QUANTUM DOT INTEGRATED SILICON PHOTONIC DEVICES FOR OPTICAL SENSOR APPLICATIONS

By

Girija Gaur

Dissertation

Submitted to the Faculty of the

Graduate School of Vanderbilt University

in partial fulfillment of the requirements

for the degree of

DOCTOR OF PHILOSOPHY

in

Electrical Engineering
December, 2015
Nashville, Tennessee

Approved:

Professor Sharon M. Weiss, Ph.D.

Professor Daniel M. Fleetwood, Ph.D.

Professor Ronald D. Schrimpf, Ph.D.

Professor Richard F. Haglund, Jr., Ph.D.

Professor Dmitry S. Koktysh, Ph.D.

Professor Kirill I. Bolotin, Ph.D.

Dedication

To my parents and to the loving memory of Chow.

ACKNOWLEDGEMENTS

I would like to greatly thank my advisor Prof. Sharon M. Weiss whose support, guidance, and encouragement have been a corner stone of my graduate school experience and research activities here at Vanderbilt University. I am forever grateful for her scientific insights and enthusiasm for allowing me the freedom and curiosity to pave my own way in a couple of different research directions. Her optimism, dedication to science and remarkable abilities to focus on several different research thrusts is an inspiration that shall forever stay with me. I would also like to thank all of my committee members for their guidance, and support during my entire research experience.

I would like to especially thank Prof. Dmitry S. Koktysh who has been an incredible part of all of my research work. His expertise in Chemistry, quantum dot synthesis and insightful scientific contributions have been a key factor in enabling such an inter-disciplinary, highly rewarding and very enjoyable research experience. I am also really grateful to everyone in the Weiss group for their support, feedback, and inputs all along the way. I would like to especially thank Jenifer and Ben Lawrie for always being so helpful, and Jenifer for being such an inspiration for managing her work and dedication to her two little kids who came along during her years as a Ph.D. student at Vanderbilt University. Also, I am very grateful to Shuren Hu who has been a source of inspiration for translating many intangible physical phenomena into applicable science all around us in innumerable ways.

I would also like to thank Sergey Avanesyan for help with the pulsed laser operation and maintenance, Ben Schmidt and Bo Choi at the Vanderbilt Institute of Nanoscale Science and Technology, and the staff at Oak Ridge National Laboratories for all their guidance and help with device fabrication.

Finally, I would like to thank my parents to whom I am grateful for their encouragement and support.

The work in this thesis was funded in part by the Army Research Office and the Defense Threat Reduction Agency. Lithographic processing was conducted at the Center for Nanophase Materials Sciences, which is a Department of Energy Office of Science User Facility. Vanderbilt Institute of Nanoscale Science and Engineering facilities were utilized for scanning electron microscopy imaging and some reflectance measurements.

TABLE OF CONTENTS

Page

LIST OF TABLES

Table Page

LIST OF FIGURES

Figure Page

1. INTRODUCTION

1.1 Optical Sensors

Our image of the world around us is governed by what we perceive and light has fundamentally been the central and most vital constituent shaping our perceptions. Advances in instrumentation, science and technology over the past few centuries have opened the door to perceiving physical phenomena beyond those that we are directly capable of perceiving. For example, it is now routine to stare at smartphone displays or quantum dot light emitting diode (QLED) television screens that project information from all over the world while taking such technological innovations for granted. 2015 is celebrated as the International Year of Light, and it also serves to remind us of the amazing progress made over the centuries in not only mathematically describing light as electromagnetic wave propagation through the equations put forward by James Clerk Maxwell in 1861-1862 but also applying such knowledge to an ever-increasing suite of applications ranging from the ubiquitous smartphones to the less widespread but more important diagnostic optical sensors.

A sensor may be broadly categorized as a device capable of transducing a physical input quantity into a measurable output signal. Some of the widely used transduction methods are electrical, mass, chemical or optical based. Optical sensors have largely dominated diagnostic technologies due to their exceptional sensitivities, manipulation-free, non-destructive analysis, and remote sensing capabilities. From the earliest inceptions of human civilizations, we as a species have been working towards the development of improved diagnostic tools that can identify diseases, toxins, and poisons to ward off early death, the spread of fatal epidemics and ensure stable, thriving economies. However, it is only recently, through careful analysis of light-matter interactions that we are now capable

of perceiving phenomena at micro- and nano-scales which are as exquisite as intracellular fluorescent protein interactions or as critical as tumor cell progressions. Most importantly, we now routinely use optical techniques to peer within ourselves and keep track of various vital signs that are beyond the physical capabilities of our five senses of perception.

1.1.1 OPTICAL BIOSENSORS

As Bill Gates announced in a recent TED Talk titled "The next outbreak? We're not ready"[1], a very realistic threat to the survival of our species is probably not an alien invasion but the emergence of a viral outbreak that can spread across the world within 24 hours due to ever-increasing interconnected forms of trade and travel. A large part of the work in this thesis is thereby motivated by the need to drive improvements in optical diagnostic technologies on several fronts such as:

1. Sensitivity
2. Rapid signal transduction
3. Low-cost
4. Portability and/or smartphone compatibility
5. Lab-on-chip capabilities
6. Multiplexing

wherein, a biosensor may be broadly categorized as a device that is capable of transducing the capture of a target analyte into a measurable signal.

Label-Free and Labeled Biosensors

Optical biosensors may be further classified as either label-free or labeled depending upon whether the target molecule requires an additional labeling step in order to be detected. A representative illustration of label-free and labeled biosensing is shown in **Figure 1.1**.

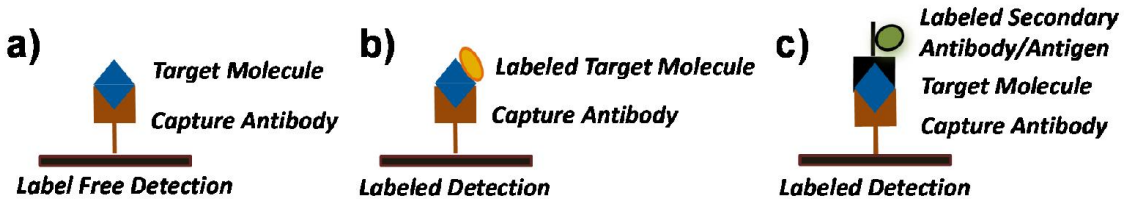

Figure 1.1. a) Label-free detection of target molecule. b) Direct-labeling of target molecule c) Indirect labeled detection of target molecule through the use of a target specific labeled secondary antibody or antigen.

The most commonly used transduction methods for label-free optical biosensors are surface plasmon resonance (SPR) and refractive index (RI) techniques. Labeled biosensors most commonly rely on fluorescent or enzymatic labels to identify target molecules.[2]

SPR sensors excite a surface plasmon wave (SPW), which is a traveling charge density oscillation at the interface of two media with dielectric constants of opposite signs such as metal and air. The capture of target biomolecules by the sensor surface will result in a change in the SPW excitation condition. **Figure 1.2a** illustrates the working principle of SPR biosensors. The most widely used method of exciting a SPW is by prism coupling. In the prism coupling configuration (**Figure 1.2b**), the incident light is totally reflected at the prism–metal interface and generates an evanescent field penetrating into the metal layer. At the resonant angle or resonant wavelength, the propagation constant of the evanescent field matches that of the SPW as described in **Eq. (1.1)**, and as a result, the photon will be coupled into the SPW (**Figure 1.2c**).[3-5]

$$\frac{2\pi}{\lambda} n_p sin\theta = \beta_{sp} \qquad (1.1)$$

where λ is the incident wavelength, n_p the prism refractive index, θ the incident angle and β_{sp} is the propagation constant of the SPW.

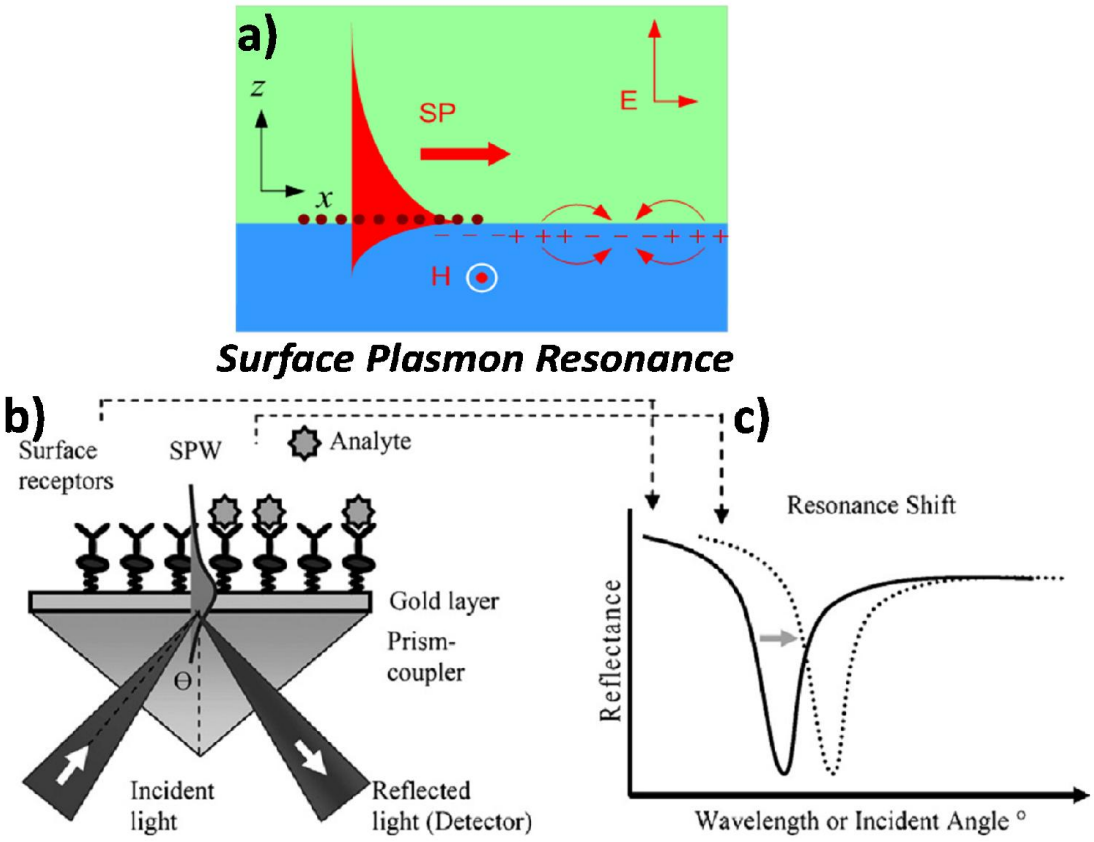

Figure 1.2. a) Working principle of SPR based biosensors. b) Prism coupling configuration used for exciting a surface plasmon wave at the active sensing surface. c) Measured reflectance of incident laser for different incident angles (fixed wavelength) or different wavelengths (fixed angle). The resonance angle or wavelength corresponds to the condition for which light couples into the surface plasmon wave. Adapted from [3-5].

While SPR sensors routinely offer detection sensitivities down to nM concentrations, some of the disadvantages facing such sensors are the rapid decrease in signal sensitivity away from the active sensing surface that makes detecting larger molecules challenging, bulky instrumentation, and challenges towards implementing a low-cost, lab-on-a-chip integrated diagnostic device.

The most common labeled sensor technology is the enzyme-linked immunosorbent assay (ELISA), which has dominated the industry since its establishment in the 1970's.[6-7] ELISA relies on enzymatic labeling of target analytes to generate a color change upon target

molecule capture. The disadvantages of ELISA are the long reaction times that can require over 24 hours, and time consuming, labeling, rinsing and washing steps that require trained personnel. As a result, ELISA remains an optical sensing technique largely confined to well-equipped laboratories.

In order to achieve rapid, highly-sensitive signal transduction, a new class of optical sensors that rely on monitoring refractive index (RI) changes are drawing increasing attention due to their potentially exceptional sensitivities, multiplexing capabilities and ability to be integrated with lab-on-chip diagnostic platforms and smartphones.[8] Some of the most promising RI based sensors are thin-film reflectance interferometers, ring-resonators and photonic crystals.[2]

1.1.2 Optical Radiation Sensors

On a related front, we are now entering an era of not only robotic space exploration but also manned interplanetary missions. The success of such missions relies greatly on the developments of radiation hardened electronics that guarantee operation in highly damaging radiation environments which in turn rely on estimations of the type of radiation sources and the total exposure dose for the missions. Terrestrial sources of high energy radiation, including nuclear power plants, also demand continual monitoring. Consequently, it is becoming increasingly necessary to develop radiation dosimeters capable of operation for extended periods of time in high radiation environments that provide improved energy resolution and real-time feedback on the type, and total dose exposure. In space environments, sources of highly ionizing radiation are primarily high energy particles such as protons and electrons and high energy photons such as gamma-rays, whose flux varies dependent upon solar flares, supernovas, blazars and pulsars. An estimate of the sources of gamma radiation are shown in **Figure 1.3a** and a comparative estimate of total radiation dose exposure on a trip to Mars is shown in **Figure 1.3b**.[9] New

types of gamma-ray-emitting objects within the "unassociated sources" in **Figure 1.3a** constitute roughly a third of the Fermi catalog.

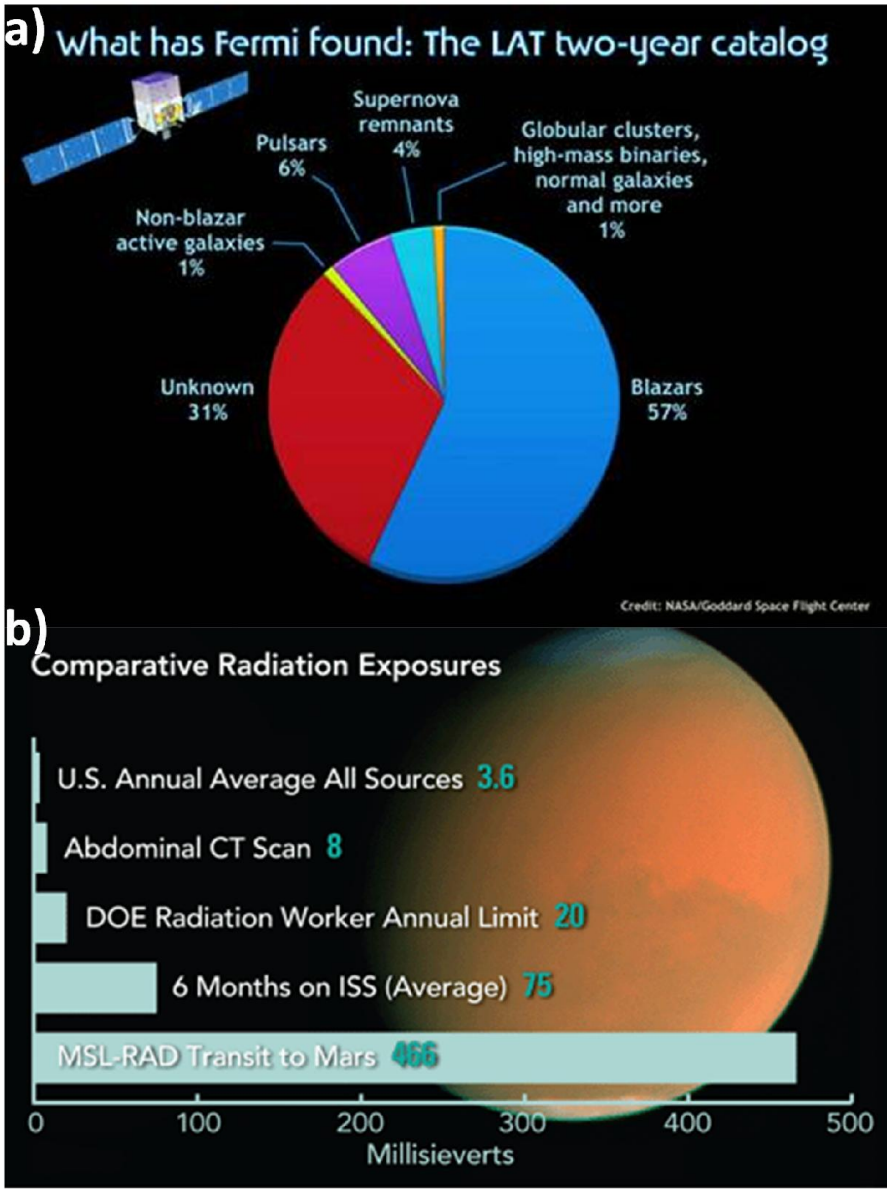

Figure 1.3. a) Active galaxies called blazars constitute the single largest source class in the second Fermi Large Area Telescope catalog, but nearly a third of the sources are

unassociated with objects at any other wavelength. Their natures are unknown. Credit: NASA's Goddard Space Flight Center. b) Plot showing possible avenues of radiation exposures and their comparative radiation exposure doses. Credit: Cary Zeitlin/Southwest Research Institute, Boulder, CO

Radiation dosimetry may be defined as a process whereby a reading is recorded through interactions of the incident radiation with matter causing a measurable change in its properties. This can be a change in the measured charge (ionization chambers), measured light output (thermoluminescent dosimeters, TLDs) or a visible polymeric chemical reaction (radiochromic film). The process is caused by atomic and nuclear interactions occurring within the atoms.[10] Notably, space radiation such as γ-rays and charged particles such as protons are referred to as "ionizing sources of radiation" due to their ability to ionize a material by delivering enough energy to permit the escape of electrons as well excite electrons to higher energy states when the energy imparted is not sufficient to cause ionization. Charged particles such as protons are capable of imparting enough energy to result in the creation of secondary charged particles such as electrons, which in turn can cause substantial ionization events of their own.[11] Due to the payload constraints for space flights, the most critical requirements for space dosimeters are low weight and low power consumption. Additionally, since ionization flux remains very low, large area dosimeters are usually more favorable.

Radiation dosimeters may be classified as either passive or active depending upon their need for power. Some of the most widely used space radiation dosimeters are the active type, such as solid state charged particle counters and ion chamber based proportional counters, and the passive type such as thermoluminescent dosimeters (TLD) and solid state nuclear track detectors (SSNTD).[12] While active dosimeters might provide greater energy resolution and real-time data, these dosimeters are only able to provide accuracy when they are able to stop the charged particle within the active sensing regions.

Many times this necessitates the use of two or more Si-detectors in a telescopic arrangements adding to the power and weight requirements. Passive radiation dosimeters, largely due to their low mass, low power consumption and robust design, continue to be an integral part of space radiation dosimetry.[13] While optical diagnostic techniques and colloidal QDs have gained widespread use in the field of biosensor developments, few real-time, optical detection techniques exist for flexible, low-cost, efficient, good energy resolution of high energy particles and photons including X-rays, gamma-rays, protons and electrons. This work will focus on the interactions of high energy photons with matter, in particular with colloidal QDs, with the aim of developing an optical radiation sensor that is low-cost, portable, re-useable, and suitable for high dose radiation environments. Additionally, this developmental avenue may be promising for terrestrial high radiation risk facilities such as nuclear power stations.

1.2 Porous Silicon

Porous silicon was accidentally discovered by the Uhlirs, a husband and wife team working at Bell Laboratories in the mid-1950s, while electromachining silicon wafers for use in the microelectronics industry. Under certain electrochemical conditions, they found that the silicon wafer did not dissolve uniformly and instead formed nanoscale voids or pores, propagating primarily in the <100 > direction in the wafer. [14]

This result was far from the desired smooth polish required for manufacturing microelectronics and the result was shelved leaving behind only a technical note in Bell labs.[14] However, in the 1990's interest in the material was vigorously renewed with the discovery of quantum confinement related light emission.[15-16] Around the same time, the

ease of fabrication of porous silicon along with its extremely high surface areas began to draw increasing attention for applications in biomedical optical sensors and optics. [8, 17-19]

Figure 1.4 provides details on the formation mechanism of porous silicon.

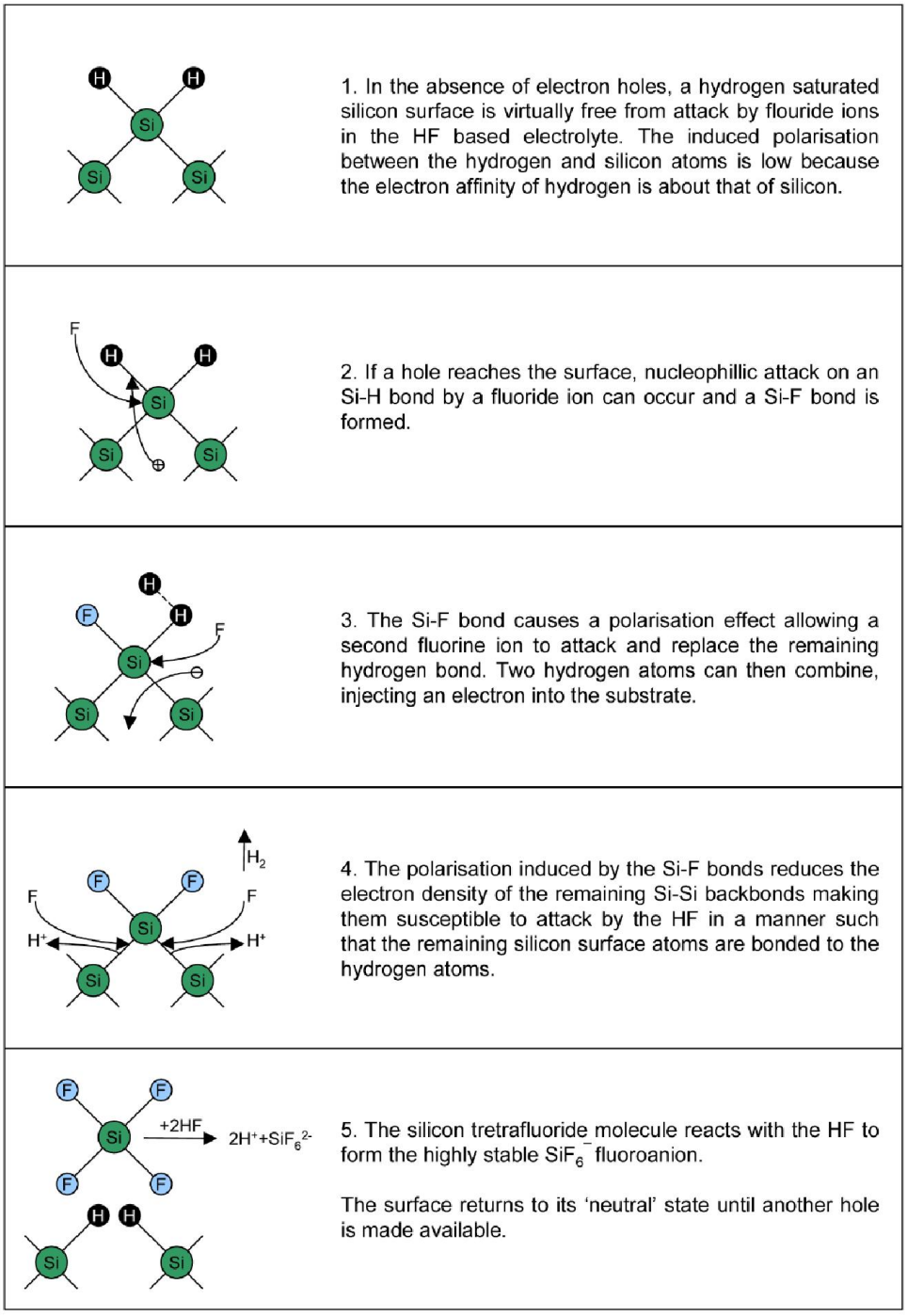

Figure 1.4. Mechanism of PSi formation on p-type silicon. Adapted from [20].

1.2.1 FABRICATION

PSi films are fabricated by electrochemical etching of silicon wafers in a two-electrode configuration as shown in **Figure 1.5**. In the work discussed in this thesis, a platinum wire counter-electrode is used and a silicon wafer with an exposed area of 1.7 cm^2 is mounted on a silver plate in a Teflon etching cell. The electrolyte consists of a hydrofluoric acid based solution. Anodization is carried out in the dark to avoid photocurrent induced variability in the formation process. Tuning of the etching conditions enables the formation of PSi films with a variety of average pore diameters, morphologies, and thickness necessary to characterize the subsequent infiltration and immobilization of small molecules in the porous framework.[21-23]

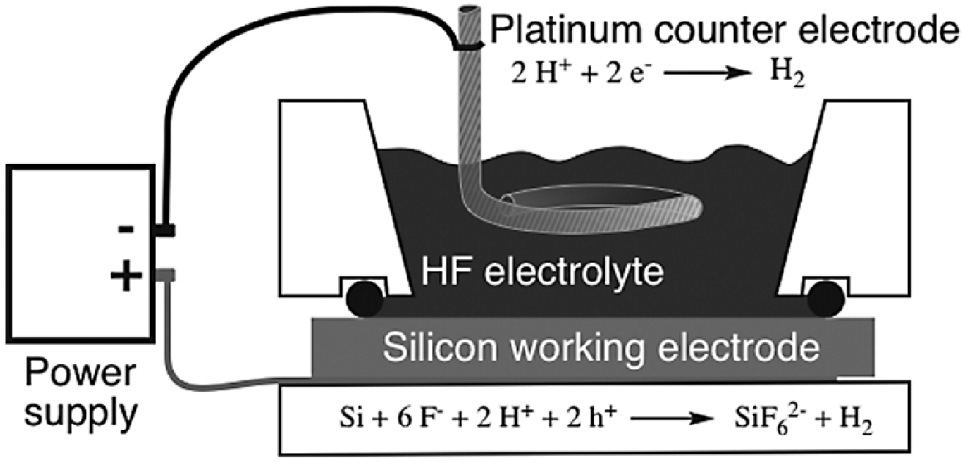

Figure 1.5. Schematic of a two - electrode electrochemical cell used to make porous silicon. Silicon is the working electrode. The working electrode is an anode, because an oxidation reaction occurs at its surface. The cathode counter-electrode is typically platinum. The main oxidation and reduction half - reactions occurring during the formation of porous silicon are given in **Figure 1.5**. Adapted from [16].

1.2.2 PSi Based Optical Biosensors

The common types of PSi optical biosensors as shown in **Figure 1.6** are:

1. thin-film interferometers
2. waveguides
3. microcavities

1. Thin-film interferometers:

Thin-film interferometers rely on the accumulated phase change of light as it traverses through a thin-film. Fabry-Perot interference fringes are formed due to the difference in accumulated phase between light reflected off the top and bottom surfaces of a thin film (**Figure 1.6a**). A spectral shift of the Fabry-Perot fringes occurs when the optical thickness of the thin film changes. In the case of PSi thin film interferometer sensors, target molecules binding inside the PSi causes a change in the effective refractive index of the thin-film, resulting in a spectral fringe shift of magnitude proportional to the number of bound molecules. Due to their straightforward fabrication, simplicity of measurement, and large surface area that allows for the capture of many molecules, PSi thin-film interferometers have been utilized by several groups for the detection of oligomers, lipids and DNA. However, thin-film interferometers exhibit average detection limits in the μM range, which is more than three orders of magnitude higher than many types of resonant sensors.[24-27]

2. Waveguides:

For the last decade, several researchers have demonstrated PSi waveguide based biosensors.[21, 28] PSi waveguides provide convenient electric field localization within easily accessible active sensing thin-films wherein light is confined within a high index core (n_1) surrounded by lower index ($n_2, n_3 < n_1$) cladding layers at the top and bottom surfaces (**Figure 1.6b**). At the core/cladding interfaces, light is totally internally reflected due to the refractive index contrast and remains confined to the waveguiding core layer. However, in order to excite a propagating mode within the waveguide region, incident light needs to be phase matched to the mode of propagation. The two commonly used methods for coupling light into waveguides are through the use of gratings or prisms. At a certain angle of incidence, the tangential component of the incident wave vector k will equal the propagation constant β of a waveguide mode. For a prism with refractive index n_p, an incidence angle θ, the coupling condition is defined as:

$$\beta = k_0 n_p sin\theta$$

While PSi waveguides provide sharp spectral features in the reflectance corresponding to the coupling angle of the incident laser beam, the requirement of such angle dependent coupling requires bulky instrumentation. Additionally, although the electric field is localized to the thin-film active sensing regions, waveguides do not provide strong enhancements of electromagnetic fields and typically achieve detection sensitivities in the 100's of nM. Recent years have witnessed tremendous improvements in the design and fabrication of optical resonators with features on par or below the wavelengths of light they

confine. These optical resonators provide sustained build-up of electromagnetic fields within cavities that typically achieve quality factors (Q) over 10^4 and electric field enhancements over orders of magnitude.[29] As a result, a small change in the effective refractive index of the cavity regions results in strong perturbation of the resonant optical modes making them highly attractive for ultra-low detection limit biosensing. Microcavities are an example of optical structures designed to confine and enhance electric field intensities over specific wavelengths.

3. Microcavities

The introduction of a so called defect layer that is $\lambda_{res}/2$ in width, sandwiched between two Bragg mirrors, results in a microcavity architecture with a resonance centered at a wavelength of λ_{res} (**Figure 1.6c**). These optical resonators achieve increased electric fields within active sensing regions for wavelengths that are able to form stable standing waves within the cavity. The two adjacent identical Bragg mirrors confine the resonant optical mode which lies at the center of their stop band and any light at the resonance wavelength that reaches the cavity is trapped within it and decays away within the layers. Such resonators show a sharp dip in the reflectance spectra at the resonance wavelengths with high Q and enhanced electric fields within the cavity layer. Typically, these microcavity structures require several periods within the Bragg mirrors and are usually a couple of microns of thickness. For PSi, such architectures introduce difficulties for target molecule infiltration into these buried cavity layers. In order to achieve sufficiently high index contrast, the two alternating thin-films need a really low porosity film with an index of ~2 or larger and a fairly high porosity thin-film with an index of ~1.75 or lower. The

electrochemical etching of silicon introduces constraints in the average pore sizes that are capable of being formed within these low porosity films with average pore sizes routinely etched being on the order of ~5 nm – 10 nm for highly doped p-type silicon wafers. The electrochemical etching of n-type silicon wafers typically results in large pore sizes, reduced control over engineering large index contrasts and rougher interfacial surfaces that lead to increased light scatter and poorer quality optical device performance. Therefore, although PSi microcavities could potentially achieve ultra-sensitive small molecule detection down to the fg levels, these resonators have not translated into any commercially available architectures.

In conclusion, thin-film interferometers offer the most convenient, low-cost potential for developing highly sensitive small molecule point-of-care optical sensors. In this work, we engineer a method to increase their detection sensitivities by over an order of magnitude, with detection times of a couple of minutes, by using colloidal QDs as refractive index amplifiers and labeling the target molecules with these highly stable quantum emitters. Colloidal QDs inherently have a high refractive index of 2 or more which in comparison to biomolecules offers a convenient boost to the detectable signal by at least 33%. This technique is especially advantageous for extremely small molecules or toxins (1 nm in size) that are traditionally very hard to detect by refractive index based biosensors. QDs can be engineered to be easily ~20 nm in size adding a substantial boost to the increase in effective refractive index upon capturing a 1 nm sized small molecule labeled with a 20 nm sized QD resulting in a potential increase in detected signal by a factor of 26 or 40 depending upon the refractive index of the QD being either 2 or 2.9 and assuming a 1:1 binding stoichiometry between the small molecule and the QD. Additionally, QDs provide a

secondary means of target molecule identification via their strong photoluminescence signal that allows for multiplexed target molecule detection capabilities.

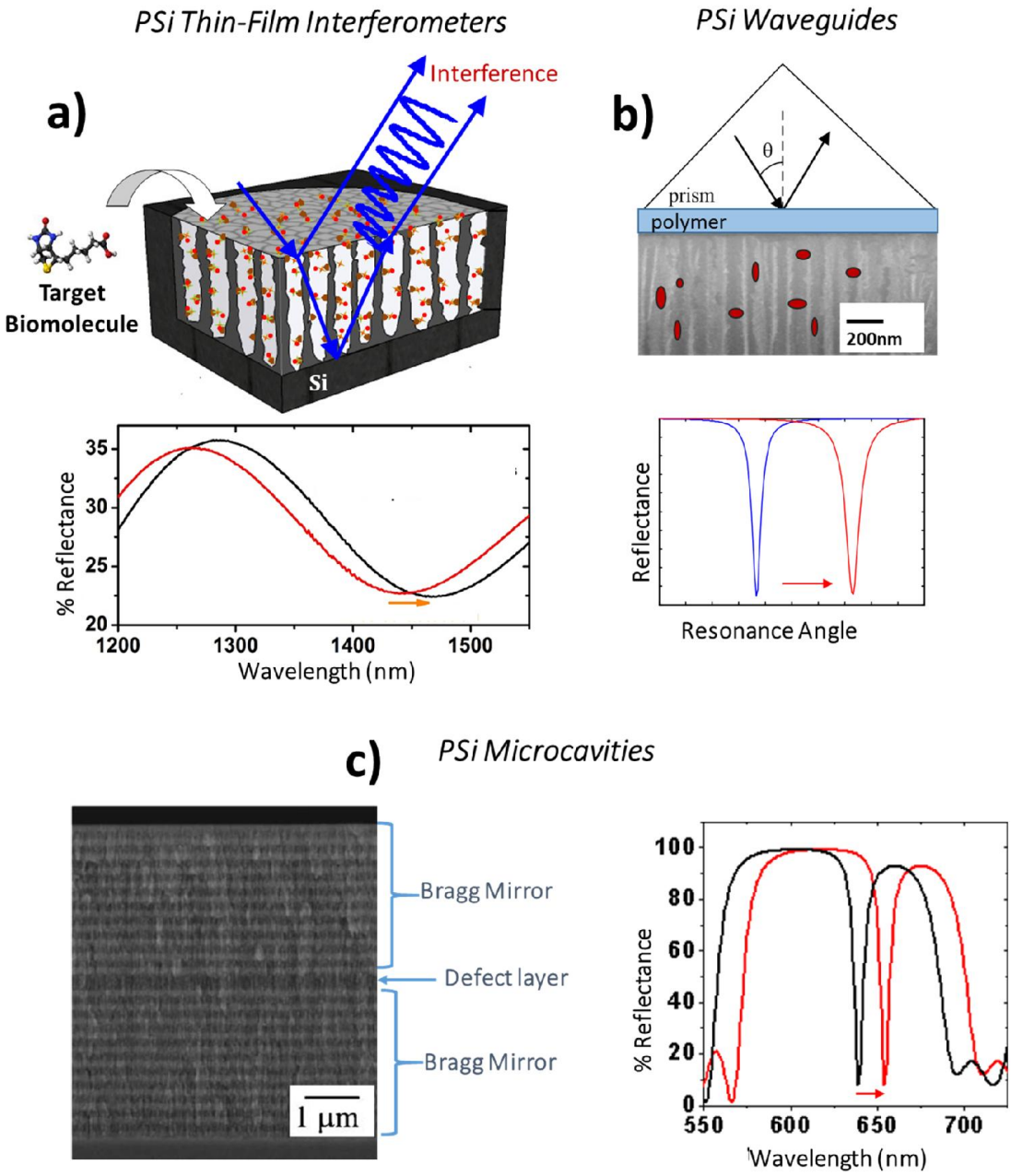

Figure 1.6. a) PSi thin-film interferometer based optical sensors. The characteristic Fabry-Perot fringes in the reflectance spectrum show a red-shift after capture of target biomolecules. The shift in the fringes corresponds directly to the change in phase shift, $\Delta\Phi$, introduced as light passes through the thin-film with captured target biomolecules. b) PSi

waveguides in the prism coupling configuration. Light incident at an angle θ is phase matched to the propagation constant β of a waveguide mode. Any change in the effective refractive index of the PSi waveguide film will cause a change in the propagation constant β and thereby change the coupling angle of the incident laser. This is sometimes referred to as a change in the resonance angle of the prism coupled waveguide. c) Cross-sectional SEM image of a PSi microcavity structure showing infiltrated biomolecules in the cavity layer.

1.2.3 Enhancing Light-Matter Interactions Through Cavity Optimizations

While thin-film PSi reflectance interferometers offer straightforward, low cost and high sensitivity optical diagnostics, it is possible to improve optical detection sensitivities even further by engineering active sensing regions that enhance light-matter interactions. The most commonly used resonators for optical diagnostics are microring resonators, 2D photonic crystals, and 1D nanobeam photonic crystals (**Figure 1.7**).

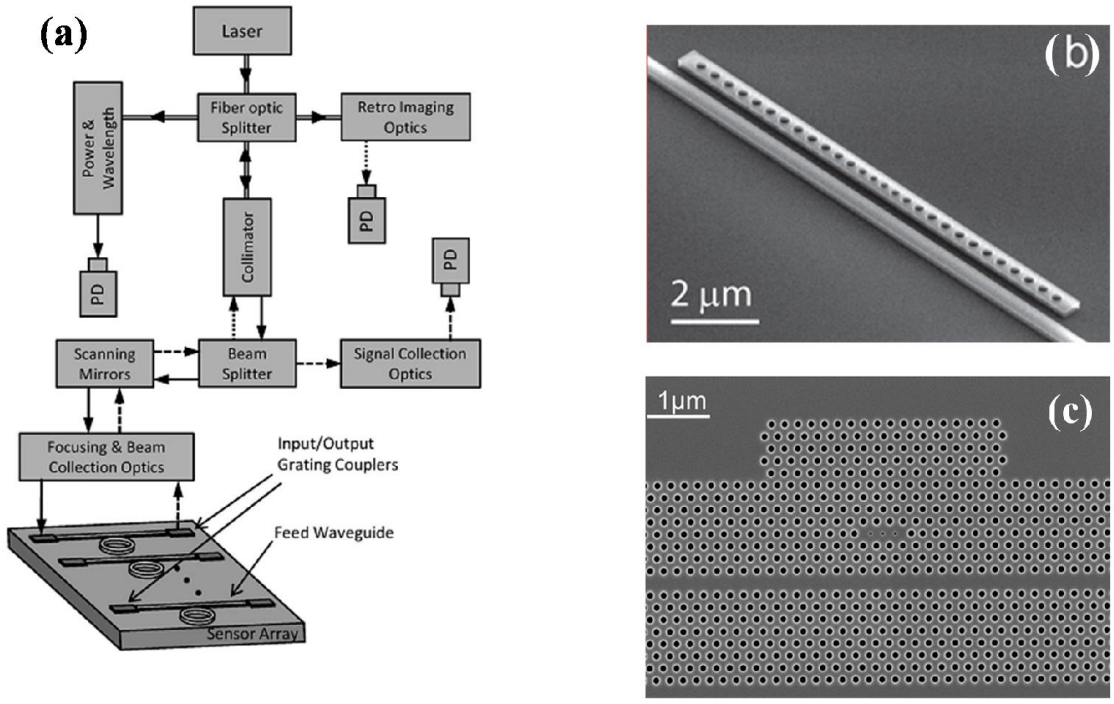

Figure 1.7. Label-free optical resonator sensors (a) High level architecture of the ring resonator array biosensing platform adapted from [30] (b) 1D photonic crystal nanobeam sensor adapted from [31] (c) 2D photonic crystal cavity sensor adapted from [32].

Such approaches rely on the near-lossless manipulation of the flow of light at wavelength scale geometries to achieve higher temporal confinement of photons. This enables increased interaction of captured biomolecules and chemical species with the guided modes of light coupled into these dielectric devices.[30-35] Detection sensitivities of 200 nm/RIU are routinely reported for ring resonators whereas 1D and 2D photonic crystal based sensors can achieve sub-pg/mm^2 detection limits with over 400 nm/RIU detection sensitivities.[32, 36]

The drawback of these optical resonators, especially for low-cost, point-of-care deployment, is the requirement for careful coupling of light in-plane, that may be either fiber-coupled or grating-coupled, and the costly equipment overhead that comprises of a tunable laser and photodetector. For 2D photonic crystal slab sensors, it is possible to use

direct normally incident light and couple it into a so-called guided mode resonance (GMR) without the need for coupling optics (**Figure 1.8**). However, although this configuration may be suitable for large area sensors with no coupling optics required, it is extremely sensitive to variations in the light incident angle requiring carefully aligned light incident only normally to the sensor surface. The Q values for GMR photonic crystal slabs are also usually lower and while simulated detection sensitivities reported may be as high as 800 nm/RIU, fabricated devices so far report sensitivities closer to only 100 nm/RIU.[24, 37]

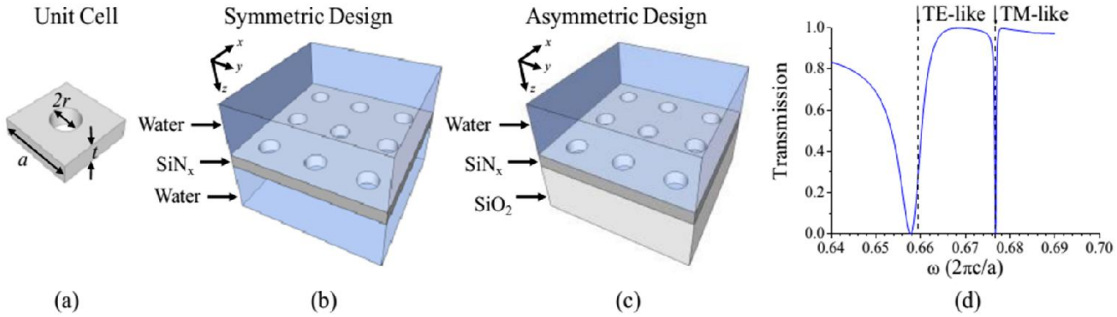

Figure 1.8. (a) A unit cell for a square grid of holes PCS. Illustrations of (b) symmetric and (c) asymmetric PCS designs. (d) A typical transmission spectrum for a PCS with guided resonance frequencies indicated by dashed lines.

For most of these optical sensors, new design approaches have demonstrated control over light on ever-decreasing length scales and have led to dramatically improved detection sensitivities. The increasing light-matter interactions through the design of sub-wavelength optical cavities achieve not only exceptional temporal confinement of photons but also reduced mode volumes. Some examples of these design advancements are the slotted nanobeam photonic crystal cavities that achieve Q factors as high as 10^6 and sub-wavelength mode volumes $(< \lambda/n)^3$.[38]

In this work, we circumvent the need for coupling optics and complex instrumentation, by designing two different types of optical cavities. The first one is a PSi microcavity integrated with a high contrast grating (μC-HCG). This optical cavity supports highly

sensitive, label-free detection of analytes. Upon capture of target analytes, the narrow linewidth spectral resonance of the cavity, shifts in correspondence to the amount of target captured, and the shift may be monitored using a simple broadband light source in a reflectance configuration (**Figure 1.9**). Arrays of such μC-HCGs may be fabricated and integrated with PDMS microfluidic flow cells for delivery of μL volumes of target analytes to the active sensing regions as shown in **Figure 1.9a**. The μC-HCG sensor arrays can also support multiplexed detection of analytes especially through the use of QD-labeled targets, whose wavelength specific PL acts as a secondary means of target biomolecule capture **Figure 1.9d**.

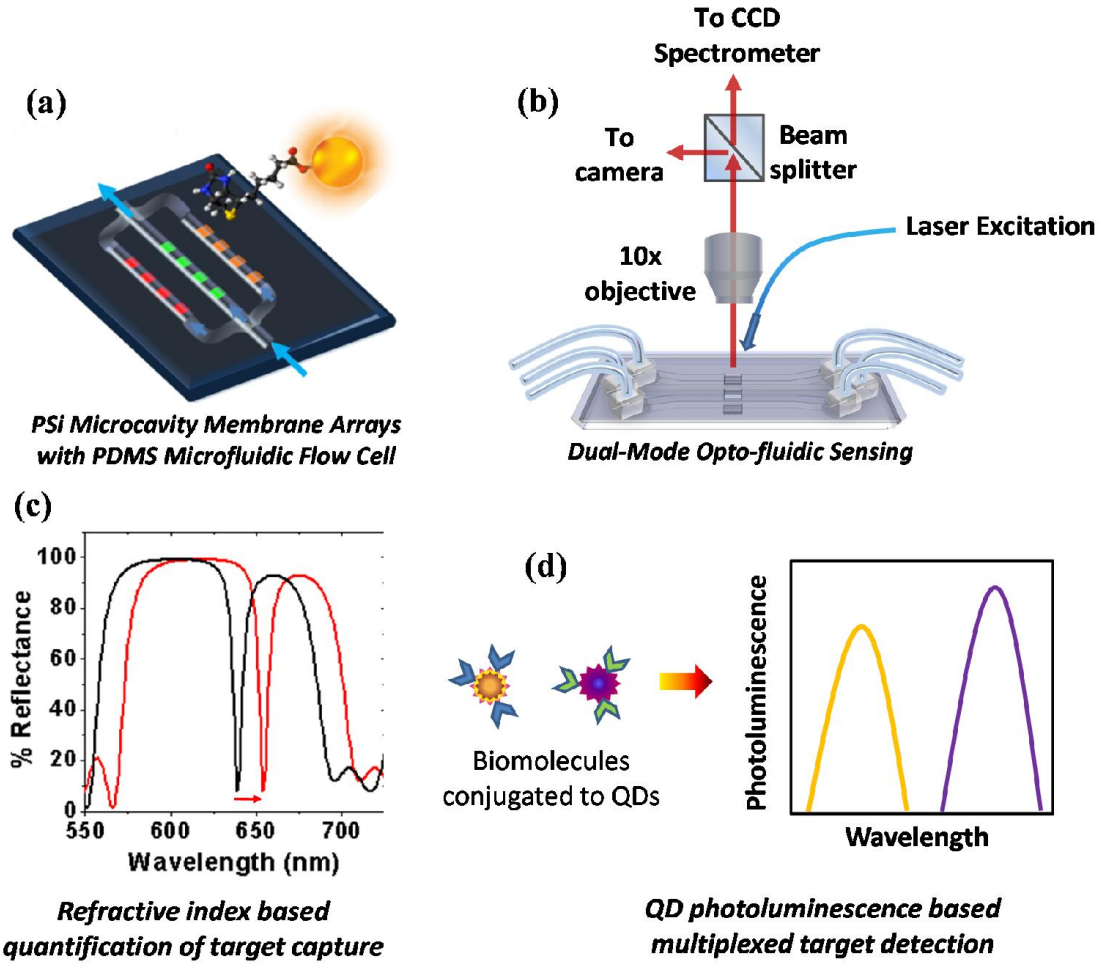

Figure 1.9. a - b) PSi microcavity-HCG membrane arrays integrated with PDMS microfluidic flow cells for the dual-mode, opto-fluidic, real-time detection of QD-

biomolecule conjugates. c) Sharp spectral features corresponding to the cavity resonance wavelengths in the reflectance measurements enhance the detection sensitivities. d) Strong QD PL enhanced at the microcavity resonance wavelength provides secondary confirmation of target molecule capture which is additionally advantageous for multiplexed target molecule detection.

The second optical cavity is a PSi annular Bragg resonator (PSi-ABR) that features its own emission source using cavity coupled QDs that function as built-in light emitters (**Figure 1.10**). This sensing platform, once integrated with QDs, also functions as a label-free sensor requiring straightforward excitation by an inexpensive LED to provide a cavity modified, narrow line-width QD emission with strong photoluminescence (PL) intensities. Any changes to the environmental refractive index of the sensor, upon target molecule capture, will perturb the cavity resonance conditions causing a shift in the cavity coupled QD emission profile. This shift in the QD emission profile can be easily monitored by using a camera or spectrometer. ABRs have the potential to achieve Q values of 10^6, on par with those achieved by 2D PhCs, with more flexibility in the choice of device material, while providing micron-sized regions of extremely high light-matter interactions.[39]

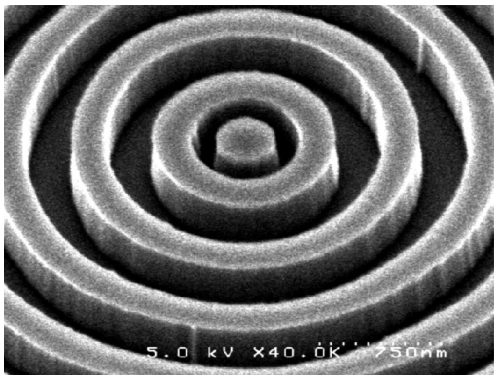

Figure 1.10. SEM image of an annular Bragg nanocavity designed to support the m=0 mode in a 300 nm wide central pillar adapted from [39]

1.2.3.1 PSi Microcavities Integrated with High Contrast Grating Reflectors

Thin-film reflectance interferometry may be extended to free-standing PSi microcavity (μC) membrane arrays wherein open-ended pores allow for faster diffusion kinetics of analytes through active sensing regions. The traditional PSi μC design is shown in **Figure 1.11a** and its corresponding reflection spectra is shown in **Figure 1.11b**. The microcavity sensor design enhances light-matter interactions in the cavity regions while providing sharp spectral features in the reflectance spectra as shown in **Figure 1.11b** that improve detection sensitivities.

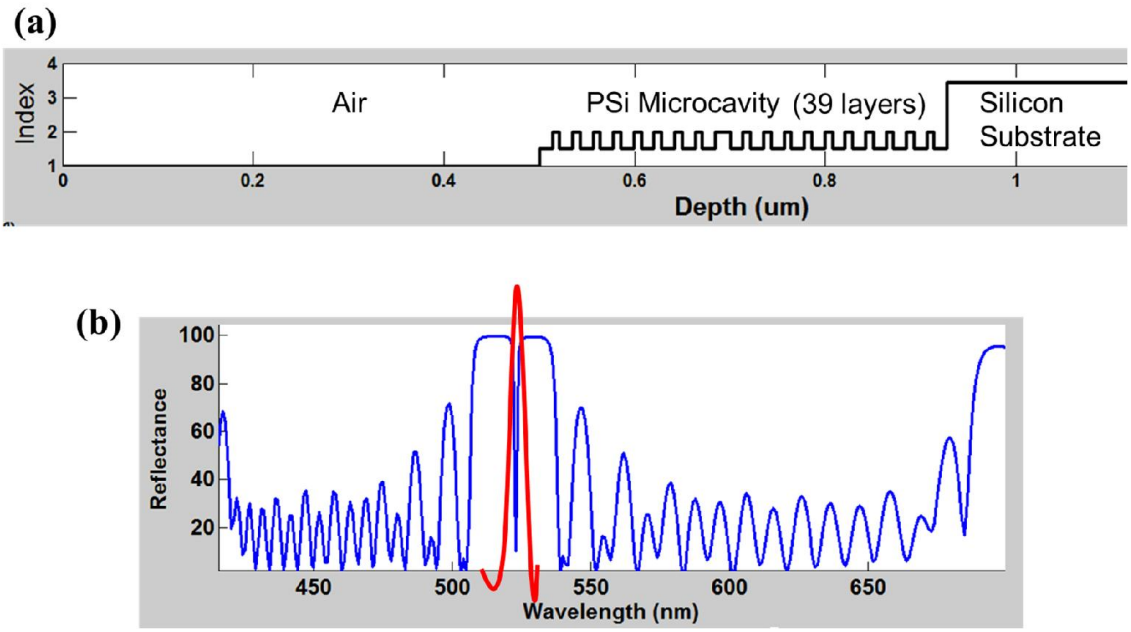

Figure 1.11. a) Refractive index profile for a traditional μC sensor with 39 total high and low porosity alternating layers. b) Simulated reflectance profile for the μC with Q factors ~450 at a resonance wavelength ~525 nm. Shown also is the cavity modified QD emission profile (red) that coincides with the cavity resonance wavelength.

The μC design is centered around resonance wavelengths within the visible spectrum. This provides an additional advantage for QD-labeled analyte detection. The overlap of QD emission wavelengths with the cavity resonance wavelength, results in narrow linewidth

visible QD emission spectra (**Figure 1.11b**) that can be monitored in a straightforward and low-cost manner. The QD-labeling of target biomolecules, thereby serves as a secondary means of identification of target specific detection that is advantageous for multiplexed detection arrays.

However, although the fabrication of PSi microcavities is low-cost and straightforward, these optical structures consist of several alternating layers of small and large pore sizes that correspond to high and low refractive index layers respectively. While infiltration through the low refractive index layers is usually straightforward due to the fairly large pore sizes, the high refractive index layers and limited to much lower pore sizes of ~15 nm. **Figure 1.12** shows the cross-sectional SEM images of a traditional PSi μC structure with alternating high and low refractive index layers. The cavity shows a high porosity layer with pore sizes ~ 25 nm while the low porosity layers have pore sizes ~15 nm. This limitation arises from the electrochemical formation mechanisms of PSi. As a result, fabrication of alternating high and low refractive index layers with sufficient refractive index contrast usually results in intermediary layers of fairly small pore sizes. This has resulted in severe difficulties in their practical implementation as robust immunoassay platforms.

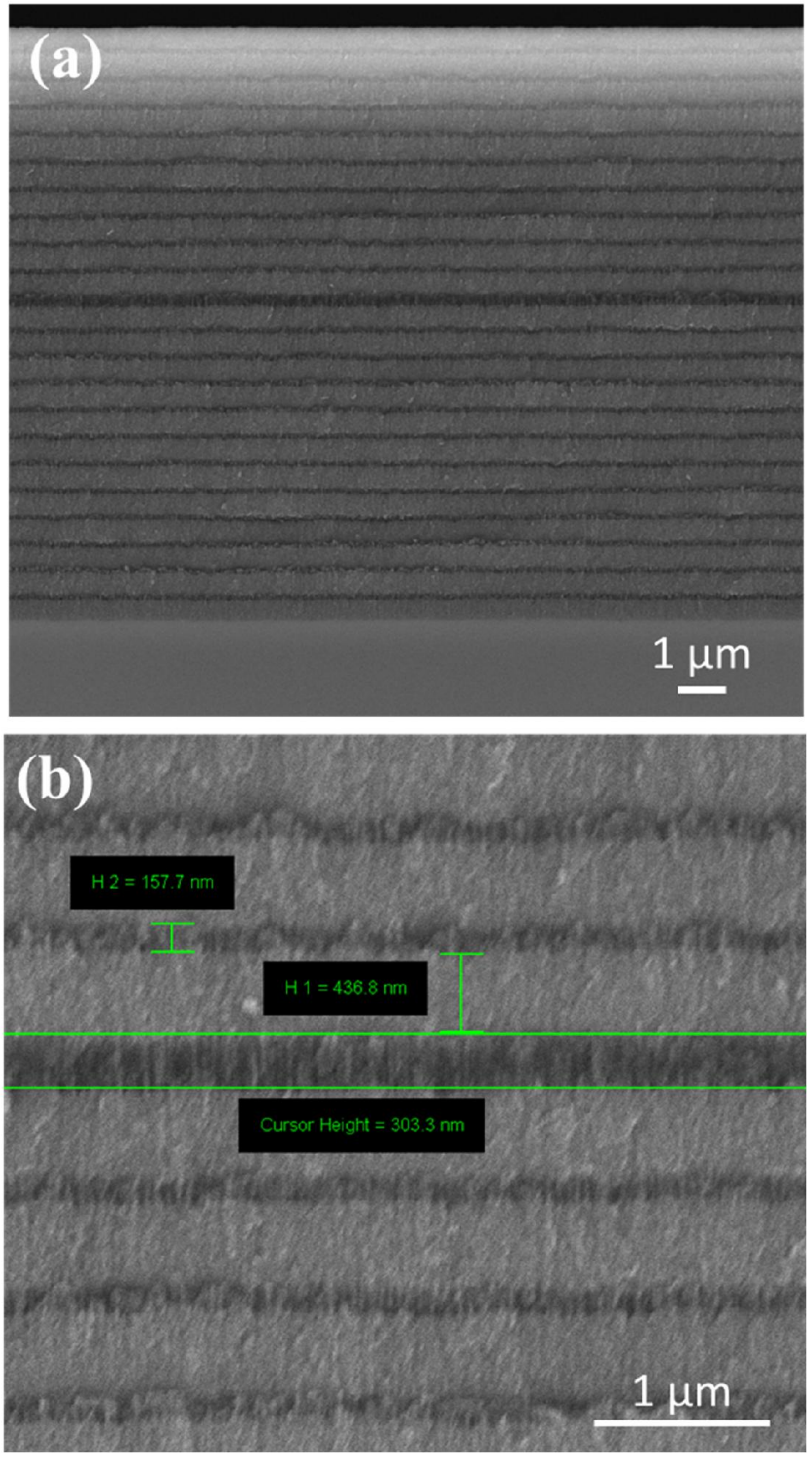

Figure 1.12. Cross-sectional SEM images of a traditional PSi µC consisting of 9 period and 11 period Bragg stacks at the top and bottom respectively.

In order to overcome analyte and linker molecule infiltration challenges, a high contrast sub-wavelength grating reflector has been utilized as a replacement optical structure for one entire Bragg stack at the top of the microcavity structure. This approach allows access of target molecules to the cavity region that now lies directly below the high contrast grating (HCG).

High Contrast Sub-Wavelength High Gratings

Since the first demonstration of a sub-wavelength broadband mirror (**Figure 1.13**) in 1999 by Mateus et. al., several applications of sub-wavelength high contrast gratings have emerged such as vertical cavity surface emitting laser (VCSEL), lenses, focusing elements, and filters (**Figure 1.14**).[40-43] Careful optimizations of the design demonstrated broadband reflectivity $R > 99\%$ with $\Delta\lambda/\lambda > 30\%$ for a polysilicon grating with $n_h = 3.48$, a SiO_2 low index material with $n_L = 1.47$ and a silicon substrate, designed for a central wavelength of 1.55 μm as shown in **Figure 1.13b**.[40] Sub-wavelength gratings do not have diffraction orders other than the zeroth (in this case – surface normal) order, and thus all power that is not transmitted through the zeroth diffraction order gets reflected back. This fact differentiates sub-wavelength gratings with broadband reflectivity from normal gratings since cancellation of the 0^{th} transmissive diffraction order results in high reflectivity.[44] One of the criteria for these sub-wavelength grating structures however, is the required high index contrast of at least 2 to achieve broadband high reflectivity. Additionally, it has been reported that a low index region below the HCG layer is critical for the mirror performance performance. [40]

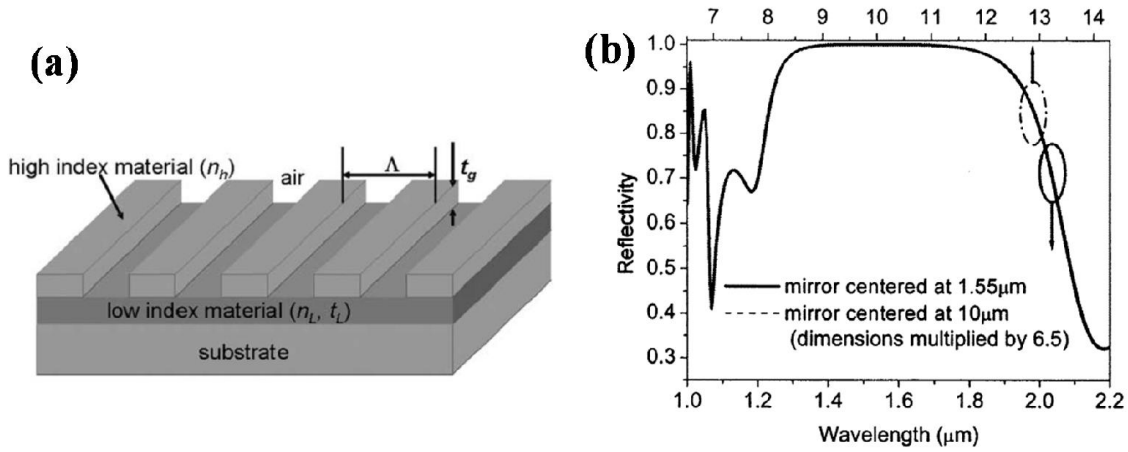

Figure 1.13. (a) Schematic illustration of a sub-wavelength grating reflector. The low index material under the grating is essential for the broadband mirror effect. (b) Simulated reflected power for light polarized perpendicularly to the grating lines. A simple scaling factor (6.5) applied to the dimensions gives completely overlapped traces. The thick line is centered at 1.55μm, while the dashed line is at 10 μm. Figure adapted from [40]

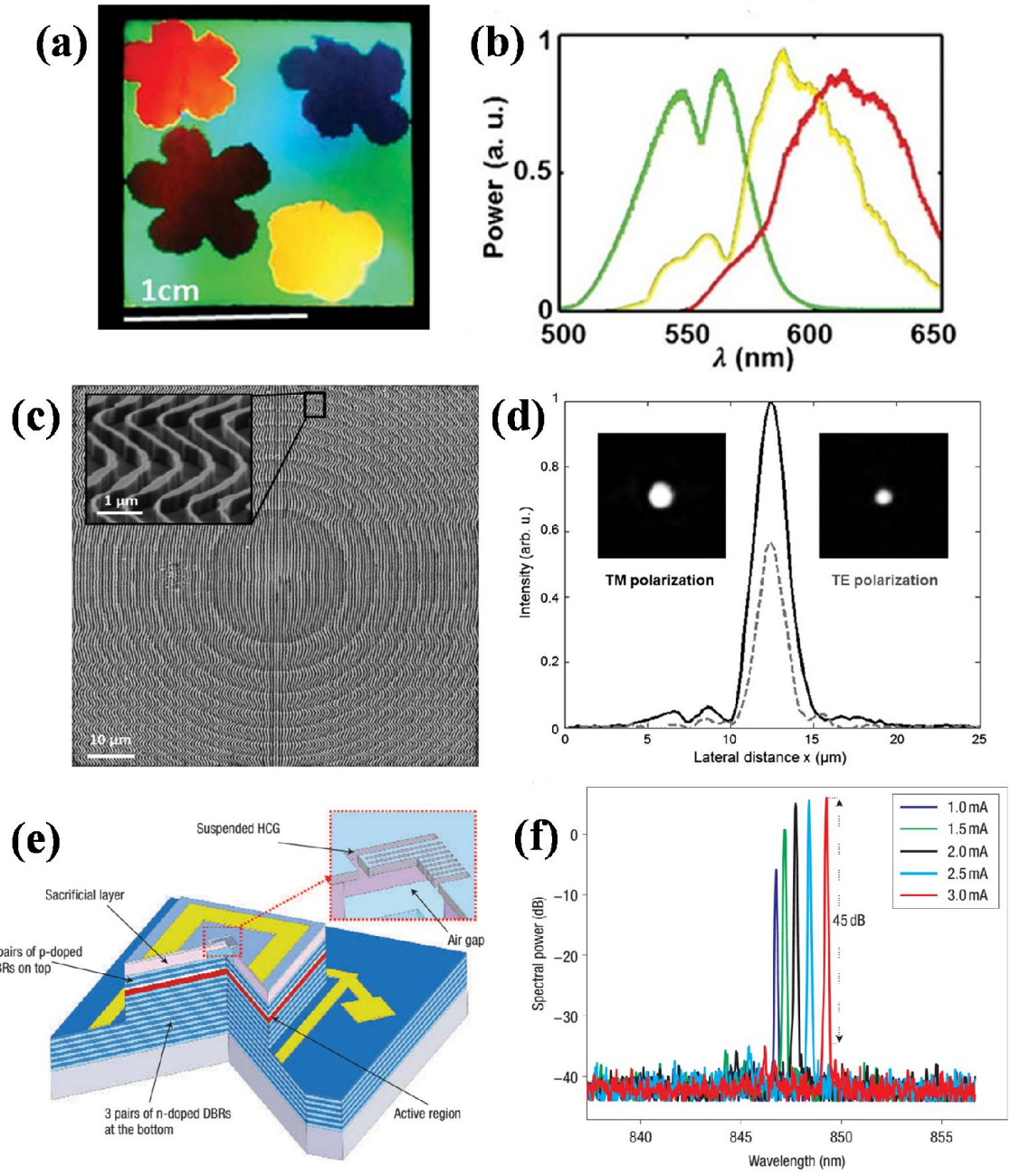

Figure 1.14. (a) Photograph of the display sample under the white light illumination. (b) Spectra of the -1st order for green, yellow, and red designs. (c) Scanning micrograph of the entire fabricated grating lens for f = 100 μm (top view). The inset emphasizes the region with two phase jumps (taken at 70° viewing angle). (d) Lateral intensity profiles of the reflected focal spot for TM (solid black line) and TE polarization (dashed grey line) together with the respective images. The first-order rings of the Airy diffraction pattern are clearly visible in the intensity plots. (e) Schematic cross-sectional layout of the VCSEL

with the top mirror consisting of a freely suspending HCG and four pair DBRs. (f) Measured single-mode emission spectra under different bias currents, showing a 45 dB suppression of higher-order transverse modes. Figure adapted from [41-42, 45]

Careful optimizations of the design demonstrated broadband reflectivity $R > 99\%$ with $\Delta\lambda/\lambda > 30\%$ for a polysilicon grating with $n_h = 3.48$, a SiO_2 low index material with $n_L = 1.47$ and a silicon substrate, designed for a central wavelength of 1.55 μm as shown in **Figure 1.13b**.[40]

1.2.3.2 PSi-ABRs

Extending the concept of 1D photon confinement in a μC-HCG resonator, to a complete in-plane confinement of resonant modes in an ABR geometry serves to further enhance light-matter interactions over reduced mode volumes. Additionally, the integration of PSi-ABRs with QDs results in the development of an optical sensing platform that has its own built-in light source (**Figure 1.15**).

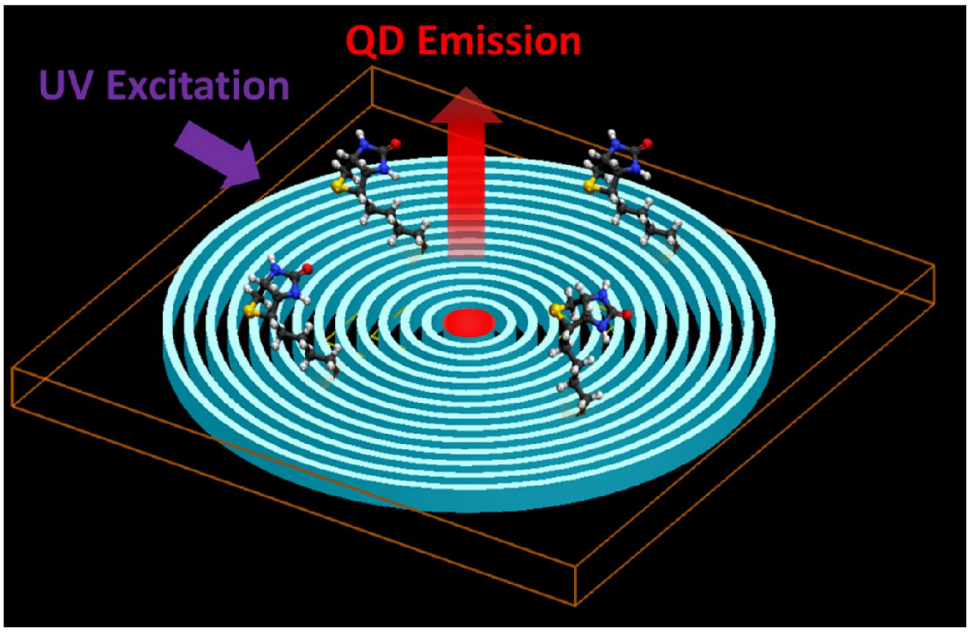

Figure 1.15. Schematic representation of a PSi-QD ABR biosensor. (not to scale)

Unlike photonic crystals, ABR geometries are also more tolerant to fabrication tolerances and non-expensive, UV sources of LED excitation may be used to excite the attached quantum dots whose cavity-coupled emission spectra will be characterized by strong and narrow spectral features with Q factors (~10^3 – 10^5) far exceeding those achievable by a PSi μC-HCG resonator. Compared with linear structures, ABRs achieve in-plane photon confinement and a minimal refractive index contrast of the materials may be used. This is an inherent advantage over traditional photonic crystal cavities where a high index contrast lattice is required for a photonic band gap, and thus, the choice of suitable materials is very limited.[39] As a result, these structures may be fabricated using partially oxidized, PSi thin-films whose tunable pore sizes, allow for infiltration of QDs into the regions of strong EM field confinement. Any changes in the surrounding environmental refractive index will be detected by a shift in resonance wavelength of the annular Bragg resonators which in turn, will shift the peak QD emission wavelength.

Overall, this strategy incorporates the advantages of enhanced light-matter interactions in photonic cavities with those of strong light emitting QDs in a silicon based porous material platform that allows for incorporation of light emitters and target biomolecules into the regions of highest light-matter interactions. This provides a means of developing highly sensitive, inexpensive, and robust, optofluidic laser biosensors.

1.3 Quantum Dots

Quantum dots are artificially engineered semiconductor nanocrystals whose energy band gap strongly depends upon their size and shape. For macroscopic semiconductors this

band gap is a fixed parameter. However, the phenomenon wherein, electronic excitation can feel the presence of particle boundaries, as particle sizes approach the quantum confinement regime, and adjust their energy spectra, is known as the quantum size effect and the nanoscale particles that exhibit it are referred to as quantum dots.[46] Since the development of QDs over two decades ago, significant advancements in their synthesis have led to more stable QDs with controlled optical and electronic properties. As a result, QDs have been integrated into devices and other semiconductor materials for applications ranging from LEDs, lasers and biological labels to photovoltaics and photodetectors.[47-52] **Figure 1.16** shows the variation in electronic confinement and density of states as a function of decreasing semiconductor dimension. Increasing degrees of quantum confinement with decreasing dimensions leads to a collapse of continuous energy bands of the bulk material into discrete atomic energy levels for quantum dots. As quantum dots may be engineered with varying electronic and optical properties depending upon their size, they resemble atoms more than bulk materials and have been nicknamed as artificial atoms.

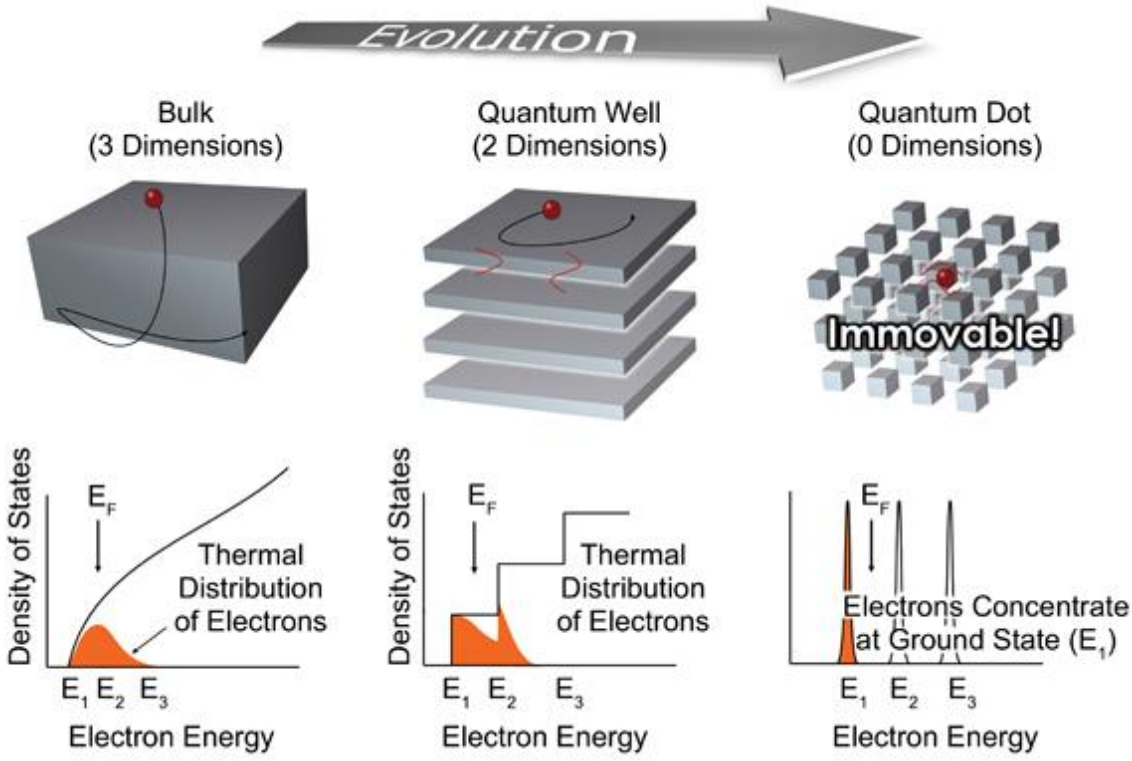

Figure 1.16. Schematic illustration of electronic confinement and the density of states in one band of semiconductor as a function of dimension for bulk semiconductors, 2D quantum well structures and 0D quantum dots. Shrinking dimensions concentrate electronic states. Courtesy QD Laser.

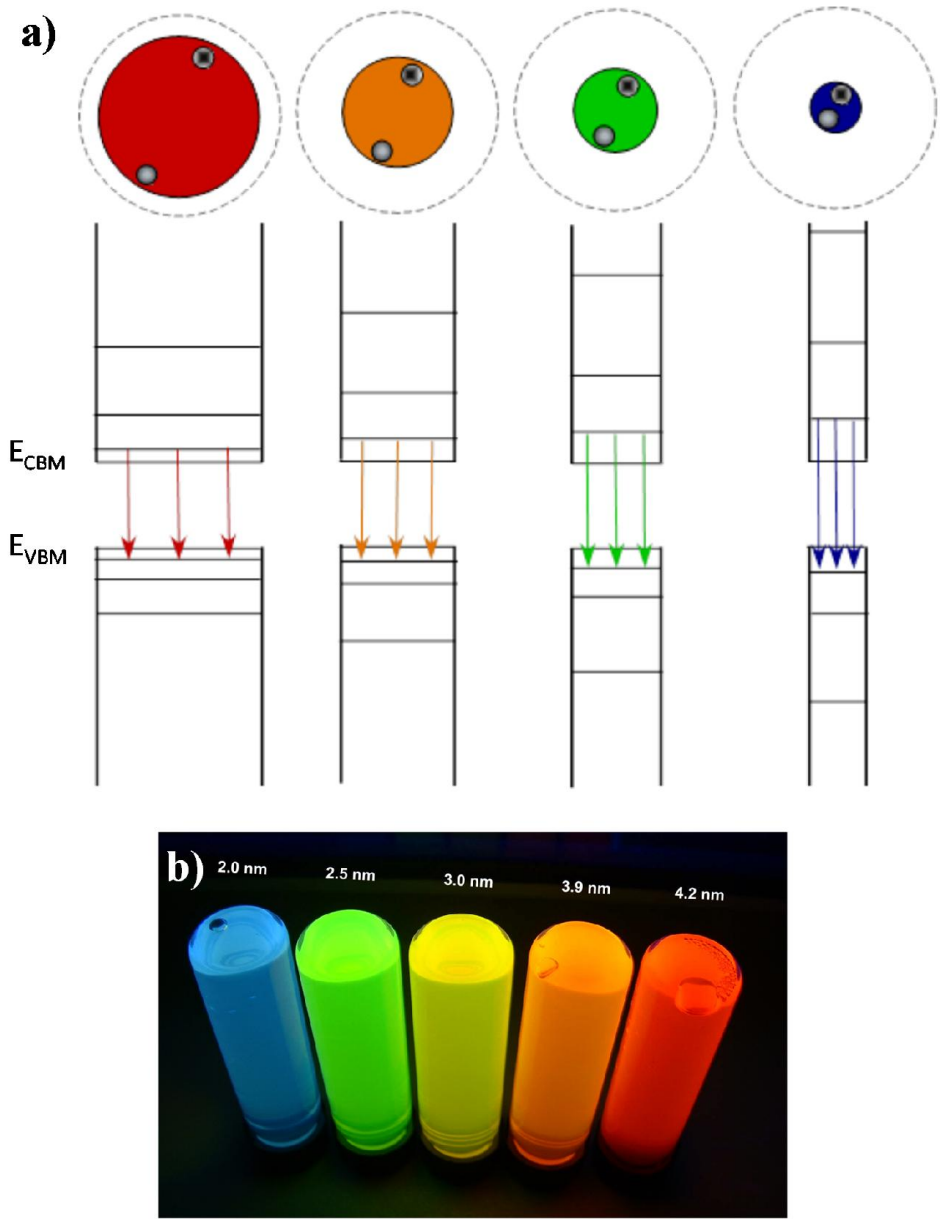

Figure 1.17. a) Schematic demonstrating the quantum confinement effect in semiconductor QDs. Spatial confinement of carriers directly affects the electronic structure of the material. With decreasing particle sizes, below that of the Bohr exciton radii (shown as dashed circles around nanocrystal depictions), blue shift in optical properties are observed and associated with widening band gap energies.[53] E_{CBM} and E_{VBM} denote the conduction band minima and valence band maxima respectively. b) Camera image of different sized CdSe QDs under UV excitation. Courtesy Rice University.

Figure 1.17 a) provides a schematic illustration of the increasing bandgap energies of QDs with increased quantum confinement arising from decreasing nanocrystal sizes and Figure xyz b) shows the size dependent emission color of CdSe QDs. Since the development of QDs over two decades ago, significant advancements in their synthesis have led to more stable QDs with strong wavelength specific emission (**Figure 1.17 b**) and controlled optical and electronic properties. As a result, QDs have been integrated into devices and other semiconductor materials for applications ranging from LEDs, lasers and biological labels to photovoltaics and photodetectors.[47-52]

Further details on the integration of quantum dots with porous silicon structures will be presented in **Chapter 2** under **Section 2.2**.

1.4 Modeling and Simulations

1.4.1 Transfer Matrix Simulations

The transfer-matrix method is used to analyze the propagation of electromagnetic waves in layered media. Its simplicity is based on the continuity in boundary conditions between layer interfaces applied to Maxwell's equations. For layered media, this approach simplifies the computation that would otherwise require calculations of partially reflected and partially transmitted light propagation and the resulting interference arising between several light paths while traversing all the layers. Based on the transfer-matrix method, if the incident field is known, the resulting transmitted field and reflected field can be calculated based on simple matrix operations. [54-55]

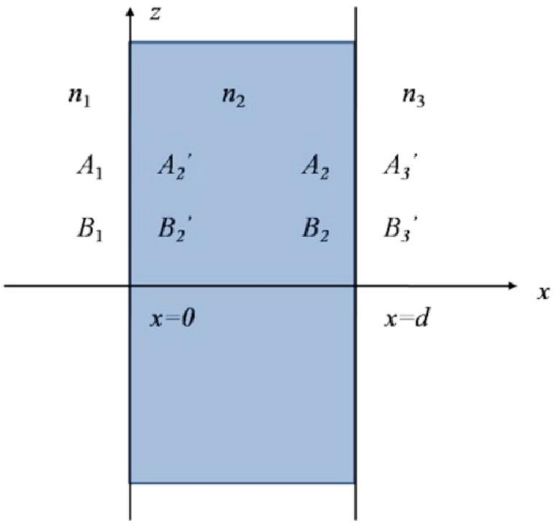

Figure 1.18. A thin layer of dielectric medium.

Figure 1.18 shows an arbitrary thin-film of thickness *d* and refractive index n_2 in-between two media of refractive indices n_1 and n_3. The whole medium is assumed to be infinite in *z*. The electric field that satisfies Maxwell's equations is given by the form,

$$E = E(x)e^{i(\omega t - \beta z)} \quad \ldots\ldots\ldots\ldots\ldots\ldots\ldots\ldots\ldots\ldots 1.4.1$$

where, β is the *z* component of the wave vector and ω is the angular frequency. We assume that the EM wave is propagating in the *xz* plane and is transverse electric (TE) or s-polarized (E || y), with the electric field E(x) in each layer can be described as a superposition of a right-propagating wave A(x) and a left-propagating wave B(x). Therefore the electric field in each layer can be written in the form of

$$E_y(x) = Ae^{-ik_x x} + Be^{ik_x x} \quad \ldots\ldots\ldots\ldots\ldots\ldots\ldots\ldots\ldots\ldots 1.4.2$$

where, A and B are the amplitudes of the electric field of the propagating waves and $\pm k_x$, are the components of the wave vector. Based on Maxwell's equations, the magnetic field *H* can be calculated from

$$\vec{H} = \frac{i}{\omega\mu}\nabla x\vec{E} \quad \text{.....1.4.3}$$

After substituting the electric field into Eq. (1.4.3) the tangential component (z component) of the magnetic field can be described as

$$H_z(x) = -ik_x A e^{-ik_x x} + ik_x B e^{ik_x x} \quad \text{.....1.4.4}$$

After applying the continuity conditions, that tangential electric field and magnetic field are both continuous at interfaces, the following two equations are satisfied at the interface, x=0.

$$A_1 + B_1 = A_2' + B_2', \quad \text{.....1.4.5}$$

$$-ik_{1x}A_1 + ik_{1x}B_1 = -ik_{2x}A_2{}' + ik_{2x}B_2{}' \quad \text{.....1.4.6}$$

where A' and B' are the electric amplitude on the right side of the same interface. These two equations can be also written in the form of a matrix equation

$$\begin{pmatrix} 1 & 1 \\ -ik_{1x} & ik_x \end{pmatrix}\begin{pmatrix} A_1 \\ B_1 \end{pmatrix} = \begin{pmatrix} 1 & 1 \\ -ik_{2x} & ik_{2x} \end{pmatrix}\begin{pmatrix} A_2{}' \\ B_2{}' \end{pmatrix} \quad \text{.....1.4.7}$$

Therefore, the amplitudes of the electric field on each side of interface are related by Eq. (1.4.8)

$$\begin{pmatrix} A_1 \\ B_1 \end{pmatrix} = D_{12}\begin{pmatrix} A_2{}' \\ B_2{}' \end{pmatrix} \quad \text{.....1.4.8}$$

with a transmission matrix D_{12} at the interface from medium 1 to 2 (x=0) defined in Eq. (1.4.9)

$$D_{12} = \begin{pmatrix} 1 & 1 \\ -ik_{1x} & ik_{1x} \end{pmatrix}^{-1} \begin{pmatrix} 1 & 1 \\ -ik_{2x} & ik_{2x} \end{pmatrix} = \frac{1}{2} \begin{pmatrix} 1+\frac{k_{2x}}{k_{1x}} & 1-\frac{k_{2x}}{k_{1x}} \\ 1-\frac{k_{2x}}{k_{1x}} & 1+\frac{k_{2x}}{k_{1x}} \end{pmatrix} \quad \text{....1.4.9}$$

Similarly, the transmission matrix at the interface from medium 2 to 3 (x=d) can be calculated to be

$$D_{23} = \frac{1}{2} \begin{pmatrix} 1+\frac{k_{3x}}{k_{2x}} & 1-\frac{k_{3x}}{k_{2x}} \\ 1-\frac{k_{3x}}{k_{2x}} & 1+\frac{k_{3x}}{k_{2x}} \end{pmatrix} \quad \text{.....1.4.10}$$

Next, both A(x) and B(x) propagating through the bulk of the layer with finite thickness d experiences a phase change of $\phi=k_{nx}d_n$, which is directly related to the refractive index and thickness of that layer. In the unit calculation cell, the two amplitudes of the electric field before and after traveling through the middle layer can be related via Eq (1.4.11)

$$\begin{pmatrix} A_2' \\ B_2' \end{pmatrix} = P_2 \begin{pmatrix} A_2 \\ B_2 \end{pmatrix} \quad \text{.....1.4.11}$$

with propagation matrix P defined as

$$P = \begin{pmatrix} e^{i\Phi_2} & 0 \\ 0 & e^{-i\Phi_2} \end{pmatrix} \quad \text{.....1.4.12}$$

Based on Eqs. (1.13) - (1.17), the amplitudes in the incident region A1, B1 and the output region A3', B3' in the calculation cell are related by Eq. (1.18)

$$\begin{pmatrix} A_1 \\ B_1 \end{pmatrix} = D_{12}P_2D_{23}\begin{pmatrix} A_3{}' \\ B_3{}' \end{pmatrix} \quad \ldots\ldots\ldots\ldots\ldots\ldots\ldots\ldots 1.16$$

The above derivation can be extended to an arbitrary multilayer structure as shown in **Figure 1.19**.

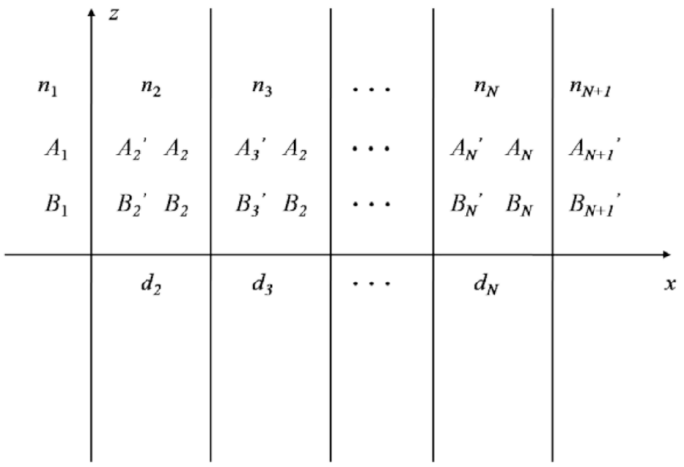

Figure 1.19. A multilayer dielectric medium

In the arbitrary multilayer case, the relationship between incident waves A1, B1 and output waves AN+1', BN+1' can be straightforwardly related via the multiplication of all the involved calculation cells in the following form

$$\begin{pmatrix} A_1 \\ B_1 \end{pmatrix} = D_{12}P_2D_{23}P_3D_{34}\ldots\ldots D_{N-1,N}P_ND_{N,N+1}\begin{pmatrix} A_{N+1}{}' \\ B_{N+!}{}' \end{pmatrix} = \begin{pmatrix} M_{11} & M_{12} \\ M_{21} & M_{22} \end{pmatrix}\begin{pmatrix} A_{N+1}{}' \\ B_{N+1}{}' \end{pmatrix} \ldots 1.19$$

where, the matrix $\boldsymbol{M}$ is the system matrix describing the entire multilayer structure. From specific components of matrix $\boldsymbol{M}$, the reflection and transmission coefficients can be extracted. Assuming light is incident from medium 1 and output from medium N+1 (i.e. B_{N+1}'=0), the reflection and transmission coefficients can be respectively described as

$$r = \left(\frac{B_1}{A_1}\right)_{B_{N+1}\prime=0} = \frac{M_{21}}{M_{11}} \quad \text{.....1.20}$$

$$t = \left(\frac{A_{N+1}\prime}{A_1}\right)_{B_{N+1}\prime=0} = \frac{1}{M_{11}} \quad \text{.....1.21}$$

Reflectance (R) and transmittance (T) are given, respectively, by

$$R = |r|^2 = \left|\frac{M_{21}}{M_{11}}\right|^2 \quad \text{.....1.22}$$

and,

$$T = |t|^2 = \left|\frac{1}{M_{11}}\right|^2 \quad \text{.....1.23}$$

1.4.2 FINITE DIFFERENCE TIME DOMAIN (FDTD) SIMULATIONS

The FDTD method solves Maxwell's equations on a discrete spatial and temporal grid. Since it is a time domain method, a vast range of frequencies can be simulated in a single run. When Maxwell's differential equations are examined, it can be seen that the change in the E-field in time (the time derivative) is dependent on the change in the H-field across space (the curl). This results in the basic FDTD time-stepping relation that, at any point in space, the updated value of the E-field in time is dependent on the stored value of the E-field and the numerical curl of the local distribution of the H-field in space.[56]

In this work, the commercially available FDTD Solutions solver in Lumerical® is primarily utilized. The FDTD solver supports a range of boundary conditions, such as perfectly matched layer, periodic, and Bloch; and supports a number of different types of sources such as point dipoles, beams, plane waves, a total-field scattered-field source, a guided-mode source for integrated optical components, and an imported source to interface with external photonic design software. A 3D CAD layout environment where structures can be built from primitive geometric objects, imported from a multilayer GDSII file or

imported via an SEM image and an extensive object library contains more than 100 pre-defined compound structures including parametric surfaces, nanoparticle distributions, and photonic crystal arrays makes modeling complex sub-wavelength geometries possible.[57]

Some simulations for larger optical resonator structures have been performed using the open source FDTD solver MEEP, developed at MIT to model electromagnetic systems. MEEP provides advantages for simulating radial optical structures by supporting cylindrical coordinate systems in 1D, 2 D, and 3 D. Exploitation of symmetries also reduces the computation size — even/odd mirror symmetries and 90°/180° rotations.

1.5 Overview of the dissertation

This work provides exciting avenues towards realizing improvements in CBRN defense through the implementation of advanced sensing platforms. Emphasis has been placed on realizing improvements in current sensing technologies while also achieving a robust and portable sensing platform, capable of deployment at point-of-care, nuclear and space environments.

Chapter 2 provides detailed characterizations of the PSi substrate that forms the primary sensing platform for the chemical, biological and radiation sensors presented in this work.

Chapters 3 – 4 tackle the development of labeled and label-free sensing platforms with the end goal of achieving smartphone compatible, portable diagnostic platforms that offer improved detection capabilities over currently existing platforms.

Chapters 5 – 6 explore the material systems of QDs and PSi as a basis for the development of QD based radiation sensors.

Chapter 7 provides a summary of the conclusions reached in all the projects described and demonstrates initial research studies that can further drive improvements in the sensing technologies already demonstrated in this work.

2. POROUS SILICON SUBSTRATE CHARACTERIZATIONS

2.1 Introduction

The morphology of PSi depends not only on the etching parameters used during fabrication but also on silicon wafer characteristics such as type of dopant, resistivity, and orientation. Knowledge of the pore size distribution in a given film is essential for sensing applications in order to estimate the ability to form sufficient linker molecule chains within the pores, understand the balance between efficient infiltration of target molecules and natural filtering of large contaminant species whose presence in the pores might lead to false positive sensor readings. Knowledge of the number of pores and associated surface area available for molecular binding inside the pores is critical for understanding how many small molecules or chemicals can be captured by these porous sensors,[24] ensuring measurable detection sensitivities, and optimized integration of QDs with the porous 3D scaffolds.

2.2 SEM Image Analysis

In order to accurately model the properties of the PSi films, top-view and cross-sectional scanning electron microscopy (SEM) images using a Hitachi S-4200 SEM, were analyzed to determine pore size distributions, number of pores, and the available surface area for molecular binding events. Samples were mounted on the sample holder using

carbon tape. An accelerating voltage of 10 kV was used during sample imaging. Thresholding of the gray-scale top-view SEM images of PSi in MATLAB yields binary images that allow for straightforward differentiation between the pores and the silicon pore wall framework. After noise removal using mathematical morphological openings and closings on the thresholded image,[58] pore areas in pixel count were extracted using the function regionprops in MATLAB. The image processing analysis steps are outlined in **Figure 2.1** using a representative porous silicon sample. The pore areas were then expressed in nm^2 by application of a conversion factor based on the ratio of the SEM scale bar pixel count to the corresponding length in nm. All pores were approximated to cylinders and the effective pore diameters were calculated from the extracted pore areas.

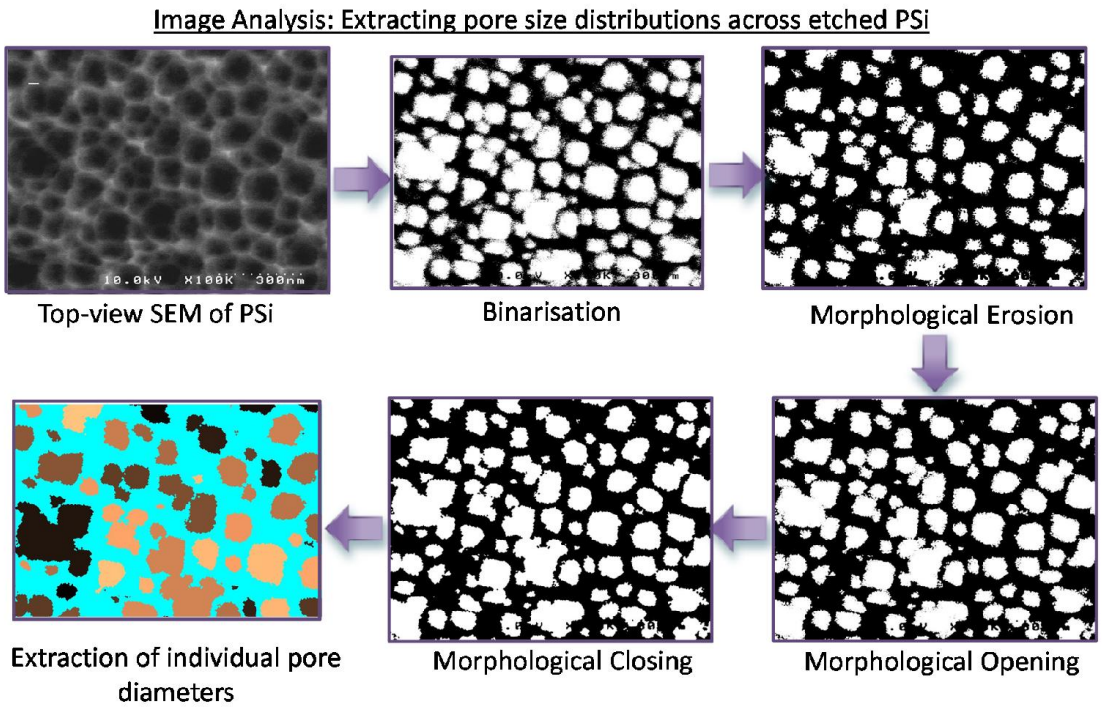

Figure 2.1. Image processing analysis steps on a representative porous silicon SEM image that help in identifying individual pore geometries.

2.3 Porosity and Surface Area Estimates

For our initial characterization study, several PSi films of the same nominal thickness were formed under different applied current densities to understand the range of achievable pore sizes, porosities, and morphologies. The etching parameters for these ~5.5 μm thick PSi films are presented in **Table 2.1**. Porosity calculations were based on gravimetric analysis of the PSi layers. **Figure 2.2** shows top-view SEM images with the corresponding pore size histograms derived from SEM image analysis. Based on the results shown in **Figure 2.2** and the corresponding fabrication conditions in **Table 2.1**, we find that increasing the etching current density results in larger pore sizes with cylindrical pore geometries, higher porosities, fewer side branches, and a slightly broader pore size distribution (**Figure 2.3**). These trends agree well with previously reported results.[43, 44]

Table 2.1. Fabrication conditions for ~5.5 μm thick PSi films with different average pore sizes.

Average Pore Diameter [nm]	% Porosity (± 2.5%)	Etching Current Density [mA cm^{-2}]	Etching Time [s]
30	82	60	190
25	75	48	200
20	67	40	210
15	60	20	510
12	55	5	1200

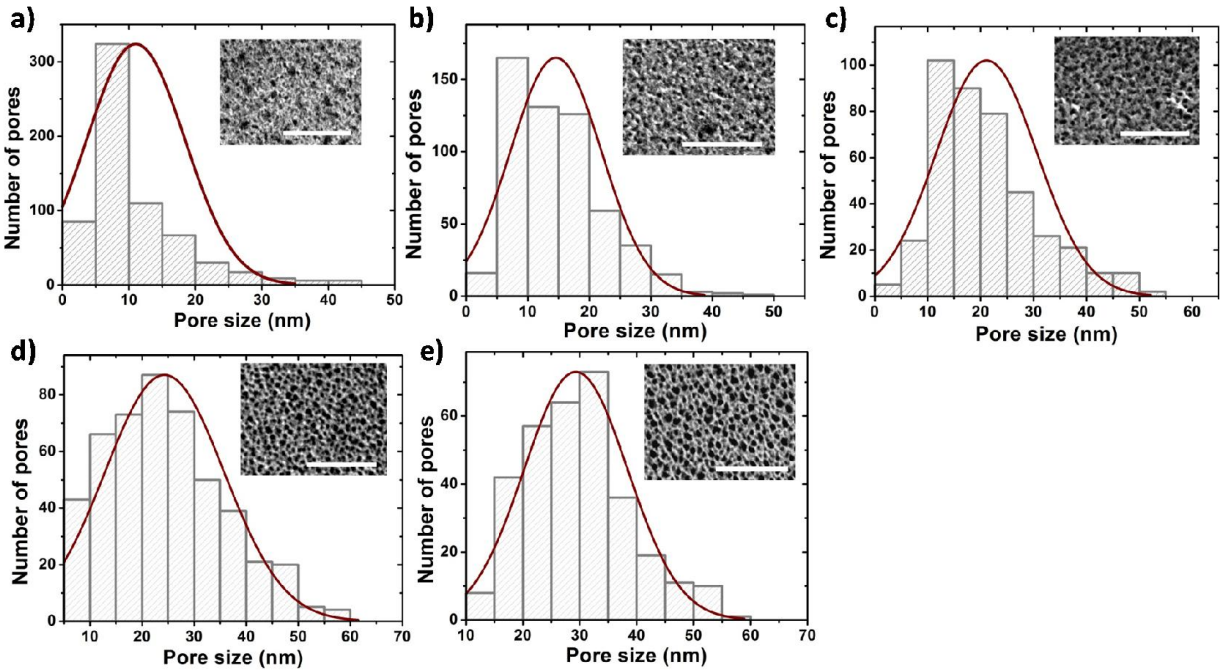

Figure 2.2. Top-view SEM images of PSi films and the corresponding pore size distributions. The etching conditions for these films are given in Table 1. a) 12 nm average pore size (□ = 7.87 nm), b) 15 nm average pore size (□ = 6 nm), c) 20 nm average pore size (□ = 10.35 nm), d) 25 nm average pore size (□ = 11.21 nm) , and e) 30 nm average pore size (□ = 9.78 nm). All SEM scale bars indicate 375 nm.

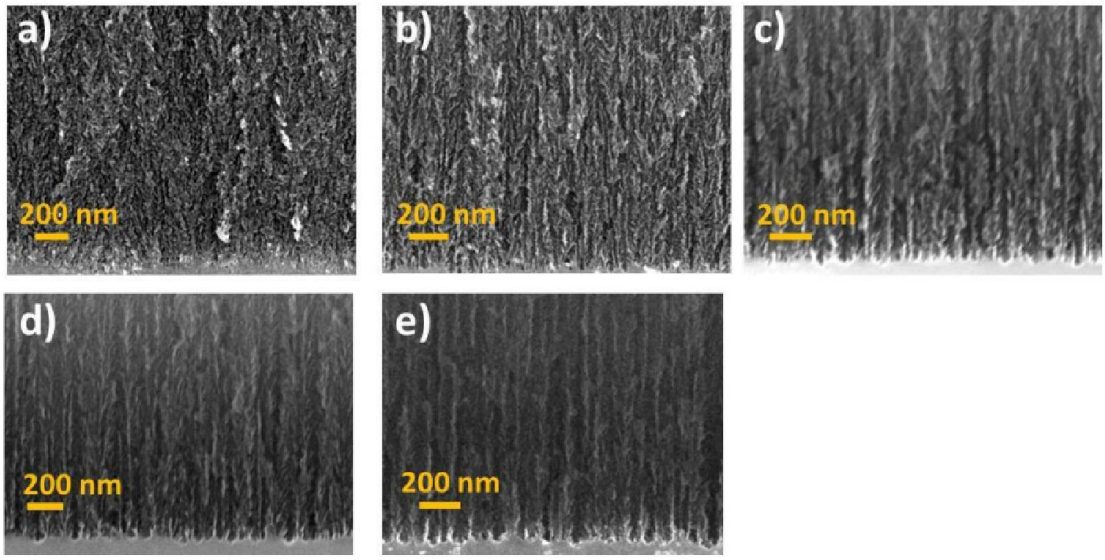

Figure 2.3. Cross-sectional SEM images of PSi films. a) 12 nm average pore size, b) 15 nm average pore size, c) 20 nm average pore size, d) 25 nm average pore size , and e) 30 nm average pore size. Larger pore diameters (20 nm, 25 nm and 30 nm) conform more closely to an ideal cylindrical shape as compared to the smaller (12 nm and 15 nm pores), more branchy pores.

Figure 2.4 shows quantification of the decrease in PSi surface area that accompanies increasing average pore diameters and increasing porosity.

For the surface area calculations, pores have been assumed to be cylindrical. This approach underestimates the total surface area in the porous matrix as it neglects the surface area contribution from the side branches. Hence, the surface areas reported should be taken as lower bound values.

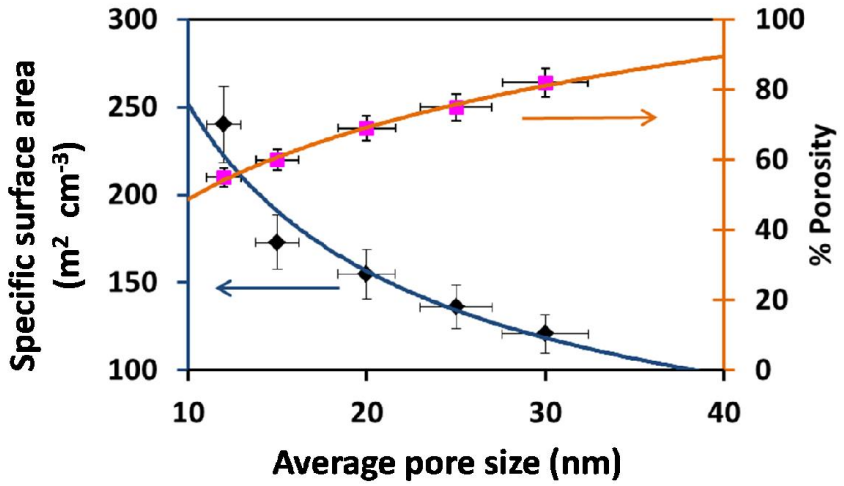

Figure 2.4. Inverse relationship between PSi surface area and porosity as a function of average pore size.

The surface area on all samples examined was ≥ 100 m^2 cm^{-3}, which represents a very large active sensing region for molecular detection. There is a natural tradeoff between available surface area for molecular attachment and ease of infiltrating molecules into larger and more open porous frameworks. We note that the surface functionalization procedures for sensing applications must be carefully tuned to allow for high target molecule capture relative to the available surface area. For example, a sufficient number of probe molecules must be immobilized in the pores to ensure that target molecule capture leads to a measurable sensor output.

2.4 Summary

This chapter provides a detailed characterization of the fabricated porous silicon samples. This forms the basis of the development of highly sensitive small molecule

sensors, analysis of the QD PL dependence upon the porous silicon substrate as well as foundational studies on the interaction of high energy radiation with the QDs that will be covered in **Chapter 6.**

3. QUANTUM DOT SIGNAL AMPLIFIERS FOR DUAL-MODE OPTICAL BIOSENSING

3.1 Introduction

In recent years, biocompatible luminescent colloidal quantum dots (QDs) have gained increasing attention for numerous biomedical applications such as fluorescent tags in biomarkers, immunoassays, guided drug delivery, cellular imaging, and fluorescence resonance energy transfer (FRET) based sensors.[59-64] The unique photophysical properties of QDs, including high quantum yield, resistance to photobleaching, broad excitation spectra, tunable by nanometer size and structure, fluorescence that spans the UV-visible-NIR spectrum and bioconjugation capabilities make them a favorable choice for meeting the increasing demands of high sensitivity, stability, and rapid signal transduction in the early detection of toxins, disease markers, chemical species, and environmental bio-agents.[65-70] However, most QD-labeled sensing platforms to date have focused on using the strong fluorescence spectra of protein- or DNA-conjugated QDs for target molecule detection via fluorescence immunoassays or FRET.[71-74] Although FRET based biosensing has demonstrated sensitivities down to the single molecule, the method is hindered by the extreme sensitivity to distance between donor and acceptor molecules and the requirement for spectral overlap between donor emission and acceptor absorption for efficient energy transfer.[75-77] The conveniently high refractive index of QDs compared to that of conjugated protein or DNA molecules is a potential advantage for sensor platforms that has been left largely unexploited. In this work, we utilize the simplicity of fluorescence based optical

detection of QD-conjugated biomolecules and combine it with the ability to quantify captured target molecules in thin films via monitoring changes in the effective refractive index of the film by reflective interferometric spectroscopy to achieve a novel, dual-mode, optical porous silicon (PSi) sensor.

Our choice for selecting a porous silicon (PSi) film for QD-labeled biomolecule detection stems from the many advantages that PSi has to offer as a sensor platform, such as tunable pore dimensions and film thicknesses, high surface area (> 100 m^2 cm^{-3}), ease of surface modification, and inherent size-selective filtering of contaminant molecules.[8, 17, 23, 78-79] These advantages have led to the emergence of many PSi based label-free biosensors,[27, 80-81] as well as the implementation of PSi films and membranes in fuel cells,[82-84] solar cells,[18, 85-86] drug delivery vehicles [87-91] and cellular imaging host matrices [92-94]. For all of these applications, PSi pore size distributions, pore morphologies, available surface area for binding events to take place, and stable surface functionalization procedures play a crucial role. The comprehensive step-by-step characterization of the PSi platform described in **Chapter 2 Section 1** along with Fourier transform infrared spectroscopy (FTIR) has been used to more accurately enable estimation of infiltration efficiency, quantification of captured molecules in the nanoporous matrix, and optimization of the PSi sensor for maximum signal transduction depending upon the size of target infiltrated species. With a well-characterized and appropriately functionalized PSi matrix, we demonstrate the specific detection of biotin molecules conjugated with low-toxic $AgInS_2$/ZnS (AIS/ZnS) QDs through both reflectance and fluorescence measurements. The QDs serve both as high refractive index signal amplifiers for the reflectance

measurements that can quantify the number of molecules captured and as fluorescent emitters whose characteristic emission wavelength confirms molecule capture in the functionalized pores. We note that intermediate QD carrier nanoparticles and additional biomolecule labeling are not necessary using our approach [95]. Moreover, an extremely competitive detection sensitivity of 6 fg mm^{-2} for biotin molecules is shown and we anticipate that a sub-fg mm^{-2} detection limit is readily achievable.

3.2 QD Synthesis

Synthesis of PbS Quantum Dots: PbS QDs were prepared using a reported procedure.[96-97] The QDs synthesis was carried out inside a glove box under nitrogen atmosphere. Briefly, 2 mmol of lead (II) oxide (PbO, 99.99%, Acros Organics), 2.7 mmol of oleic acid (OA, Aldrich) and 4 mL of octadecene (ODE, Lancaster) were mixed in a 25 ml three neck flask under a magnetic stirring. After degassing and purging by argon at 80 °C the mixture was subsequently heated to 140 °C. After complete dissolution of PbO, the solution was cooled to 120 °C and 2 mL of ODE with bis(trimethylsilyl)sulfide (1 mmol, 98%, Alfa Aesar) was rapidly injected into the solution under constant stirring. After the temperature decreased to 110 °C, resulting from the injection of the precursor, an additional 2 mL of ODE was added into the solution. Growth of the QDs was carried out at 100 °C for 30 s. Synthesized QDs were then removed from the reaction vessel with a glass syringe. The resulting PbS QDs were purified twice by acetone precipitation from chlorofom solution and centrifugation to remove unreacted precursors. Finally, the desired PbS QDs were redissolved in hexane, yielding an optically clear brown solution. By controlling chemical

synthesis conditions and the concentration of precursors, different sizes (2.8 nm and 7.5 nm) of PbS QDs were prepared.

Transmission Electron Microscopy (TEM): HRTEM analysis was performed using a Philips CM20 TEM operating at 200 kV. The samples for TEM investigation were prepared by dropping a solution of washed QDs onto carbon coated copper grids.

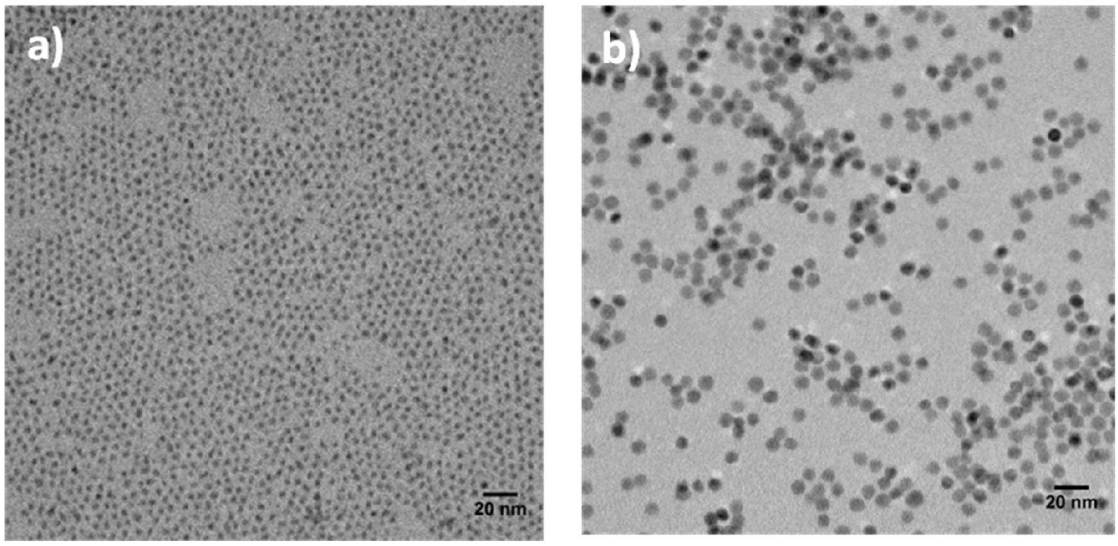

Figure 3.1. HR-TEM micrographs of (a) 2.8 nm and (b) 7.5 nm PbS QDs

Synthesis and functionalization of $AgInS_2$/ZnS (AIS/ZnS) Quantum Dots: $AgInS_2$/ZnS QDs were synthesized by a procedure published elsewhere [98-99]. The single source precursor $(AgIn)(S_2CN(C_2H_5)_2)_4$ was prepared directly through the precipitation of stoichiometric amounts of indium acetate ($In(CH_3COO)_3$, 99%, Alfa Aesar), silver nitrate ($AgNO_3$, 99.8%, Aldrich) and sodium diethyldithiocarbamate ($Na\ S_2CN(C_2H_5)_2S \cdot 3H_2O$, 98%, Alfa Aesar) in DI water. $Zn(S_2CN(C_2H_5)_2)_2$ was prepared in the same manner using zinc acetate ($Zn(CH_3COO)_2$, 99.98%, Alfa Aesar). Both precursors were *thoroughly* washed by water

and dried in a vacuum before further use.

In the synthesis of $AgInS_2$ (AIS) QDs, a previously degassed mixture of 50 mg of precursor and 3 mL of oleylamine (OLA, Aldrich) was heated to 180 °C under a stream of Ar and constant magnetic stirring. After allowing QDs to grow for 8 min, the brown solution was removed by a syringe. After being cooled to room temperature, the QD solution was separated from large agglomerates by centrifugation at 4500 rpm for 10 min. AIS QDs were then washed from unreacted precursor by precipitating with 10 mL of acetone and isolated by centrifugation and decantation. To grow the ZnS shell, the AIS QDs and 10 mg of $Zn(S_2CN(C_2H_5)_2)_2$ were redissolved in 3 mL of OLA. The mixture was degassed and subsequently heated to 180 °C for 20 min. The prepared AIS/ZnS QDs were subjected to a washing procedure as described for AIS QDs. Finally AIS/ZnS QDs were dissolved in 1 mL of chloroform.

Water solubilization of AIS/ZnS QDs was achieved using a ligand exchange strategy described in Refs. [100-102]. Typically, 1 mL of glutathione (GSH, 30 mg, 98%, Acros Organics) methanolic solution with pH adjusted to 12 by tetramethylammonium hydroxide (TMAH, 25 % solution in methanol, Acros Organics) was added dropwise to a chloroform solution of QDs (30 μmol) under constant stirring. The solution was left while stirring for 24 hours. Then, 1 mL of water was added and the mixture was kept stirring for another hour. After being transferred into upper aqueous phase, the QDs were isolated and washed with acetone several times before finally being dissolved in water. GSH functionalized QDs were washed from excess ligands using a Microcon Centrifugal Unit (Ultracel YM-10, MWCO=10,000).

AIS/ZnS QDs were conjugated to biotin according to the following protocol.[103] 1μmol of GSH coated AIS/ZnS QDs were incubated with 0.5 mg of sulfo-NHS-biotin in PBS buffer for 30 min at room temperature. After incubation, biotin conjugated QDs were washed from the excess of unreacted sulfo-NHS-biotin using the Ultracel YM-10.

3.3 Porous Silicon Thin-Film Fabrication

A 5.5% aqueous HF solution was used to etch n+ wafers (30 mA/cm^2, 275 s) for demonstration of QD infiltration and attachment in fairly large pore sizes (**Section 3.5.1.1**). For the n-type wafers, it has been previously shown that the initial pore formation leads to narrow pore openings that widen as the pores continue to propagate into the bulk.[104] Consequently, a ~800 nm sacrificial layer (40 mA/cm^2, 30 s) was initially etched for n-type wafers and subsequently removed by an electropolishing step (250 mA/cm^2, 3 s). This electropolish step ensures wide pore openings at the top of the n-type PSi layer and facilitates the infiltration of nanoparticles into the PSi framework. The average pore diameter for the n-type PSi was 70 nm.

For the thickness dependent studies in **Section 3.5.1.2**, the following etching conditions were used. For set 1: A current density of 5 mA cm^{-2} was applied for etching times of 400 s, 800 s, 1200 s, and 1600 s to form PSi films with an average pore diameter of 12 nm and thicknesses of 2 μm, 3.75 μm, 5.5 μm, and 7.25 μm, respectively. For set 2: A current density of 48 mA cm^{-2} was applied for etching times of 67 s, 133 s, 200 s, and 267 s to form PSi films with an average pore diameter of 25 nm and thicknesses of 2 μm, 3.75 μm, 5.5 μm, and 7.25 μm, respectively. For pore size dependent QD attachment in PSi

(**Section 3.5.1.3**), etch parameters as listed in **Table 3.1** were used. The average pore size and porosity estimates were based on calculations discussed in **Chapter 2**.

Table 3.1. Fabrication conditions for ~5.5 μm thick PSi films with different average pore sizes.

Average Pore Diameter [nm]	%Porosity (± 2.5%)	Etching Current Density [mA cm^{-2}]	Etching Time [s]
30	82	60	190
25	75	48	200
20	67	40	210
15	60	20	510
12	55	5	1200

For the biosensing studies in **Section 3.5.2**, 2 μm thick PSi films with ~30 nm average pore diameters were fabricated by applying a current density of 60 mA cm^{-2} for 66 s.

3.4 Surface Functionalizations

Organic solvents used were of analytical reagent grades. The chemicals were used without further purification.

PSi films were functionalized for two sets of experiments. The initial experiments performed with PbS quantum dots required only amine functionalization of the PSi. For these experiments, PSi samples were thermally oxidized in air at 800 °C for 30 min (Omegalux LMF-3550 Oven) forming a SiO_2 layer and characteristic Si-O-Si bonds. The samples were then rinsed with ethanol and dried under a stream of nitrogen to remove any organic surface contaminants deposited on the sample surface during oxidation. The clean oxidized PSi samples were incubated in a freshly prepared 4% 3-

aminopropyltriethoxysilane (APTES) solution [50:48:4 = de-ionized water : methanol : APTES (99% Aldrich)] for 20 min in a moist environment to provide an amine functionalized surface. The excess of unreacted APTES was thoroughly rinsed from the samples three times with ethanol and de-ionized (DI) water, dried under nitrogen flow and baked in an oven at 100 °C for 10 min to increase the cross-linking density. The 0.8 nm APTES molecules form an almost uniform monolayer over the entire PSi surface.[105] Note: By subjecting oxidized PSi samples to oxygen plasma or nitric acid, the formation of a more uniform silane layer may be possible. Both these processes result in the formation of reactive –OH groups at the silicon surface. The amine-functionalized PSi films were exposed to a 0.44 mg mL^{-1} PbS QD solution for 24 hrs in order to ensure saturation of all binding sites, following results from previous studies. [106] The films were then rinsed thoroughly with anhydrous hexane to remove all unbound QDs. The second set of expertiments performed with biotin molecules and biotinylated-$AgInS_2$/ZnS QDs required additional functionalization of the PSi films. After silanization with 3-APTES, the PSi films were exposed to the homobifuctional cross-linker glutaraldehyde.[107-108] The films were incubated in 2.5% glutaraldehyde solution, formed by mixing 50 µL of 50% aqueous glutaraldehyde (Aldrich) with 950 µL of HEPES buffer (20 mM HEPES, 150 mM NaCl, 5 mM EDTA, pH=7.4), for 30 minutes. Excess glutaraldehyde solution was removed and 1 µL of sodium cyanoborohydride (5M cyanoborohydride, 1M NaOH, Aldrich) in 100µL of HEPES buffer was pipetted onto the PSi sensor in order to stabilize the Schiff base (C=N) formed during reaction of the aldehyde group with the amine group. After 30 minutes of incubation with the reducing agent, the PSi films were thoroughly rinsed with HEPES

buffer to remove any unreacted glutaraldehyde from the nanoscale pores. A schematic representation for the surface functionalization steps is provided in **Figure 3.2**.

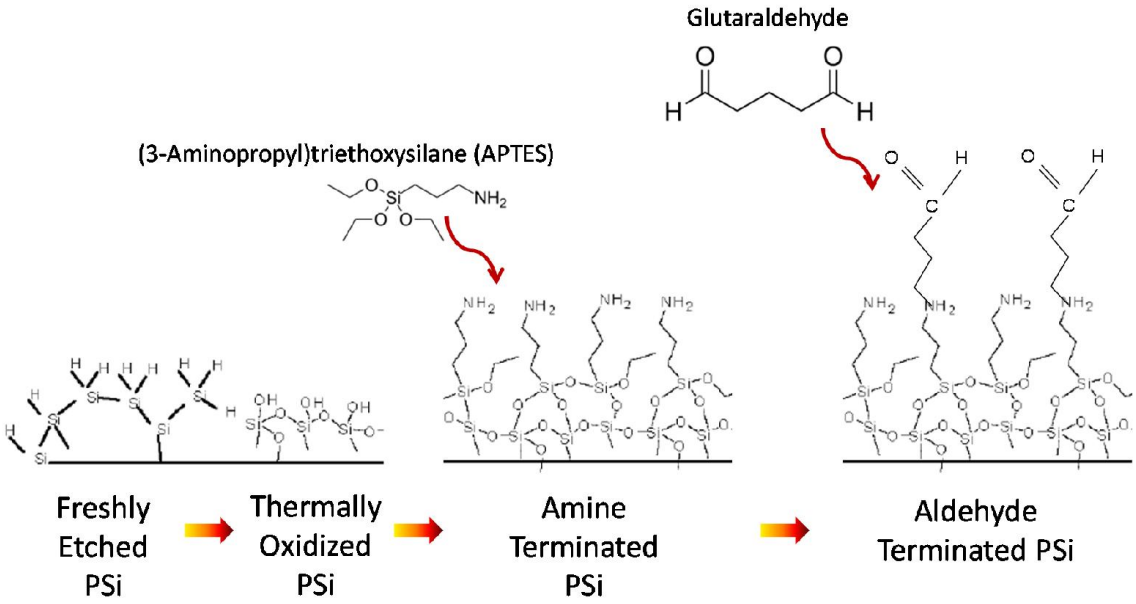

Figure 3.2. Schematic representation of the surface functionalization steps of PSi. Adapted from [109].

Next, 100 µL of 10 µM streptavidin solution in PBS buffer was then pipetted onto the PSi sensor and incubated for 30 min. An incubation time of 30 min was found to be sufficient to ensure maximum attachment of target molecule as reported previously.[106] Thereafter, the reducing step with sodium cyanoborohydride was repeated in order to stabilize the Schiff base formed during streptavidin fixation to the pore walls. To close any unreacted aldehyde groups for minimizing non-specific binding, 3M ethanolamine (>99% ethanolamine, Aldrich) in buffer, with pH adjusted to 9.0, was pipetted onto the PSi sensor

and incubated for 30 minutes. [21] The PSi sample was then thoroughly rinsed with buffer and DI water and dried under air.

For the labeled detection measurements, the PSi sensor was exposed to 100 μL of a 500 μM solution of QD-biotin conjugates and incubated for 30 min. The sample was then thoroughly rinsed with buffer and DI water, and then dried under air. For label-free detection, 100 μL of 200 μM sulfo-NHS-biotin (Sigma Aldrich) solution in HEPES buffer was pipetted onto a streptavidin (Sigma Aldrich) functionalized PSi sensor. This high concentration ensured that all accessible streptavidin binding sites were hybridized with biotin as higher concentration solutions produced the same reflectance fringe shift. Following incubation of the sample in the biotin solution for 30 min, the samples were rinsed with buffer and DI water, and then dried under air. By following a thorough Piranha cleaning procedure, the covalently bound organics and QDs may be removed to allow for re-useability of the sample surface. A quick O_2 plasma clean can ensure removal of the covalently bound silane cross-linkers. This removal of the silane monolayer is commonly referred to ashing.

In our studies to evaluate the infiltration efficiency of various sized species in PSi films of different thicknesses with the pore size distributions shown in **Figure 2.1** (**Chapter 2**), an amine termination was needed. **Figure 3.3** shows the FTIR spectra for a PSi film after anodization, thermal oxidation, and silanization with 3-aminopropyltriethoxysilane to form the amine termination. Measurements were conducted using a Tensor 27 FTIR spectrometer (Bruker Optics Inc.) equipped with the Seagull variable angle reflection accessory (Harrick Scientific Products Inc.) for specular

reflectance measurements from solid surfaces and Opus 5.5 software. FTIR spectra were collected in 84 scans at a 4 cm^{-1} resolution in a nitrogen purged compartment.

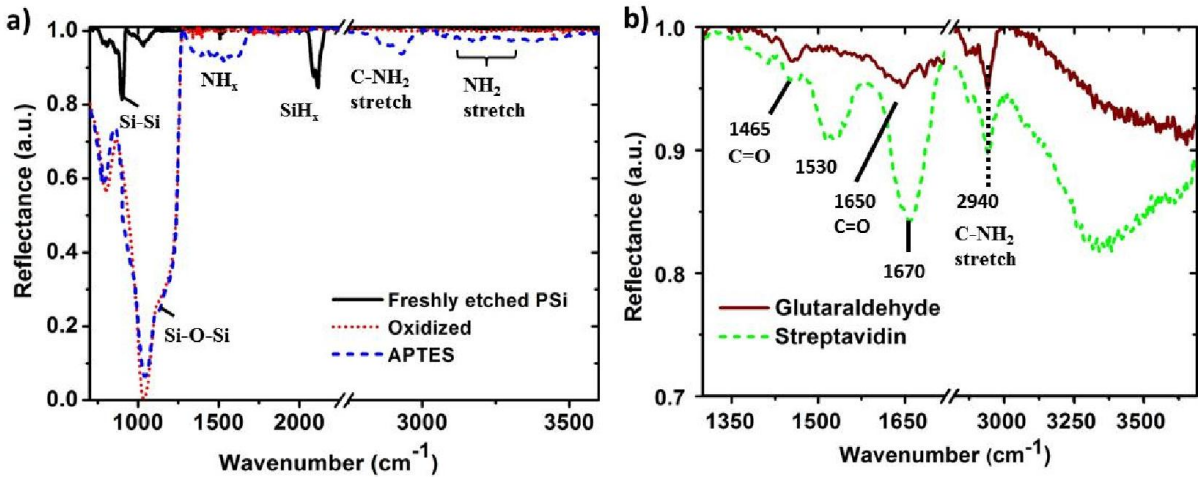

Figure 3.3. a) FTIR measurements in reflectance mode of a freshly anodized PSi sample that subsequently undergoes thermal oxidiation and APTES surface modification. b) FTIR spectra of same sample after attachment of glutaraldehyde and streptavidin for QD-biotin conjugate detection in PSi.

For the as-anodized film, resonances near 2105 cm^{-1} and 2115 cm^{-1}, corresponding to SiH_x bonds, confirm the expected hydride termination. After thermal treatment, the PSi film exhibits absorption resonances near 1040 cm^{-1} and 1140 cm^{-1}, indicating the presence of Si–O–Si bonding and confirming oxidation of the PSi film. Silanization of the oxidized PSi film results in several distinct features appearing in the FTIR spectrum that demonstrate the presence of amino groups on the surface. The broader resonances near 3300 cm^{-1} represent NH_2 stretch vibrations while the two resonances at 2880 cm^{-1} and 2940 cm^{-1}

specify the -C-NH_2 stretch vibration. Moreover, siloxane bond formations between silane and the hydroxyl terminated groups on oxidized PSi are seen between the region 1300 cm^{-1} and 1730 cm^{-1} with small peaks near 1407 cm^{-1}, 1508 cm^{-1}, 1575 cm^{-1} and 1650 cm^{-1} corresponding to the CH_3 group of APTES, symmetric $–NH^{3+}$ deformation mode, NH_2 scissoring vibration mode, and the asymmetric $–NH^{3+}$ deformation mode, respectively.[45] For the sensing studies of the biotin-streptavidin pair (Section 4), additional functionalization steps were required and the associated FTIR spectra are shown in Figure 3b. Glutaraldehyde binding with silane can be confirmed from the resonances at 1650 cm^{-1} and 1872 cm^{-1} (not shown) due to C=O stretching of the aldehyde group and at 1465 cm^{-1} arising from the C=O vibration mode. A more distinct peak formation at 2940 cm^{-1} can be attributed to the C-H stretching modes from glutaraldehyde functionalization. Peaks representing amide bonds of streptavidin are detected near 1529 cm^{-1} and 1670 cm^{-1}. A very broad peak in the region between 3100 cm^{-1} and 3600 cm^{-1} indicates the presence of exchangeable protons from the amide peptide groups of streptavidin and due to the O-H and N-H stretching modes of glutaraldehyde and streptavidin.

3.5 Experimental Results

3.5.1 Characterization of QD infiltration and binding in PSi films

3.5.1.1 QD Infiltration and Immobilization in PSi

PSi films with fairly large pore sizes were used to test for QD infiltration and immobilization along the length of the pores. The amine-functionalization on the PSi films

as discussed in **Section 3.4** ensured that a monolayer of PbS QDs could be covalently attached to the pore walls.

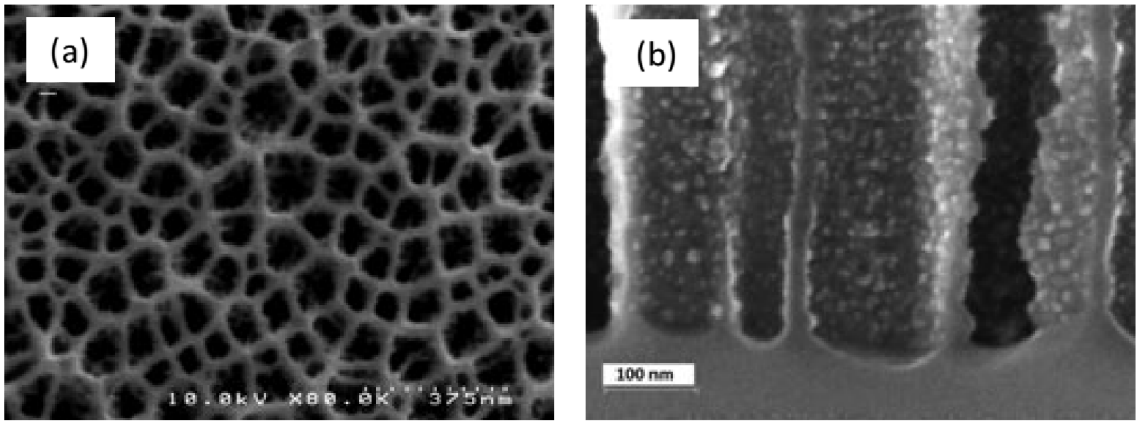

Figure 3.4. (a) Top view and (b) cross-sectional view SEM images of n-type PSi (70nm average pore openings) coupled with ~7.5nm PbS QDs. The surface coverage of PbS QDs is relatively uniform throughout the PSi framework.

Figure 3.4 shows scanning electron microscopy (SEM) images of PbS QDs coupled to a PSi framework with 70 nm pores. For this sample, reflectance spectra measured before and after coupling PbS QDs with the PSi revealed a ~35 nm shift in the fringe peak positions near a wavelength of 1000 nm. Applying a fast Fourier transform (FFT) to the reflectance spectra enabled estimation of the optical thickness of the PSi layer before and after QD infiltration, given by $2nL$ where, n is the effective refractive index of PSi and L is the thickness of the PSi layer.[106] The relative increase in optical thickness after PbS attachment was found to be ~3%. Corresponding transfer matrix simulations suggest

that the measured reflectance fringe shift and associated optical thickness increase upon QD attachment correspond to ~20% QD coverage on the pore walls.

3.5.1.2 Dependence of PSi-QD coupling on PSi film thickness

Studies were conducted to explore the infiltration efficiency of QDs into PSi films in order to verify that QD-labeled biosening in nanoscale pores is feasible. First, the dependence of PSi-QD coupling on PSi film thickness was evaluated by studying the uniformity of QD surface coverages on the pore walls and to determine how deeply QDs infiltrate into PSi films. Next, the influence of the pore size on QD infiltration efficiency was explored. PbS QDs, 2.8 nm in size, were selected for these initial studies.

In order to investigate the uniformity of QD surface coverage in PSi films, two sets of amine-functionalized PSi layers of 2 μm, 3.75 μm, 5.5 μm and 7.25 μm thickness were fabricated: one set had an average pore size of 12 nm and the other 25 nm. The relative change in effective index due to QD infiltration should remain constant across different PSi film thicknesses if the QDs infiltrate uniformly throughout the films. **Figure 3.5a** shows a schematic illustration of a PSi film before and after QD infltration and the associated reflectance spectra for one of the films in the study. **Figure 3.6** shows the representative red-shift in reflectance spectra over an expanded wavelength of 500 nm to 2000 nm.

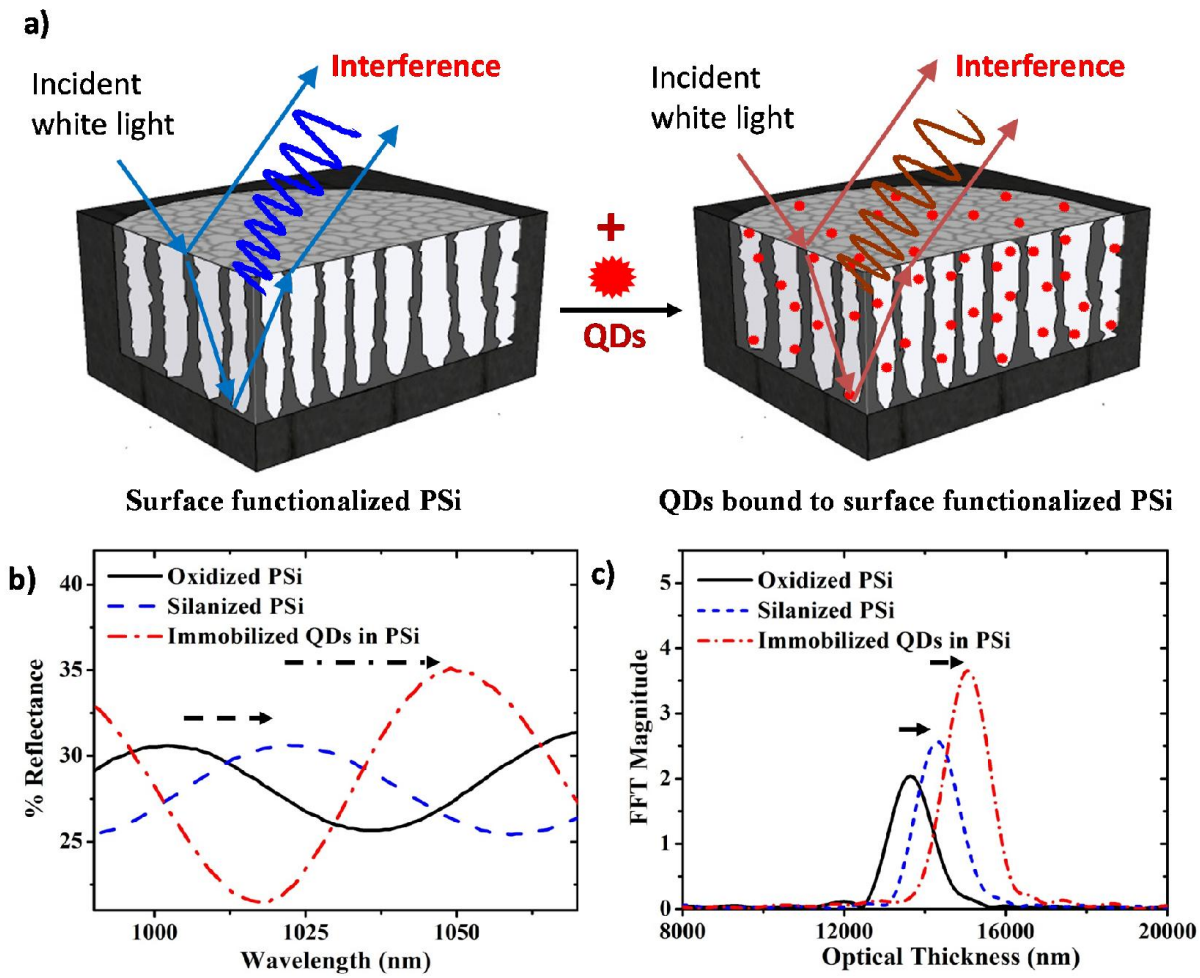

Figure 3.5. (a) Schematic representation of surface functionalized PSi film before and after attachment of QDs. Light reflecting off the top and bottom interfaces of the film interfere and produce characteristic Fabry-Perot fringes. (b) Reflectance fringe shifts and (c) increase in EOT for an oxidized ~5.5 μm thick PSi layer with 20 nm average pore diameter after APTES surface functionalization and immobilizing 2.8 nm PbS QDs. The increase in spectral shift and FFT amplitude demonstrate that QDs are being covalently bound to the functionalized pore walls.

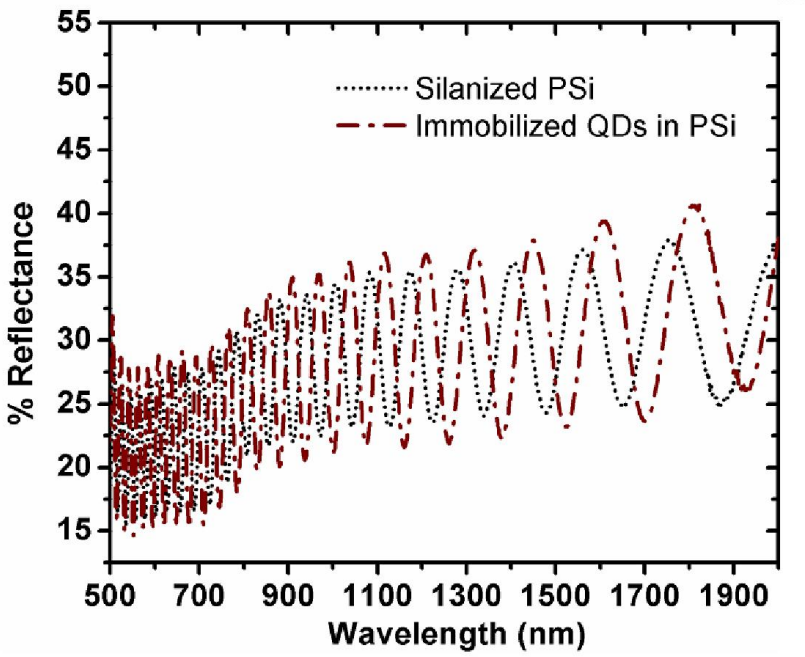

Figure 3.6. Reflectance spectra over an expanded wavelength range for PSi silanized with APTES before (dotted line) and after (dash-dot line) the immobilization of small (2.8 nm) PbS QDs on the pore walls.

The red shift of the reflectance spectra suggests that both amine linker molecules and the small QDs are successfully added to the PSi film. In order to provide a direct way of quantifying the effective refractive index of the different PSi layers and the associated changes in effective optical thickness (EOT) of the films upon inclusion of APTES and QDs, fast Fourier transform (FFT) analysis of the collected white light reflectance spectra was performed. [8,110] The Fabry-Perot relationship for thin film interference states that the reflectance fringe maxima are described by the relationship given by equation (1).

$$m\lambda = 2nL \qquad (1)$$

Here λ is the wavelength of incident light, n is the refractive index of the material, L is the film thickness, and m is an integer. Taking a FFT of the reflectance data as a function of wave number using a Hamming window produces a peak corresponding to the term *2nL,* which is the EOT of the PSi layer.[8] **Figure 3.5c** shows the EOT data corresponding to the reflectance data in **Figure 3.5b**. APTES attachment results in an EOT of 122 nm while QD attachment results in a larger 488 nm increase due to the higher refractive index and larger size of the QDs. The magnitude of the FFT peaks corresponds to the ratio of effective refractive index contrast at each layer interface. With the addition of material to the porous matrix, the effective refractive index of the PSi layer increases; accordingly, the FFT peak height increases after each infiltration step in the study.

The relative EOT increase of all PSi films examined in this study after QD coupling is shown in **Table 3.2**.

Table 3.2. Relative increase in optical thickness of PSi films after coupling with 2.8 nm QDs. All data points represent the average of measurements from at least two different samples.

Layer Thickness [μm]	Relative increase in EOT of PSi layer $\Delta nL/(nL_0)$	
	25 nm pores	10 nm pores
2.00	0.042 ± 4.1 %	0.024 ± 5 %
3.75	0.043 ± 3 %	0.023 ± 4.4 %
5.50	0.043 ± 3.2 %	0.025 ± 4 %
7.25	0.040 ± 3.1 %	0.024 ± 4.2 %

The uniform relative increase in EOT for all the PSi films with a given pore size suggests that 2.8 nm PbS QDs can effectively infiltrate PSi films with diameters equal to or greater than 12 nm to at least a thickness of 7.25 □m with a uniform surface density distribution. The surface density of the QDs, however, is different for PSi films with different pore

diameters, as is further explored in **Section 3.5.1.2**. Note that the uniform relative increase in EOT for films with the same average pore diameter corresponds to an almost linear increase in the PSi effective refractive index with increasing layer thickness. The uniform infiltration and attachment of QDs in the porous matrix demonstrates that sensors based on PSi films can utilize the entire accessible surface area of the porous matrix without being limited to probing only the sensor top surface. We note that energy dispersive x-ray spectroscopy was also performed (**Figure 3.7**) to further verify that the PbS QDs are bound inside the pores of the films. The elemental presence of lead and sulfur within the porous matrix was confirmed. This result agrees well with previously reported research in which SEM images showed that 7.5 nm PbS QDs were uniformly coupled with the pore walls of a PSi film with 70 nm pores. [106]

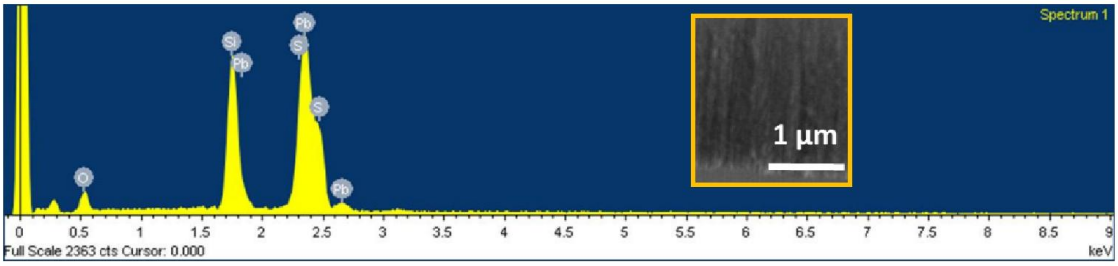

Figure 3.7. EDX spectra from cross-sectional PSi + QD sample with ~25 nm pores. The inset shows the cross-sectional SEM image of the sample that was used for the EDX analysis.

3.5.1.3 Dependence of PSi-QD coupling on PSi pore size and QD size

In order to understand the relationship between QD size and PSi pore size, experiments were performed to infiltrate two different sized PbS QDs (~ 2.8 nm and

~7.5 nm, as shown in **Figure 3.1**) into 5.5 □m thick PSi films with five different average pore diameters (12, 15, 20, 25, and 30 nm).

In general, the ease of infiltrating species into a nanoporous framework increases with increasing pore sizes. However, as shown in **Chapter 2 Figure 2.4**, the available specific surface area for immobilizing species inside the porous matrix decreases with an increase in pore size, which limits the number of available binding sites. In order to maximize detection sensitivity for sensors based on porous materials, the trade-off between the pore size to target QD size ratio and the specific surface area needs to be balanced such that pore sizes are large enough to allow for infiltration of targeted biological or chemical species into the porous matrix while providing the maximum possible specific surface area for immobilization.

Transfer matrix simulations[111] were performed to estimate the number of surface bound QDs and the percent surface area coverage of the QDs in the different PSi films. The simulations modeled the experimental shift in reflectance measurements after QD attachment and the corresponding increase in EOT; with a known thickness of each film, the reflectance shift and resulting increase in EOT can be modeled accurately by changing the effective refractive index of the film. The Bruggeman effective medium approximation is then applied to estimate the effective volume fill fraction of QDs necessary to achieve the simulated change in effective refractive index by taking into account the size of the QDs, the effective refractive index of the surface functionalized PSi, and the refractive index of the QD layer. Note that the refractive index of the QD layer was taken to be the bulk refractive index of PbS (n = 4.15), which likely results in a slight overestimation of

the refractive index for the QDs and a slight underestimation in the volume fill fraction of the QDs [112]. From the volume fill fraction of QDs, the number of coupled QDs on the pore walls can be estimated and, taking into account the total specific surface area for binding events to take place from **Figure 2.4**, QD densities on the pore walls and their percentage surface area coverages can be estimated.

Table 3.3 summarizes the results for the ten PSi samples, showing QD densities and percent surface area coverages. High surface densities of approximately 10^{15} m^{-2} are achieved in the surface functionalized PSi. The surface area coverage of the QDs is slightly smaller but in the same range as that reported for DNA molecules in PSi waveguides with comparable pore sizes.[21] In order to more easily understand the trends presented in **Table 3.3**, we plot the relative change in optical thickness of the different thickness PSi films upon infiltration of the small and large QDs in **Figure 3.8**, which mirrors the trends of the surface density and percent surface area coverage in **Table 3.3**.

Table 3.3 Quantification of small (2.8 nm) and large (7.5 nm) PbS QDs coupled with PSi films of different pore sizes based on estimated refractive index increases of the PSi films.

Average pore size [nm]	Estimated increase in effective refractive index of PSi with QD coupling		Estimated surface density (SD) [m^{-2}] and percent total surface area (% SA) coverage of QDs coupled with PSi			
	Small QDs	Large QDs	Small QDs		Large QDs	
			SD	% SA	SD	% SA
12	0.0260	0.030	1.05E+15	2.05	4.37E+14	2.24
15	0.0425	0.053	1.35E+15	5.35	1.1E+15	3.50
20	0.0460	0.057	2.26E+15	10.68	1.42E+15	7.14
25	0.0470	0.073	2.54E+15	13.40	2.32E+15	11.65
30	0.0340	0.030	1.85E+15	10.72	1.32E+15	5.67

There is a clear dependence of QD binding on PSi pore size, as well as QD size, which suggests that parameters of PSi films for sensing applications must be tuned carefully to enable maximum binding of desired molecules. As shown in **Figure 3.8**, the highest relative increase in optical thickness ($\Delta nL/nL_0$) after QD attachment occurs for PSi with ~25 nm pores, which suggests that the 25 nm pore films will give the largest response for the capture of molecules with sizes ranging from at least 2.8 nm to 7.5 nm. For larger QDs, we expect the peak value of $\Delta nL/nL_0$ to occur for samples with larger pores.

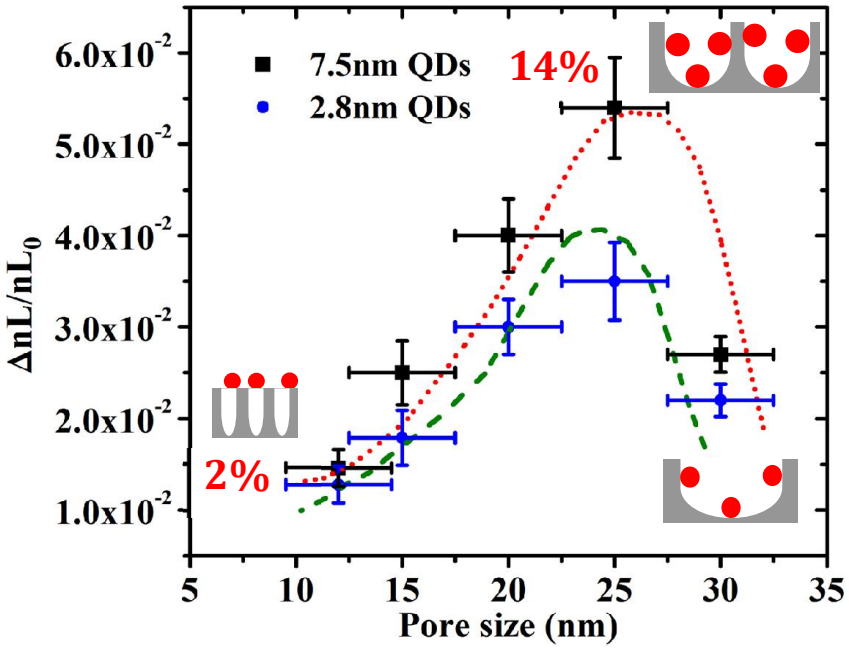

Figure 3.8. Relative increase in optical thickness of ~5.5 μm PSi layers with varying average pore size after immobilizing two different sized QDs (2.8 nm and 7.5 nm). Each data point represents the average value based on three sets of experiments and the dotted and dashed lines serve as guides to the eye. The insets give a representative idea of the pore size to target QD size and the surface area coverage estimates are approximately 2% for

the very small pores increasing upto 14% for the most optimum pore size to target QD size ratio.

The shape of the trend lines in **Figure 3.8** suggest that the value of $\Delta nL/nL_0$ for a PSi film initially increases with pore size because the QDs can more easily infiltrate into the pores. Beyond the optimum pore size to QD size ratio, the reduced surface area available for binding events to take place dominates the ease of infiltration of QDs, fewer QDs bind within the porous matrix, and the effective refractive index increase for the films is reduced thereby resulting in a decrease in the value of $\Delta nL/nL_0$. Despite the slightly lower surface area coverage of the 7.5 nm QDs as compared to the 2.8 nm QDs, the increase in effective refractive index and the values of $\Delta nL/nL_0$ are greater than that achieved with coupling smaller QDs to PSi due to their larger diameter, which results in a significantly higher increase in the net refractive index change upon coupling with PSi. We note that for the PSi sample with an average pore size of ~12 nm, the small increase in optical thickness due to the large QDs can be entirely attributed to the infiltration and coupling of these QDs with pore sizes exceeding ~20 nm, which comprise ~25% of the available surface area in the PSi sample (**Chapter 2 Figure 2.2**). The morphology of the pores also appear to play an important role in this size relationship. Based on cross-sectional SEM analysis of the pore structure formed at different etching current densities (not shown), for etching current densities greater than 20 mA cm^{-2}, the rough dendritic structure of the pores changes to a smoother more cylindrical shape, aiding the infiltration of species into the nanoporous layer and thereby improving the signal response observed for QD attachment.

Overall, the results shown in **Figure 3.8** suggest that pores need to be at least three times larger than the size of nominally spherical target species to allow for diffusion and coupling within the nanoporous framework.

3.5.1.4 Photoluminescence Characterization of QDs in PSi

In addition to the increase in effective refractive index of the PSi layer and measurable shift in the reflectance spectra upon QD attachment in the pores, observation of QD fluorescence modulated by the PSi film serves as a secondary small molecule detection mode confirming QD infiltration and coupling with PSi. **Figure 3.9** shows the measured fluorescence and overlaid reflectance spectra after coupling small and large QDs with PSi films having ~25 nm pores and **Figure 3.10** shows the absorbance and PL of both of QDs in solution. A Coherent Innova 70C water-cooled argon–krypton laser operating at a wavelength of 488 nm and ~10 mW cm-2 optical power was used to excite fluorescence from PSi samples over a spot size of 0.8 cm2. The beam was chopped at 40 Hz by a Stanford Research Systems model SR540 chopper controller. A thermoelectrically cooled InGaAs Oriel detector (model 71646) and a Stanford Research Systems model SR830 lock-in amplifier were used to measure the fluorescence intensity at the output port of a 74100 Oriel Cornerstone 260 ¼ m monochromator over a wavelength range of 800 nm - 1650 nm through a 2 x 7 mm^2 slit.

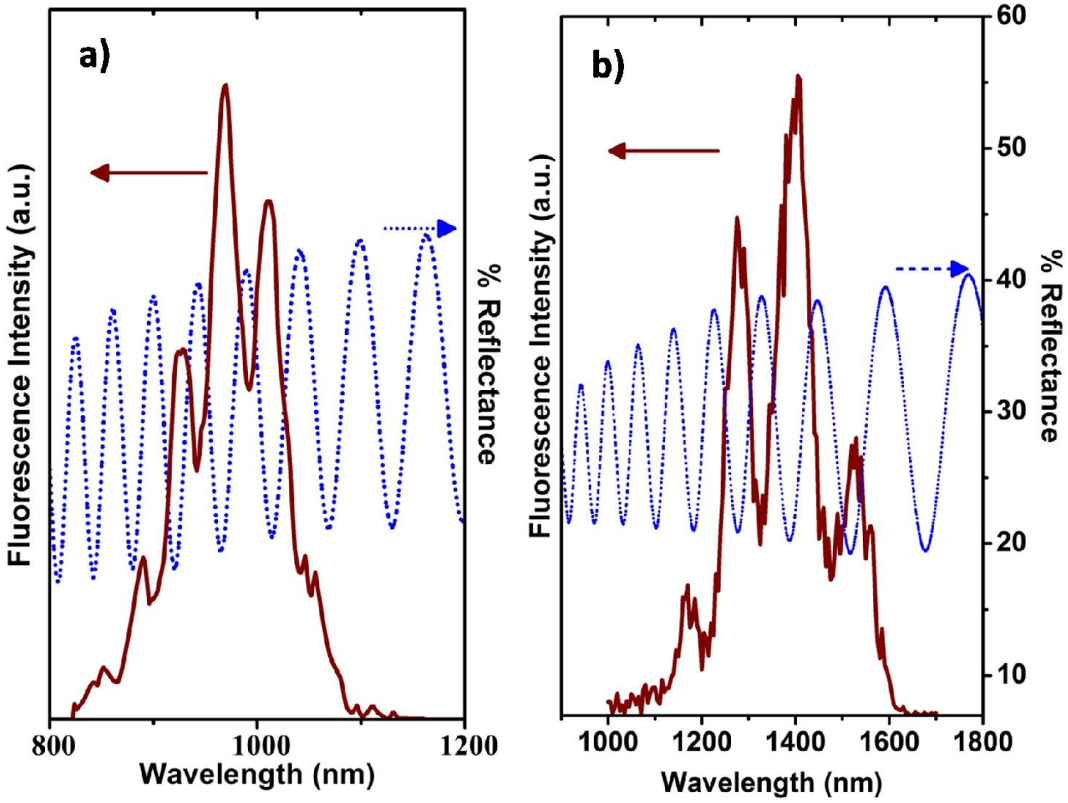

Figure 3.9. QD fluorescence spectra from PSi films (5.5 μm thick, 25 nm average pore diameter) infiltrated with (a) small (2.8 nm) QDs or (b) large (7.5 nm) QDs. The QD emission occurs in the expected wavelength regions based on the size of the QD. The modulated fluorescence (solid line) is due to thin film interference phenomena that also appear in the overlayed reflectance spectra (dotted line).

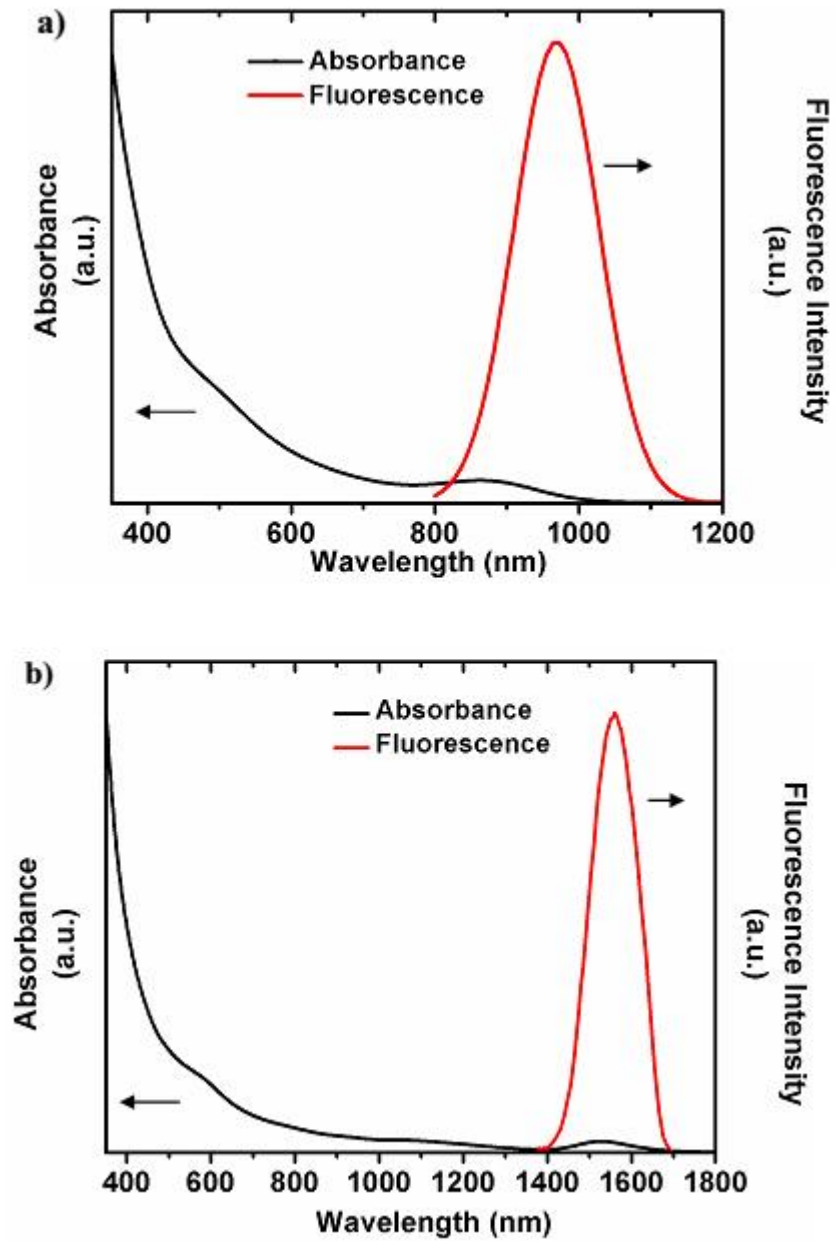

Figure 3.10. PbS QD absorption and fluorescence spectra for a) small 2.8 nm QDs and b) large 7.5 nm QDs.

The interference pattern seen in the QD fluorescence profile correlates with that arising out of thin-film interference and indicates QD attachment throughout the porous matrix. We note that modulation of the fluorescence would be absent if QDs were attached only to the surface of the PSi film. We further note that dips in the reflectance pattern have a π phase shift with respect to the minima in the fluorescence pattern which is introduced in the reflectivity spectra at the air/PSi interface where $n_{air} < n_{PSi}$. Further confirmation of the approximate effective refractive index n_{eff} of the PSi film after QD immobilization may be done by analyzing the modulated QD PL spectra. **Equation 3.1** related the film thickness L, to the n_{eff} as:

$$L = \frac{1}{2neff}\left(\frac{1}{\lambda_r} - \frac{1}{\lambda_{r+1}}\right)^{-1} \qquad 3.1$$

where, λ_r and λ_{r+1} are the r^{th} and $r+1^{th}$ fringe maxima or minima in the reflectance spectra.

3.5.2 Specific detection of biotin using QD conjugates in PSi films

With the demonstration of effective QD infiltration in PSi and an understanding of the size relationship between QDs and PSi pores presented in **Section 3.5.1**, we now demonstrate the use of non-toxic $AgInS_2$/ZnS (AIS/ZnS) QDs as signal amplifiers in PSi biosensors. The biotin-streptavidin system is chosen for the labeled sensing demonstration due to its very strong noncovalent biological interaction.[66, 69, 107] Biotin molecules (~1nm) are conjugated to water soluble AIS/ZnS QDs (~3 nm diameter) and specifically attached to streptavidin-functionalized PSi films which were found to exhibit excellent stability in aqueous and buffer solutions (**Figure 3.11**).

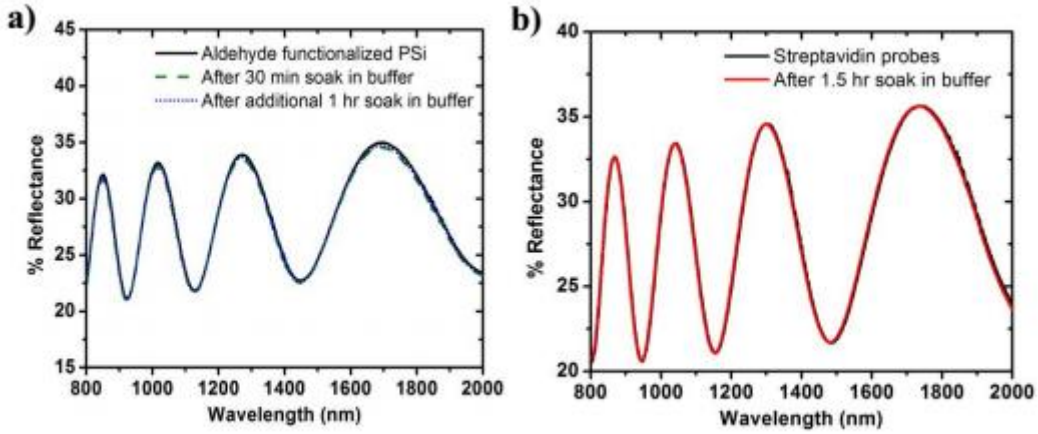

Figure 3.11. Control experiments demonstrating stability of surface functionalized PSi sensor. Reflectance spectra of aldehyde and streptavidin functionalized samples show no measureable shifts following prolonged incubations in buffer solutions.

Optical signal stability of PSi samples functionalized with the following molecules: a) glutaraldehyde, in which reflectance spectra were measured after a 30 min soak in buffer solution and after an additional 1 hr soak in buffer solution, and b) streptavidin probe molecules in which reflectance spectra were measured before and after a 1.5 hr soak in buffer solution. No measureable changes in the reflectance spectra and EOT of the PSi films were observed. After each buffer soak, the samples were rinsed with ethanol, dried under air, and the reflectance spectra were re-measured.

Given the size of the additional linker molecules (~6 nm) necessary for streptavidin-functionalization of the PSi films that reduces the size of the pore opening, PSi films with ~30 nm pores, as-anodized, were utilized, following the analysis presented

in **Section 3.5.1.3.** The estimated decrease in effective pore size following the addition of each linked molecule is shown in **Figure 3.12**.

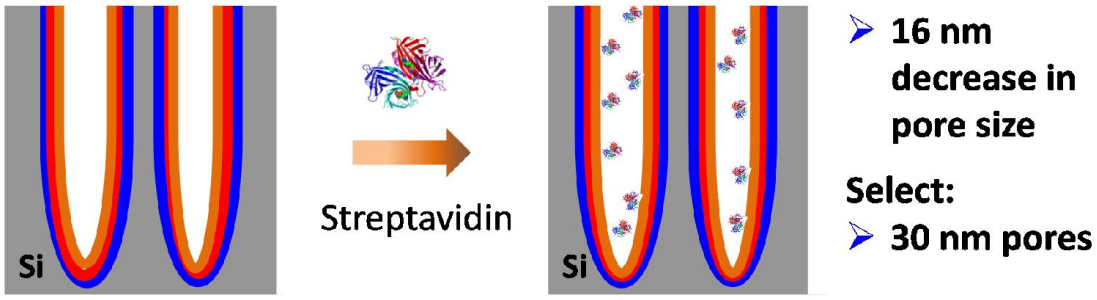

Figure 3.12. Net estimated decrease of 16 nm in average pore sizes after the surface functionalization and streptavidin immobilization steps. Pore sizes of at least 30 nm are expected to allow the infiltration and capture of QD conjugated biotin molecules that are approximately 5 nm in size based on previous data.

Fluorescence and reflectance measurements were performed to demonstrate and quantify the detection of QD-biotin conjugates in PSi. A fiber-coupled Ocean Optics USB4000 CCD spectrometer was used to record visible QD emission between 500 nm and 1000 nm. **Figure 3.13** shows the absorbance and PL of AIS/ZnS QDs in solution.

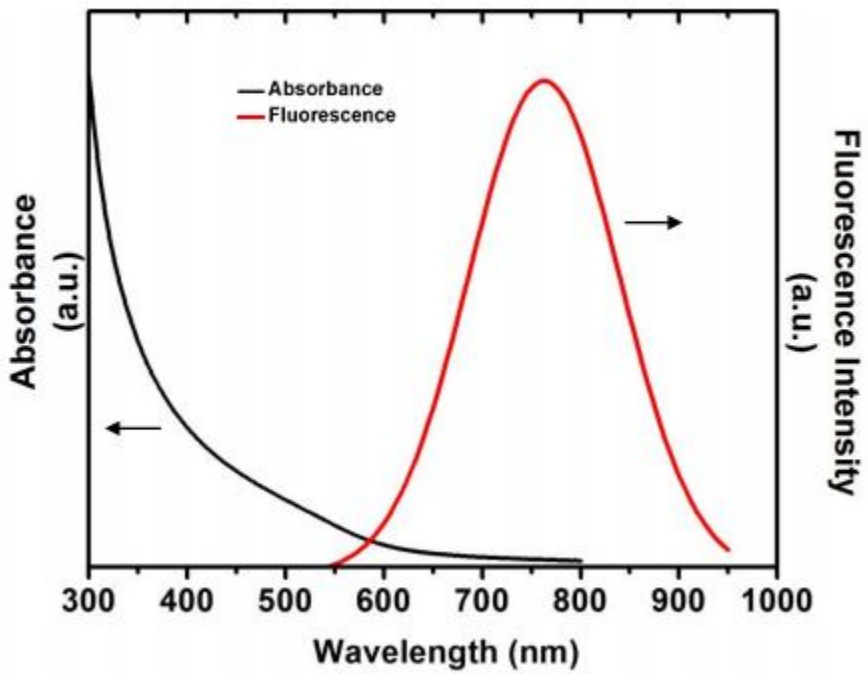

Figure 3.13. AIS/ZnS QD absorbance and fluorescence spectra.

As shown in **Figure 3.14a**, modulated fluorescence is measured when the QD-biotin conjugates are captured in the streptavidin-functionalized PSi. Excellent overlap of the fluorescence spectra from QD-biotin conjugates in solution and when coupled with PSi is also shown, verifying that the modulated fluorescence can indeed be attributed to the AIS/ZnS QDs inside the pores. **Figure 3.14b** shows a reflectance fringe shift of ~27 nm resulting from the attachment of QD-biotin conjugates in PSi. This corresponds to an increase in EOT and effective refractive index of the PSi film of ~110 nm and ~0.025, respectively.

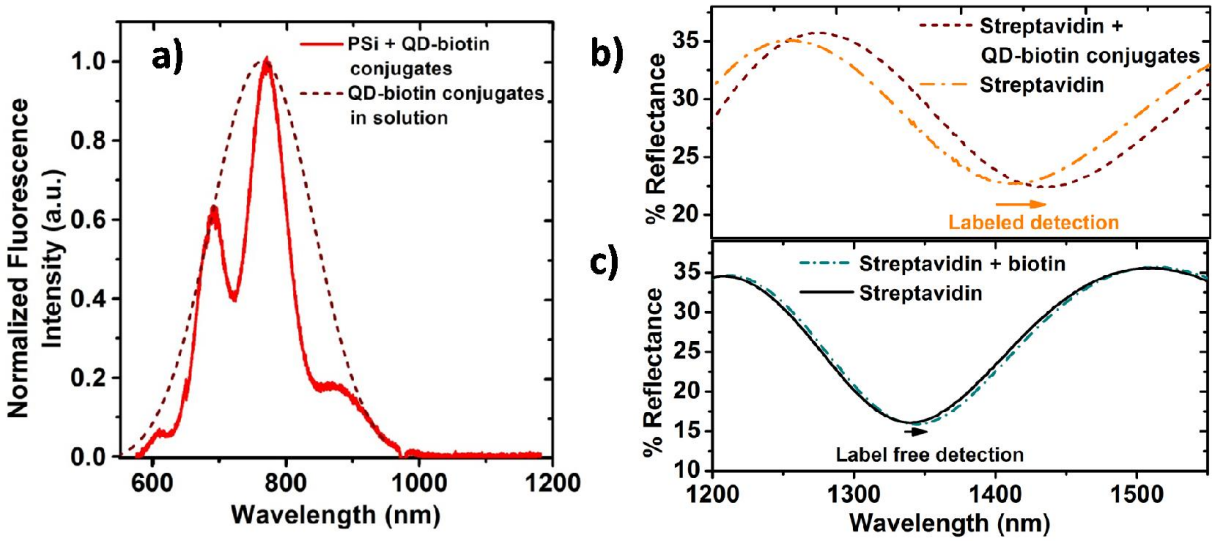

Figure 3.14. (a) Fluorescence spectra of QD-biotin conjugates in solution and bound inside a streptavidin-functionalized PSi film. The fluorescence of the conjugates inside the PSi film is modulated due to thin film interference effects and demonstrates that the conjugates are inside as opposed to only on top of the PSi film. Reflectance spectra for the detection of biotin (b) with and (c) without the use of QD-conjugates from two different PSi samples functionalized with streptavidin probes. Use of the QDs conjugated to biotin molecules significantly amplifies the sensor response.

Control samples in which streptavidin probe molecules were not immobilized did not demonstrate any measurable QD PL (**Figure 3.15**).

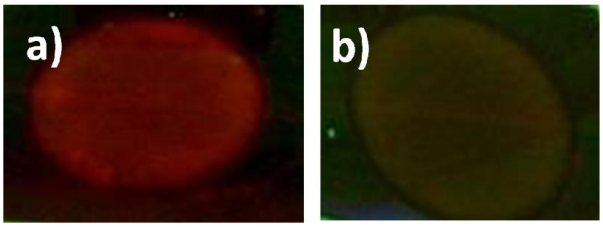

Figure 3.15. Images, under UV excitation at 365 nm, of (a) streptavidin functionalized PSi and (b) a control PSi sample (with no immobilized streptavidin probe molecules) after exposure to a QD-biotin conjugate solution and rinsing of unbound species.

Control experiments monitoring reflectance fringe shifts also did not show any noticeable changes following exposure of samples with no streptavidin probe molecules to QD-biotin conjugates (**Figure 3.16**) or to biotin molecules (**Figure 3.17**), again demonstrating absence of non-specific binding of either QD or biotin molecules to surface functionalized samples in the absence of the streptavidin probe molecules.

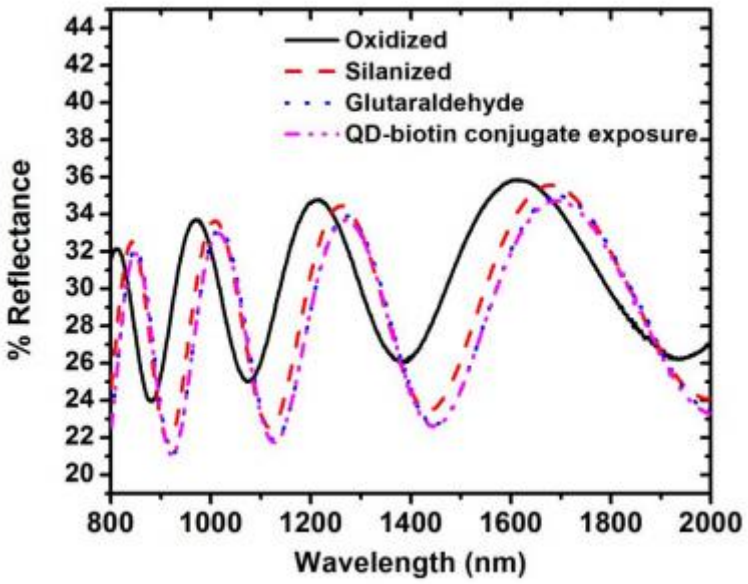

Figure 3.16. Absence of non-specific binding of target QD-biotin conjugates with PSi samples that have no streptavidin probes fixated on the pore walls is clearly demonstrated from reflectance measurements on an oxidized PSi control sample surface functionalized with amine and aldehyde linker molecules but no streptavidin probe molecules after 1 hr exposure to a 500 μM QD-biotin conjugate solution.

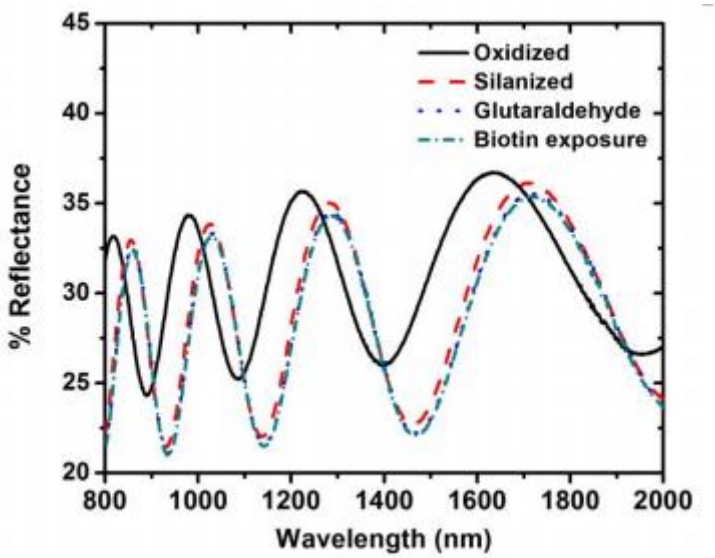

Figure 3.17. Absence of non-specific binding of target biotin molecules with PSi samples that have no streptavidin probes fixated on the pore walls is clearly demonstrated from reflectance measurements on a PSi control sample surface functionalized with amine and aldehyde linker molecules but no streptavidin probe molecules after 1 hr exposure to a 200 μM sulfo-NHS biotin solution.

Using the method presented in **Section 3.5.1.3** and considering the size (~ 4 nm) and refractive index (~ 2.2) of the QD-biotin conjugates, their surface area coverage in the streptavidin-functionalized PSi is estimated to be near 6%, resulting in a surface mass density of ~ 6 fg mm^{-2}. Assuming a conservative minimum resolvable reflectance fringe shift of 0.5 nm, the biotin detection limit of the QD-labeled PSi biosensor is ~ 0.5 fg mm^{-2}. Hence, this sensor achieves improved sensitivity compared to unlabeled optical biosensors.[2]

We experimentally verified and quantified the signal enhancement gained through

the use of the QD labels by attaching unlabeled biotin molecules to streptavidin-functionalized PSi films. As shown in **Figure 3.14c**, a reflectance fringe shift of ~5 nm corresponding to an EOT increase of ~10 nm results from unlabeled biotin attachment, which is in agreement with similar reports for single layer PSi biosensors [113] and is substantially less than that measured for attachment of QD-biotin conjugates. Taking into account the size (~1 nm), refractive index (~1.45) and molecular weight (443.4 g mol^{-1}) for biotin, we calculate a biotin surface mass density of ~7 pg mm^{-2} with a 1:1 binding stoichiometry with streptavidin. For a minimum resolvable fringe shift of 0.5 nm, simulations suggest a detection limit of ~2 pg mm^{-2} for the label-free detection of biotin using PSi. Hence, QD labeling of biotin molecules amplifies the measured change in EOT by one order of magnitude and reduces the detection limit by nearly three orders of magnitude. Moreover, conjugation of biotin with QDs provides a secondary means of target molecule identification based on the distinct QD fluorescence spectrum. Due to the robustness of the PSi sensor substrates, it is also possible to re-use the sensors by removing all organics by immersing the sensors in a Piranha solution for about 1 hr at 60°C.

3.6 Conclusion

Fabrication of a stable, well-characterized dual-mode QD-enhanced PSi biosensor for optical detection of small molecules has been demonstrated. Studies were performed to analyze pore size distributions, determine the available surface area for binding events to take place, and quantify the surface area coverages of QDs on the pore walls for different PSi films. The tradeoffs between ease of molecular infiltration into larger sized pores with

the increase in surface area obtained with smaller sized pores were presented, and a 3:1 ratio of pore:molecule size was determined to be the minimum necessary for infiltration and attachment of spherical infiltrated species. Attachment of target QD-biotin conjugates to streptavidin molecules immobilized in the optimized PSi matrix results in a significant increase in the effective refractive index of the porous layer beyond that of unlabeled biotin immobilization and reduces the detection limit by nearly three orders of magnitude. Biotin identification is also possible by means of the secondary sensing mode whereby the conjugated QDs generate distinct fluorescence. A detection limit below 1 fg mm^{-2} was demonstrated for the labeled detection of biotin molecules using a stable streptavidin-functionalized thin film PSi sensor, which demonstrates a working range of 7 pg mm^{-2} to 0.5 fg mm^{-2}. The approach of using QD-bioconjugates coupled to PSi films opens up possibilities for biocompatible, environmentally friendly, highly sensitive, real-time multiplexed opto-fluidic assays to study binding kinetics of analytes and detect disease markers at ultra-low concentrations without the need for complex and costly lithographic steps.

4. OPTICAL CAVITY ENHANCED LIGHT MATTER INTERACTIONS FOR BIOSENSING

4.1 Introduction

As discussed in **Chapter 1.2.3**, label-free optical sensors such as ring resonators, PhCs, and whispering gallery mode resonators can serve as ultra-sensitive small molecule detection platforms with few of the assay complexities that are often associated with labeled-detection. However, these sensing platforms are limited to research labs and laboratories due to the expensive coupling optics, costly equipment, and complex optical alignment requirements. To achieve point-of-care diagnostics, low cost, portable, smartphone-compatible and straightforward sensor operation is required. To address these needs, improvements in current sensing platforms are required. In this chapter, two approaches towards realizing optical sensor platforms for point-of-care diagnostics will be presented.

4.1.1 PSi Microcavities Integrated with High Contrast Grating Reflectors

One of the difficulties facing PSi membrane microcavity sensors as discussed in **Chapter 1**, is the required infiltration of target analytes through several alternating layers of small and large pore sizes that correspond to high and low refractive index layers respectively. Therefore, although PSi microcavities have been predicted to demonstrate ultra-low sensitivities down to fg[114], the resulting optical structure significantly limits the size and number of linker molecules that may be covalently bound to the active cavity

region and severely limits the choice of target molecules capable of infiltrating and being detected by the PSi microcavity. In order to circumvent this limitation, the idea proposed here is to utilize a sub-wavelength grating reflector that has the potential to entirely replace one of the two Bragg mirror geometries comprising the microcavity sensor design as shown in **Figure 4.1**.

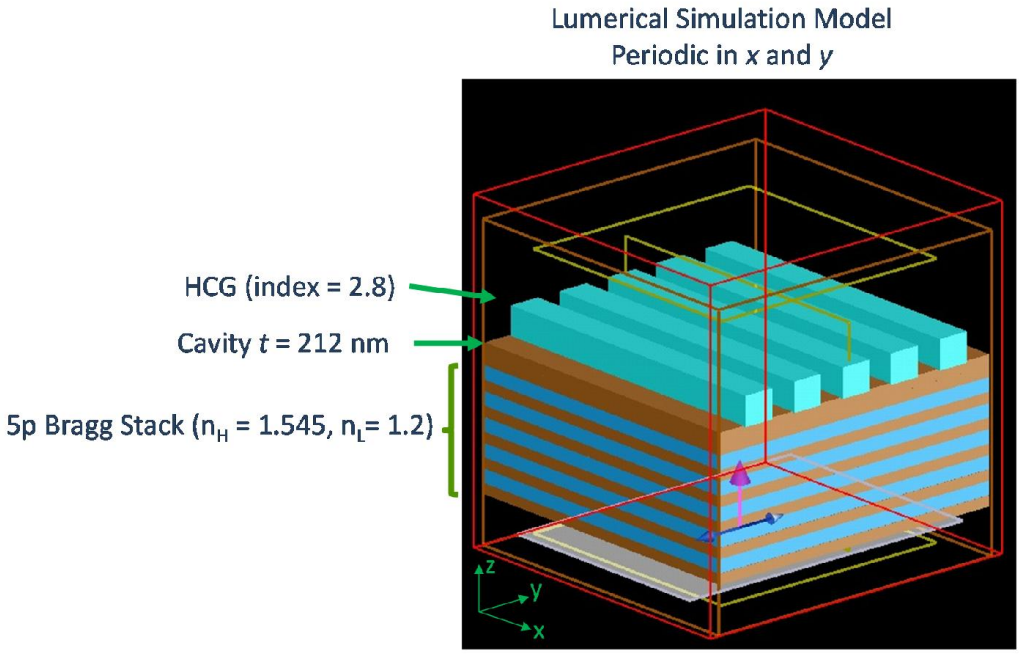

Figure 4.1. Schematic representation of a sub-wavelength high-contrast grating (HCG) reflector integrated with a 212 nm thick, $n_L = 1.2$ cavity layer and a traditional Bragg mirror stack consisting of 5 periods of alternating layers having $n_H = 1.545$ and $n_L = 1.2$ refractive indices. The sensor is designed for a resonance wavelength of 650 nm.

By fabricating a sub-wavelength HCG directly above the cavity layer, it is possible to achieve biomolecule infiltration and detection within the region of high light-matter interaction in the cavity without requiring molecular infiltration through a top Bragg

mirror. The HCG functions as a broadband reflective mirror. Integration of the optical structure on the HCG with microfluidics, can allow for opto-fluidic, real-time detection of analytes within minutes. Additionally, the entire PSi structure can be thermally oxidized, to a $PSiO_2$ structure that minimizes absorption losses for QD emission wavelengths in the visible and provides a chemically stable, inert platform for the development of robust optical boisensors.

4.1.2 PSi-Annular Bragg Resonators

A new class of active, label-free, optical biosensors have emerged, that produce their own narrow spectral emission on resonance.[115-116] Some of the sensors in this class rely on the use of dyes as a laser gain medium while others require complex fabrication techniques to align self-assembled, InGaAs QDs, with the high field regions of 2D PhCs cavity regions.[117]

These optical sensors utilize the advantages of cavity quantum electrodynamics (CQED) to enhance the spontaneous emission rate of emitters coupled to the cavities. According to CQED, the emission rate is not inherit to the emitters themselves. Instead it is controlled by the external electromagnetic environment of the emitter. The coupling strength is maximum when the emitter is located at a point of energy density maxima and when its dipole moment is aligned with the cavity electric field. Therefore, an optical cavity with a high ratio of quality factor to mode volume (Q/V) that exhibits high energy density holds a great advantage in improving lasing performance in active biosensing platforms. The spontaneous emission rate enhancement ($\frac{\Gamma}{\Gamma_0}$) by an external cavity, is represented by the Purcell factor F_p:[118-121]

$$F_p = \frac{\Gamma}{\Gamma_0} = \frac{6Q\left(\frac{\lambda}{2n}\right)^3}{\pi^2} \frac{\varepsilon(\vec{r}_{max})\max[|\vec{E}(\vec{r})|]^2}{\int \varepsilon(\vec{r})|\vec{E}(\vec{r})|^2 d^3r} = \frac{6Q}{\pi^2 V}\left(\frac{\lambda}{2n}\right)^3 \quad \text{.....4.1}$$

where, $\vec{r}_{max}$ is the location of the maximum squared field, n is the index of refraction at the peak field $(\vec{r}_{max})$, $\varepsilon(\vec{r})$ is the position dependent dielectric function, Q is the quality factor of the cavity at resonance, and Γ is derived directly from Fermi's golden rule given by:

$$\Gamma = \frac{2\pi}{\hbar^2}\int_{\infty}^{\infty} \langle|\vec{p}_a \cdot \alpha\vec{E}(\vec{r}_e)|^2\rangle \rho_c(\omega)\rho_e(\omega)d\omega \text{ ... ...4.2}$$

where, $\rho_c(\omega)$ is the density of photon modes in the cavity, $\rho_e(\omega)$ is the mode density for the dipole transition (material emission spectrum), $\vec{p}_a$ is the atomic dipole moment, and $\vec{E}(\vec{r}_e)$ is the electric field at the location of the emitter normalized by a factor $\alpha^2 \equiv \hbar\omega \frac{4\pi}{\int \varepsilon(\vec{r})|\vec{E}(\vec{r})|^2 d^3r}$ to the zero point energy.

Therefore, from **equation 4.**2, there the two ways of increasing the spontaneous emission rate; first one is by increasing the Q and the second one is by increasing the value of the normalized electric field at the emitter $\alpha\vec{E}(\vec{r}_e)$. Increasing the value of the $\alpha\vec{E}(\vec{r}_e)$ achieves the same effect as decreasing the mode volume of the electromagnetic field at the resonance frequency ω_0.

As a result, there are two challenges in practically achieving high Purcell factor cavity designs. The first is to ensure overlap between emitters and regions of highest electric field densities, as the Purcell factor is extremely position dependent. The second

area of improvement lies in the alignment of the emitter dipole moment with the cavity electric field. For traditional 1D, and 2D PhCs, the stop band is due to the confinement between Bragg mirrors or mirror segments and usually works only for a specific polarization and k-vector combination. Therefore, the enhancement of the local density of states in these cavities follows only one polarization direction. On the other hand, emitters such as QDs emit light in all directions with no specific dipole orientation. As a result, most optical cavities like 2D PhCs that are designed as per Cartesian coordinates to enhance a single polarization, are not able to demonstrate equally high Purcell factors for emitters whose dipole moment is not aligned with the cavity electric field resulting in large variabilities in the performance and complexities in the design of CQED experiments dependent upon the positioning and orientation of emitters within the cavity regions that have the highest field enhancements. Recently, a Purcell factor of ~31 has been demonstrated for a dielectric slot waveguide, that has theoretical Purcell factor of 62.[122]

Aimed at addressing these two challenges, in this work, we demonstrate PSi-QD annular Bragg resonators (ABRs) as an active, label-free biosensing platform. ABRs have been demonstrated previously as platforms for achieving narrow line-width lasing mainly for VCSELs (vertical cavity surface emitting lasers) using high index materials such as InGaAsP, polymers, and photoresists such as SU-8.[123-125] Instead of designing a discrete refractive index profile along one or two directions in the Cartesian coordinate system, design of ABRs is based on the discretization of refractive index profile along the radial direction in the polar coordinate system. PSi as a 3D scaffold provides extremely high internal surface areas accessible to the immobilization of light-emitting QDs and target

small molecules. When immobilized within an appropriately designed cavity region of a PSi scaffold, QD emission can be spectrally matched with the cavity resonance wavelength and QD spatial location can co-located with regions of highest field intensity inside the PSi cavity. Consequently, a QD-PSi system can be straightforwardly designed to demonstrate strong, narrow line-width spontaneous emission at the cavity resonance wavelength (**Figure 4.2a**). The QD integrated 3D porous scaffold further allows access of target biomolecules to regions of highest field intensities within the porous cavity region. As a result, any changes in the environmental refractive index of the PSi-QD ABR upon capture of target molecules causes a shift in the resonance wavelength of the ABR sensor and a concurrent shift in the cavity-emitted wavelength of the QD (**Figure 4.2b)**.

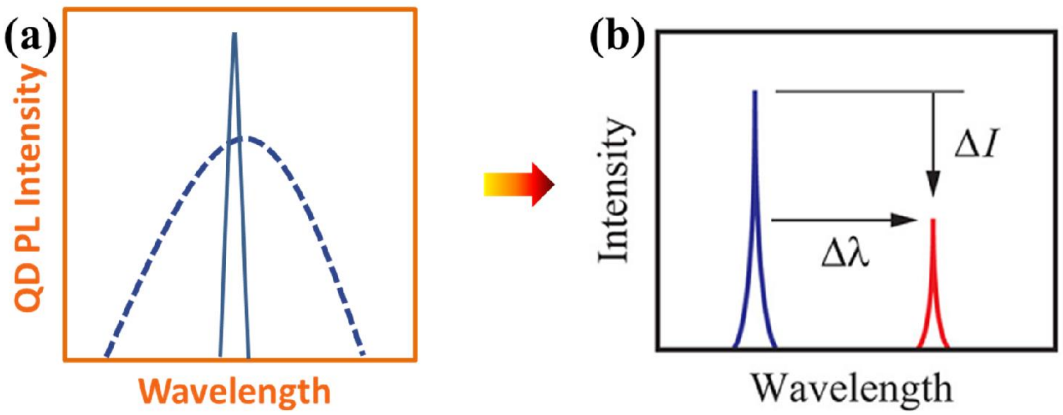

Figure 4.2. Schematic illustration of ABR cavity modified QD PL intensities. a) The broadband QD emission changes to a narrow line-width emission due to CQED. b) Perturbation of the effective refractive index of the PSi-ABR sensor upon capture of target molecules shifts the cavity resonance wavelength due to an increase in the effective refractive index of the ABR and therefore also shifts the narrow line-width QD emission to a longer wavelength. The shift in resonance wavelength may be accompanied by a change in QD emission intensities due to absorption losses upon the addition of biomolecules to the sensor and the respective change in cavity resonance position relative to the peak QD emission wavelength.

4.2 Design and Simulation Results

4.2.1 PSi Microcavities Integrated with High Contrast Grating Reflectors

As discussed earlier in the chapter, a HCG is capable of mirroring the performance of a traditional Bragg layer stack. Initial simulations were performed in Lumerical to confirm this hypothesis by adding a HCG to the top Bragg mirror of a traditional PSi μC design, with the difference being that the number of periods in the top Bragg mirror were reduced from 5 to 3 in order to weaken the traditional top Bragg mirror effect in the μC

structure (**Figure 4.3**). In addition, as introduced in Chapter 1, a low index spacer region was added directly below the HCG to ensure the high reflectivity operation over a wide bandwidth. In **Figure 4.3**, this spacer region is designated as *cavity*$_2$. Optimizations of the HCG design were then carried out to maximize the μC Q-factor and electric-field intensities within the cavity region.

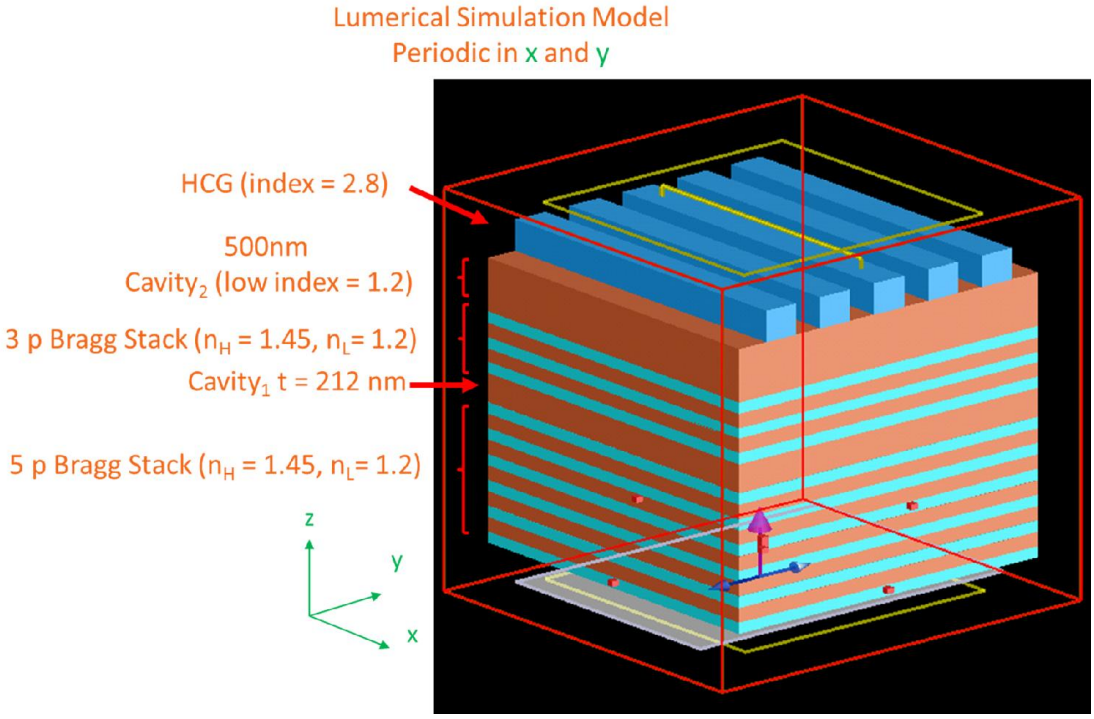

Figure 4.3. Schematic representation of a PSi μC integrated with a HCG. A broadband source polarized perpendicular to the grating lines is incident vertically in z_+ direction from below. A monitor placed below the resonator records transmission spectra in reflectance mode. Another monitor placed above the resonator records transmission spectra through the μC-HCG. Field distributions are recorded by a monitor in the *x*-*z* plane at *y*=0.

The refractive indices for the alternating PSi layers comprising the Bragg stack are chosen based on those that are practically feasible for fabrication, providing the largest refractive index contrast possible, while ensuring the lower porosity cavity region (60% porosity)

consists of pore sizes of at least 20 nm on average, prior to oxidation, to allow for infiltration of target molecules into the regions of highest field confinements. The refractive index of the grating lines is chosen to be 2.8 taking into consideration a moderately high refractive index that provides a choice of materials such as silicon nitride for experimental realization.

Simulation results for the resulting PSi μC-HCG design, for changes in grating height, are as shown in **Figure 4.4**. The simulation results are for light polarized perpendicular to the grating lines. The higher the refractive index contrast of the grating, the greater will be the reflection bandwidth of the HCG. A grating period of 450 nm has been chosen based on the required reflectance over the visible wavelengths of approximately 500 nm to 700 nm as discussed in **Section 4.1.1**. The reflectance band shifts to longer wavelengths for increasing grating periods.

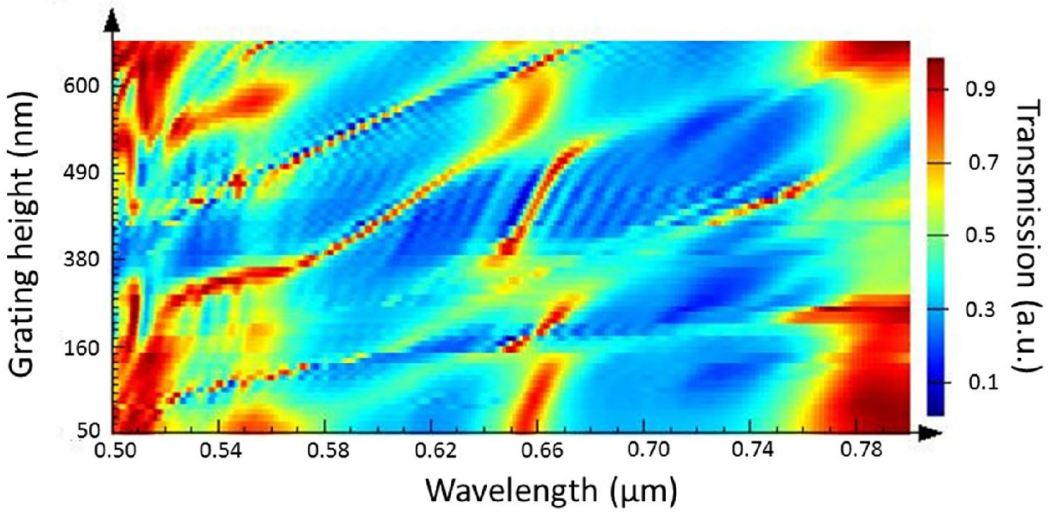

Figure 4.4. Simulation results for the transmission spectra in reflectance mode at a monitor placed below the μC-HCG for changes in the HCG height.

For thin gratings, the HCG demonstrates overall reduced reflectivities. This results in a broader resonance centered near the 650 nm of the μC and no resonances for the cavity layer directly below the HCG. As the grating height increases to above 300 nm, sharper spectral lines in the transmission spectra of **Figure 4.4** are noticeable near the 600 nm wavelength. Increase in grating heights beyond 500 nm show disappearances of the narrow linewidth resonances for $cavity_1$ and $cavity_2$. For optimizations of grating width, a grating height of 390 nm has been chosen based on the results as shown in **Figure 4.4**.

Simulation results for a PSi μC-HCG for changes in grating width are shown in **Figure 4.5**. Changes in the grating width are seen to affect the two resonance positions near 600 nm and near 700 nm. Increasing the grating width is seen to shift these two resonances further apart (**Figure 4.5a**). **Figure 4.5b** shows the simulated transmission spectra through the μC-HCG structure. Due to the broadband, high reflectivity of the HCG, transmission between 550 nm and 750 nm is really low.

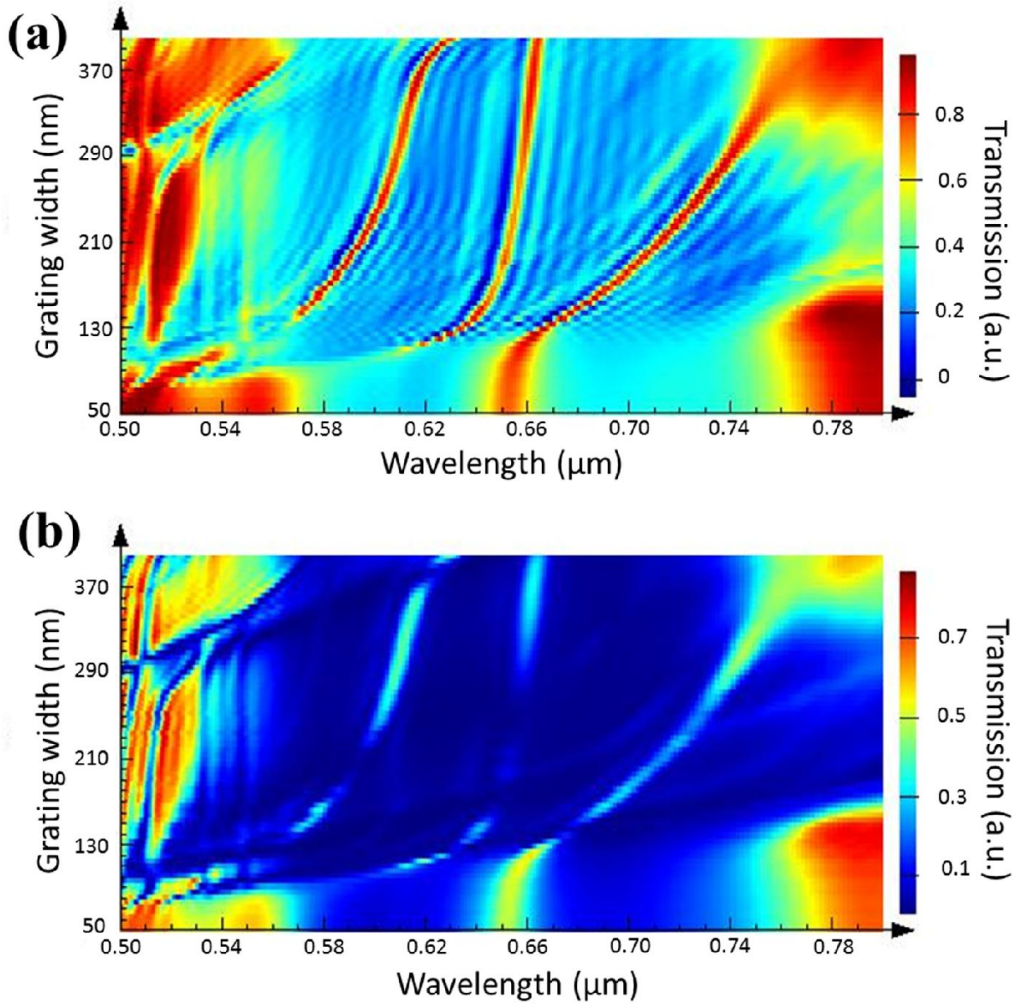

Figure 4.5. Simulation results for a) the reflectance spectra for the PSi μC-HCG calculated as (1 – transmission) b) transmission spectra at a monitor placed above the HCG as a function of the HCG width.

By selecting the most optimum HCG height and width of 390 nm and 290 nm, simulation results for the reflection and E-field magnitude in the structure are shown in **Figure 4.6**. The two cavities are seen to support resonances at two different wavelengths

of 600 nm and 650 nm corresponding to the two different cavity widths. The position of the two resonances may be tuned by changing the cavity width.

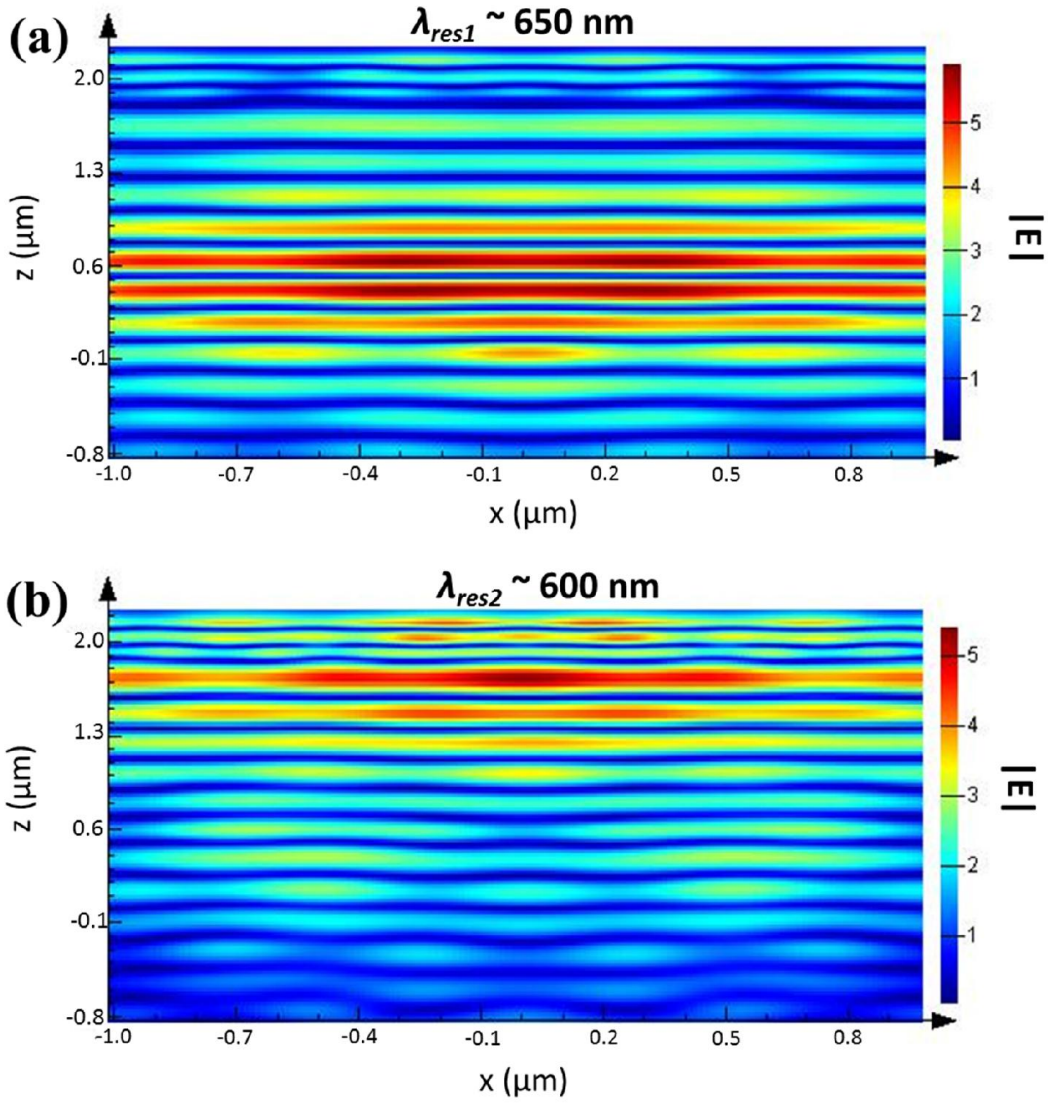

Figure 4.6. Plot of electric-field distribution within the PSi μC-HCG structure in the *x-z* plane (y = 0) at the two resonance wavelengths: a) $cavity_1$ resonance wavelength of ~650 nm and b) $cavity_2$ resonance wavelength of ~600 nm.

The corresponding transmission spectra in reflectance mode for the PSi μC-HCG sensor is shown in **Figure 4.7** along with estimated *Q* factors of 290 and 180 for the two resonances.

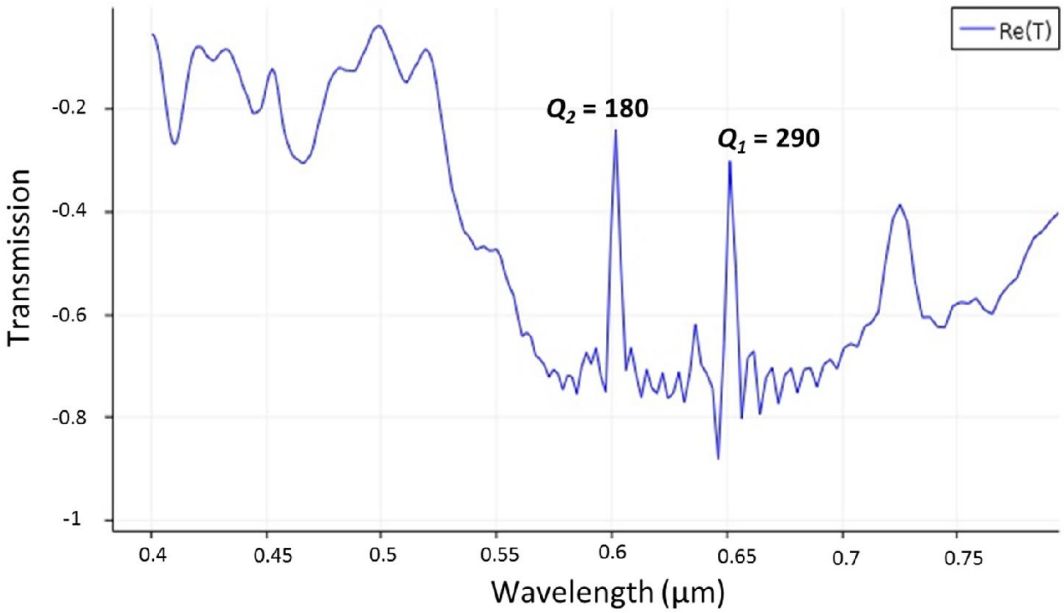

Figure 4.7. Plot of simulated reflectance for the PSi μC-HCG resonator calculated as (1 – transmission). Q factors corresponding to the two cavity resonance wavelengths at 600 nm and 650 nm have been indicated.

In order to verify the importance of the broadband reflectance of the HCG when integrated with the PSi μC structure, simulations were performed for the exact same PSi μC structure except for the HCG. **Figure 4.8** shows the electric field profile and transmission for the traditional μC structure. The field confinement is noticeably weaker and the Q factor is very low. This result is as expected for a PSi μC designed with very few Bragg periods on either side of the cavity.

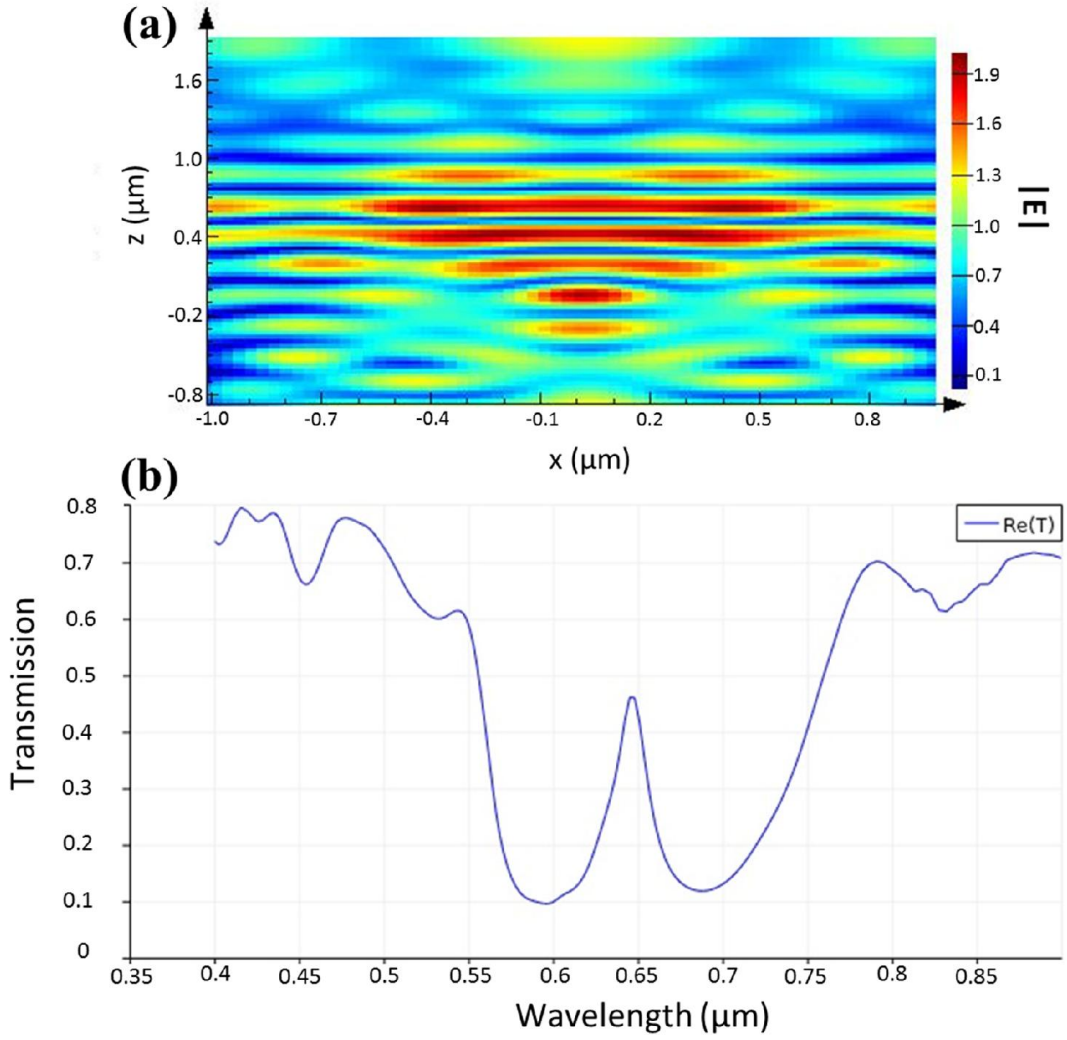

Figure 4.8. Plot of electric-field distribution within the μC structure in the *x*-*z* plane (*y* = 0) at the resonance wavelength of 650 nm. b) Plot of μC transmission showing a very weak resonance near 650 nm.

While the earlier design may allow for size selective detection of small and large biomolecules due to the two cavity regions with different molecular accessibilities, the infiltration challenges associated with complex assays make the traditional μC region highly inaccessible. Therefore, an approach that utilizes just the cavity region below the

HCG is most suitable for the development of robust, point-of-care diagnostic platforms. Simulations were carried out for a PSi-HCG μC that utilized a single Bragg stack at one end and a HCG at the other end of a cavity region. **Figure 4.9** shows the electric field profile and transmission in reflectance mode for the PSi μC-HCG resonator.

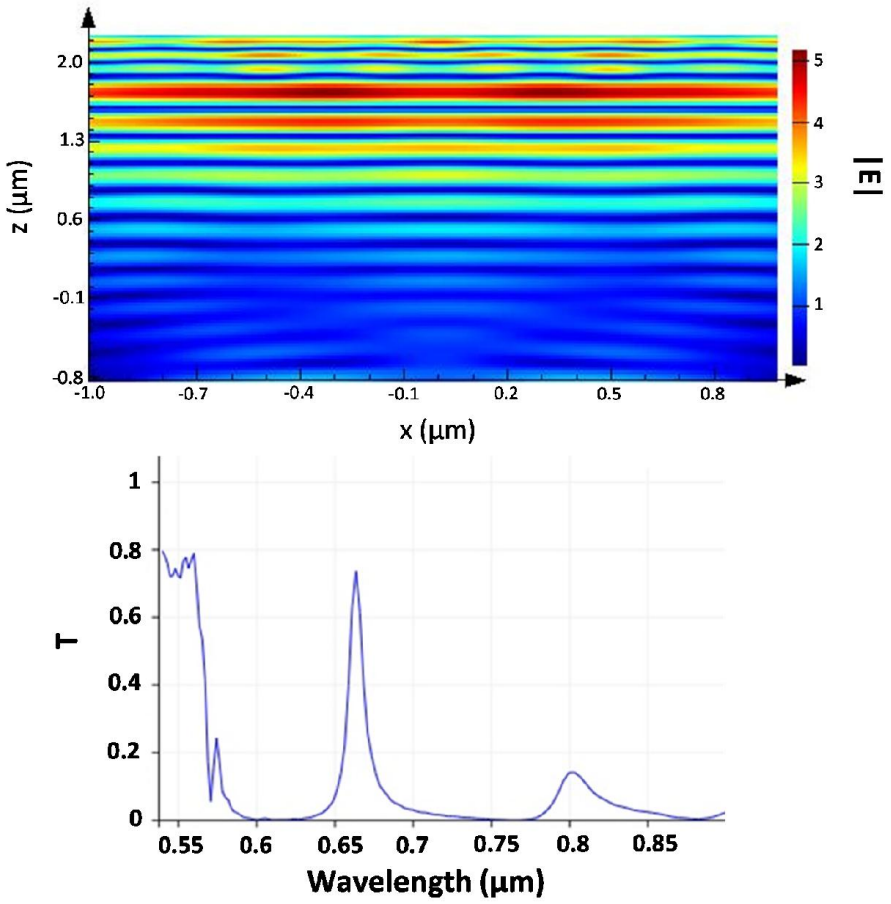

Figure 4.9. a) Plot of E-field distribution at the resonance wavelength of 620 nm, within the μC structure in the *x*-*z* plane, $y = 0$. b) Plot of transmission for the μC-HCG showing a resonance near 620 nm with a *Q* factor over 130.

Sensitivity analysis: At a resonance wavelength of ~ 650 nm, a Δn increase of 0.01 results in a resonance wavelength shift ($\Delta\lambda$) of 2.68 nm for a PSi-HCG $PSiO_2$ cavity thickness of ~ 200 nm. The $\Delta\lambda/L$ which is proportional to $\Delta\lambda/g$, where g denotes the unit mass of analyte required translates to a value given by ~2.68/200 = 0.0134. In comparison, the PSi thin-film biosensor results in a $\Delta\lambda$ of ~6 nm, in reflectance fringe shift, for a minimum required $PSiO_2$ thickness of ~3500 nm. However, taking into consideration the much larger film thickness required to achieve detectable phase difference, in a single layer configuration, the $\Delta\lambda/L \equiv \Delta\lambda/g$, translates to 6/3500 = 0.00171. The PSi-HCG μC results in > 7 fold improvement in wavelength shift/unit mass of analyte required, and has the potential to push detection limits of PSi based optical sensors to the sub-nM regime.

4.2.2 PSi-ABR Sensors

Extending the concept of enhancing light-matter interactions in PSi based resonators, the ABRs design is based on the traditional quarter wave stack Bragg mirror, surrounding a central cavity region. Each layer comprising the Bragg stack is equivalent to an optical thickness of $\lambda/4$, where λ is the central Bragg mirror wavelength. Unlike the PSi microcavity with the high contrast grating reflector that employs a linear Bragg mirror design, the Bragg mirror for the ABR is positioned radially around the cavity region. For alternating Bragg layers with 10 periods of n_{PSi}=1.75 and n_{air}= 1, 3D FDTD simulations in Lumerical using a course mesh size of 3 show electric-field enhancements of 70 for a central disk radius of ~225 nm (**Figure 4.10)**. These electric-field enhancements are comparable to those reported by Liu et. al[126] with the addition of a cladding layer of high porosity PSi that is expected to reduce the refractive index contrast at the substrate interface. The selected value for the PSi refractive index is based on estimations discussed

in **Chapter 3** for a 60% porosity sample with ~20 nm pore diameters that was etched at 20 mA/cm^2 and then subjected to an 800 °C, 30 min thermal oxidation. The course mesh simulation in Lumerical is expected to underestimate the field enhancements due to increased scattering losses associated with increased surface roughness that is generated at reduced mesh sizes.

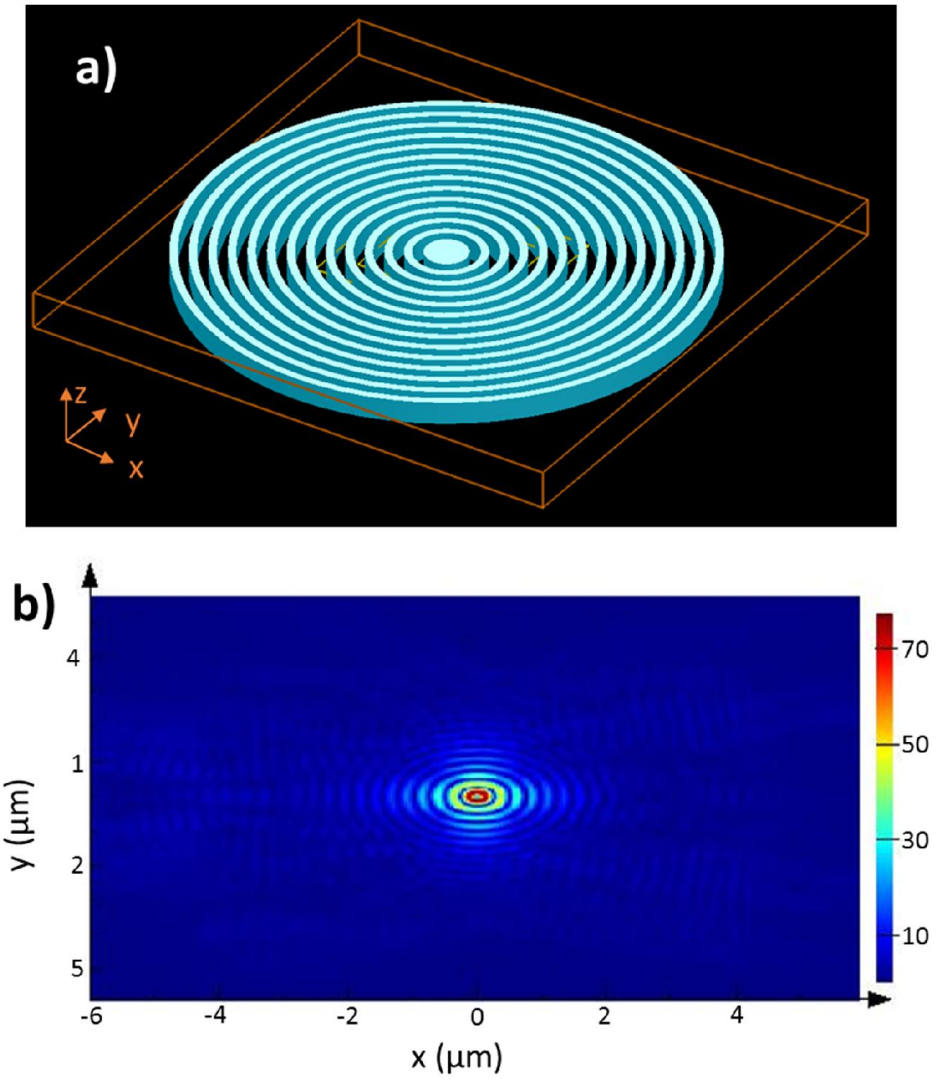

Figure 4.10. a) 3D FDTD model for a 10 period radial Bragg stack surrounding the central cavity region, 225 nm, of the ABR in Lumerical. b) 3D FDTD plot of the electric-field magnitude on resonance for the ABR. The color bar represents the amplitude of the electric-field at the z = 0 cross-section.

Increasing the Bragg stack from 10 periods to 14 periods increases the electric-field enhancement to 140 at the resonance wavelength of 645 nm with a Purcell factor enhancement of ~20 (**Figure 4.11**). As per previous research, the effects of field enhancement start to taper off for Bragg stacks exceeding 15 periods due to decreasing field intensities present moving further from the central cavity region.[39, 126]

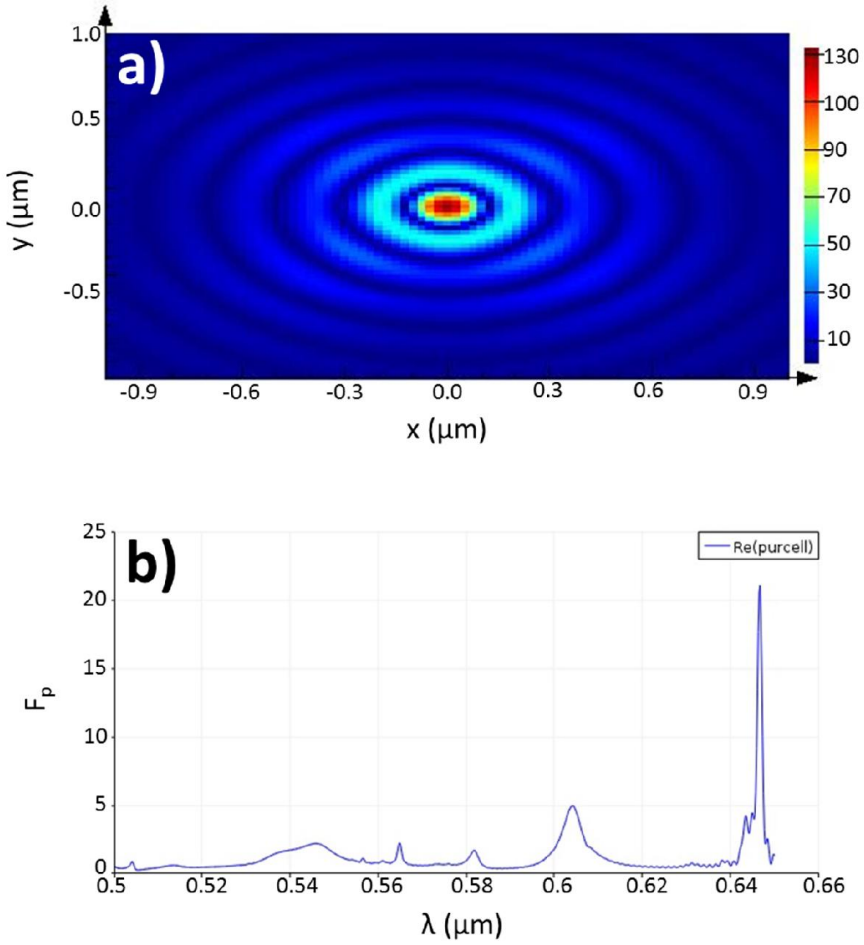

Figure 4.11. a) 3D FDTD plot of the electric-field magnitude on resonance for a 14 period radial Bragg stack surrounding the central cavity region of the ABR described in Fig. 4.10. b) Estimated Purcell factor at the designed resonance wavelength of ~645 nm. The color bar represents the amplitude of the electric-field at the z = 0 cross-section.

4.2.2.1 Q-factor optimizations

Circular Bragg mirrors enable the modulation of the refractive index along polar coordinates. As a result, the cylindrical coordinate system is a mathematically more accurate form of representation than the Cartesian coordinate system. In the cylindrical

coordinate system, only one degree of freedom, radius (r), may be varied instead of two (x and y coordinates), for the Cartesian coordinates. This significantly improves calculation efficiency in FDTD simulations, as the structure dimension can be reduced by radical symmetry in cylindrical coordinates. The following optimizations are all based on cylindrical coordinates.

In a microcavity formed by traditional quarter wavelength Bragg mirror stacks in one direction, the modes with k vector along the direction of refractive index modulation have discrete optical frequencies, and are usually well confined by the optical band gap. Therefore, traditional microcavities are only able to confine one polarization of incident light for a given wavelength. For the case of the ABRs, the refractive index modulation occurs along the radial wavevectors, and the resulting optical band gap provides complete in-plane optical confinement. The improved 2D mode confinement, results in Purcell factor enhancements for more than one polarization direction which is a significant advantage for enhancing the emission of emitters such as colloidal QDs. Improvements in ABR resonance rely on matching the central Bragg mirror wavelength with the supported resonance wavelength mode number for the central disk.

Therefore, further optimizations of the ABR are possible by varying the central disk radius, and duty cycle of the radial Bragg mirrors. **Figures 4.12a,b** show variations in the Q-factor for the ABRs on resonance at 669 nm as (i) the central disk radius is swept while keeping the duty cycle constant and (ii) the duty cycle is varied while choosing a central disk radius of 210 nm which provided the highest Q-factor from (i). As shown in the **Figure 4.12a**, the Q factor significantly increases at R_0=210 nm as the WGMs enters the band gap

of the confining annular Bragg mirrors. After selecting an optimized central disk radius of $R_0 = 210$ nm, the next step is to fine tune the confinement of the surrounding annular Bragg mirrors. Generally speaking, the confinement is best when the resonance frequency is at the mid-gap of the stop band and the electric field on resonance is allowed to exponentially decay away from the cavity. **Figure 4.12b** clearly shows that when the duty circle is tuned to 0.44, the Q factor is highest (~10^5). The index profile of the complete ABR structure including the supporting cladding layer, and the corresponding magnetic field (H-field) profile are shown in **Figure 4.12c**. The z cross-sectional cut of the PSi-ABR provides the out-of-plane H-field distribution while the E-field is in plane. Due to the radial symmetry in polar coordinates that allows for faster simulation time in MEEP, the output results contain field information for the out-of-plane components. The localization of the H-field in the central disk is indicative of the mode confinement as designed at a resonance wavelength of 669 nm.

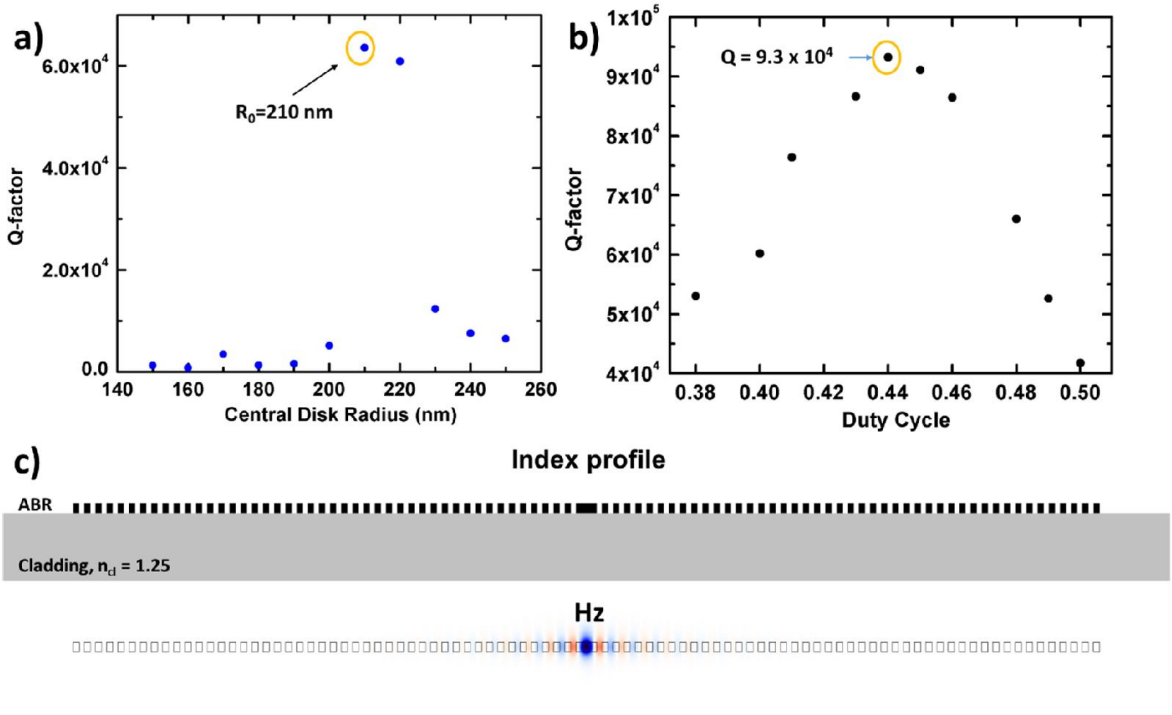

Figure. 4.12. 3D simulations of PSi-ABR in MEEP. a) Optimization of Q-factor based on sweeps of the central disk radius. b) Optimizations of Q-factor based on sweeps of the duty cycle. c) Index profile of the ABR structure with a cladding layer of n = 1.25.

4.2.2.2 Sub-wavelength cavity optimizations

Geometries known as "slots", which exploit the discontinuity of the electric field at an interface, have emerged as a means of squeezing the mode volume down to sub-wavelength regions and increasing the electric field intensity in those regions, thereby increasing the sensitivity of photonic devices incorporating slots to the capture of small molecules that overlap with the extremely localized, high field intensities.[34, 114, 127]

As per the electromagnetic boundary conditions, the normal component of the electric displacement field (D_n) is continuous across an interface (**Equation 4.1**).

Accordingly, the corresponding E-field intensity (**Equation 4.2**) undergoes an abrupt change at the interface between two media wherein the E-field intensity in the low index or "slot" region, experiences an increase proportional to the ratio of the dielectric constants of the two media given by **Equation 4.3**.[128]

$$D_{n,low} = D_{n,high} \quad \text{.....4.1}$$

$$\varepsilon_{low} E_{low} = \varepsilon_{high} E_{high} \quad \text{.....4.2}$$

$$E_{low} = E_{slot} = \frac{\varepsilon_{high} E_{high}}{\varepsilon_{low}} \quad \text{.....4.3}$$

The Purcell factor, which is inversely proportional to the cavity mode volume, naturally increases for slotted cavity structures. For applications pertaining to integration with quantum dots that serve as built-in light emitters, improvements in the Purcell factor will drive increases in the spontaneous emission rates of colloidal QDs whose dipole moments are aligned with the cavity electric field polarization.[129]

Figure 4.13 shows the schematic representations of a slotted PSi-ABR in Lumerical.

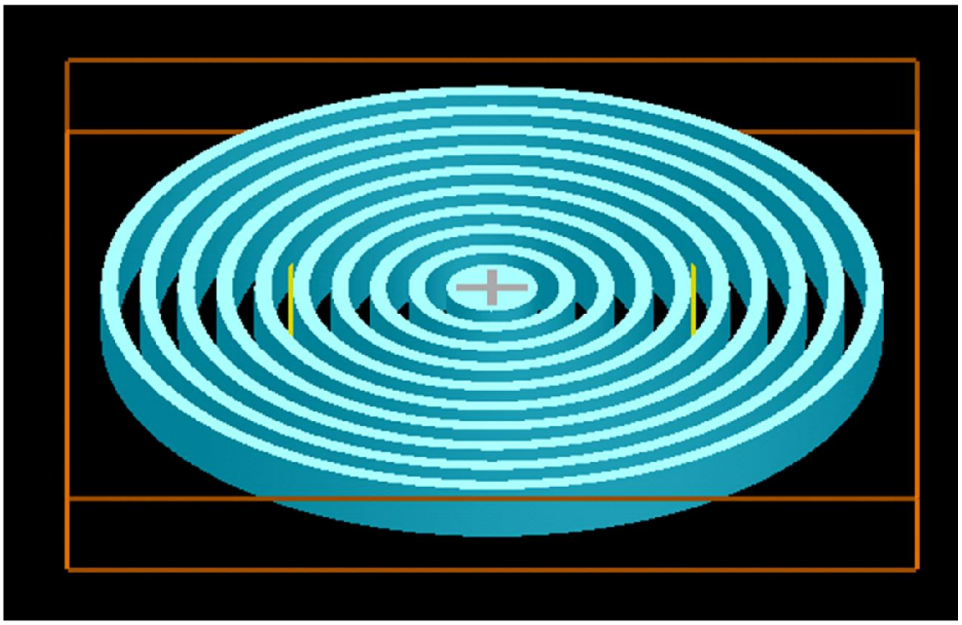

b)

Figure 4.13. 3D FDTD model for the PSi-ABR with slotted cavity region.

Figure 4.14 shows 3D FDTD simulation results for the 14 period ABR design shown previously in **Figure 4.12**, but with the addition of two intersecting slots within the central disk.

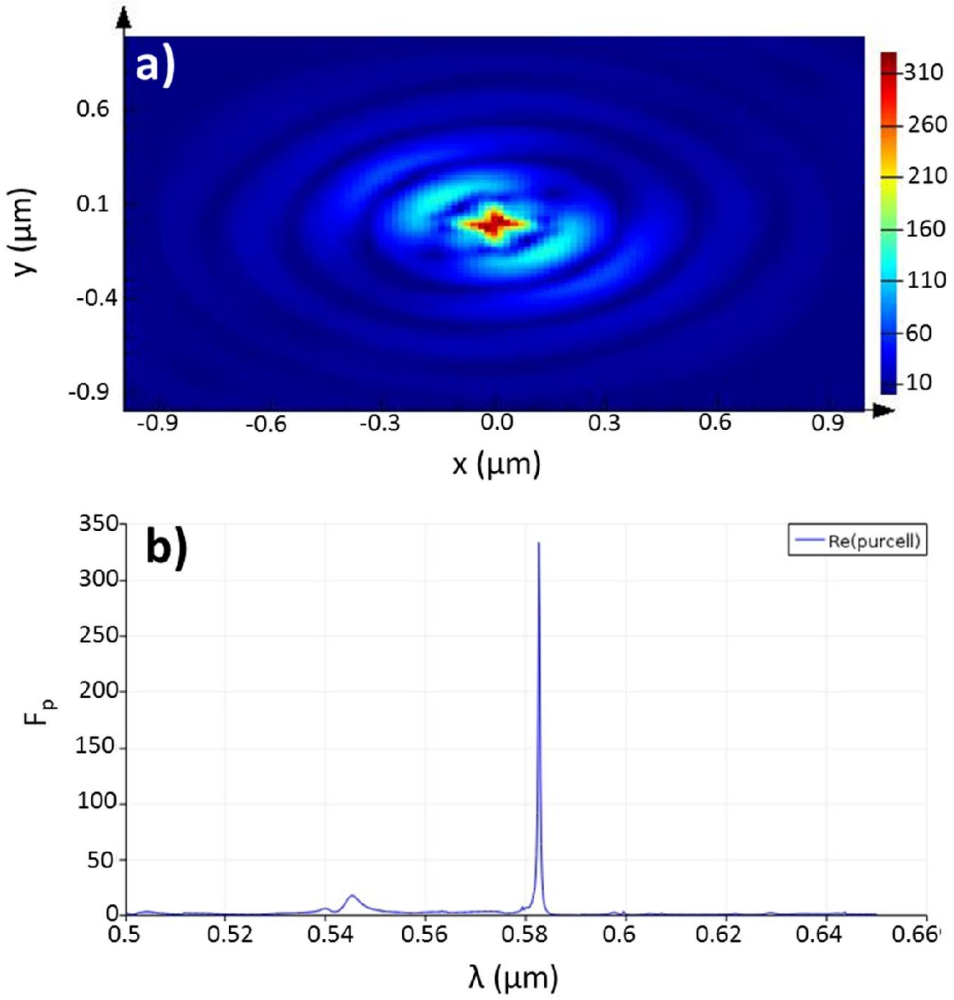

Figure 4.14. a) 3D FDTD plot of the E-field magnitude on resonance, for a 14 period radial Bragg stack surrounding the central "slotted" cavity region of the ABR. The color bar represents the amplitude of the E-field at the z = 0 cross-section. b) Estimated Purcell factor over the wavelength range of interest with the highest value near 350 corresponding to the resonance wavelength of ~581 nm.

The dimensions of the intersecting slots are 350 nm x 70 nm. Parameter sweep simulations varying the slot lengths from 100 nm to 450 nm in steps of 50 nm, while varying the slot

width from 50 nm upto 150 nm in steps of 10 nm, found a slot length of 350 nm and slot width of 70 nm to provide the maximum E-field enhancement. With the additional "slots", E-field enhancements of ~310 and Purcell factor estimations of ~350 have been simulated. These results represent nearly an order of magnitude improvement in the E-fields and Purcell factors of PSi-ABRs with the addition of sub-wavelength slots. In comparison, metal-insulator-metal plasmonic resonators have demonstrated Purcell factors close to 900.[130] However, although these resonators may increase the spontaneous emission rate of coupled QD emitters for one specific dipole orientation, they exhibit very low Q values close to 16 making them very poor refractive index based optical sensors and the complexities associated with orienting the dipole moment of the emitter with the plasmonic cavity field is another significant hurdle in the practical implementation these resonators.

4.3 Conclusion

The PSi-QD HCG-μC and ABR have the capability of delivering a low-cost, portable, smart-phone compatible, and highly sensitive sensing platform. The HCG-μC has been demonstrated to overcome the limitations facing traditional PSi μC designs while offering an over 5 fold improvement in detection limit sensitivities in comparison to a single layer PSi thin-film biosensor.

For QDs immobilized within ABRs, the in-plane field confinement offers improved overall Purcell enhancements when compared with linear PhC cavities that achieve either TM or TE mode confinement at a particular resonance wavelength. Therefore, by carefully engineering both material and device design, we are able to address the two challenges faced by traditional optical dielectric cavities and design an optimal active optical

biosensor platform. The incorporation of intersecting “slots” within the cavity center has the potential to significantly increase the Purcell factors, enhance target molecule overlap with regions of highest field intensities, and drive improvements in the performance metrics of QD integrated ABR sensors. Additionally, the minimal refractive index contrast required for designing the ABR implies that easy-to-fabricate materials such as polymers may also be used with no loss of performance.

Further optimizations of the designs are expected to improve Q factor and detection sensitivities. Together, both sensor platforms are capable of enabling proactive patient self-monitoring, and paving the way towards preventative healthcare through the use of point-of-care diagnostic systems.

5. INTERFACIAL EFFECTS ON THE OPTICAL PROPERTIES OF MONOLAYER QUANTUM DOTS IN POROUS SILICON

5.1 Introduction

Colloidal quantum dots (QDs) possess a number of positive attributes, including a wide range of absorption and emission wavelengths, fast response times, and high rates of radiative emission. These attributes have made them attractive for use as energy emitters or absorbers in applications including LEDs[131-135], lasers[136-137], solar cells[48, 138-143] and radiation scintillators.[144-145] For many of these applications, it is necessary for the QDs to maintain their optical properties when integrated with various materials and interfaces. Consequently, engineering non-radiative recombination rates to either suppress charge transfer and accelerate radiative emissions or enhance charge transfer to an interfacial material is of great interest.[146-147] Most studies to date investigate QD exciton interactions in multi-layer QD thin-films sandwiched between dielectric materials such as TiO_2 for energy conversion applications and a few studies have reported on distance dependent non-radiative energy transfer from CdSe/ZnS QDs deposited on planar silicon substrates.[47, 148-150] However, although there are reports discussing the influence of interfacial defects, charge transfer, and non-radiative energy transfer in, for example, nanostructured metal oxides and planar silicon heterostructures, less attention has been given to analyzing QD exciton dynamics when QDs are attached inside nanostructured porous silicon scaffolds that are known to have highly disordered interfaces with a high density of defect states. In

this work, by achieving highly luminescent, monolayer QD distributions in large surface area, nanostructured porous silicon thin films, we are able to straightforwardly probe the effects of interfacial defects and oxide thicknesses on QD lifetimes. This approach offers a significant advantage over techniques that utilize the deposition of several layers of QDs to achieve measurable signals, which can mask the influence of interfacial substrate defects in close proximity to the QDs. We first characterize the optical properties of monolayer CdTe/CdS QDs immobilized within nanostructured porous silicon/silicon dioxide (PSi/SiO_2) heterostructures and then vary the degree of thermally grown interfacial oxide thickness to study the impact of the local environment on the optical properties of the immobilized QDs. The use of the high surface area (~200 m^2 cm^{-3}) PSi three-dimensional matrix as the embedding medium for monolayer QDs enables straightforward tuning of the interfacial composition from Si to SiO_2 through controlled thermal oxidation. Completely oxidizing the PSi matrix to form a transparent nanostructured porous silica ($PSiO_2$) host matrix with a large conduction band offset leads to longer QD radiative lifetimes suitable for QD-integrated light emitting applications. In addition, use of a minimally oxidized PSi host matrix leads to faster QD PL decay times either through increased charge transfer into PSi or defect mediated non-radiative carrier recombinations. Charge transfer into the underlying PSi scaffold may be favorable for photovoltaic and photodetector applications wherein carriers can couple to lower energy sites present in the PSi.[151]

5.2 Fabrication

PSi films were fabricated by electrochemical etching of boron doped p+ silicon wafers (<100>, 0.01Ω-cm, Silicon Quest) in a two-electrode configuration. The electrolyte consisted of an ethanolic HF solution (3:8 v/v 49-51% aqueous HF:ethanol, Sigma Aldrich). Anodization was carried out in the dark for 334 s at an etching current density of 48 mA/cm^2 to form 10 μm thick PSi films with average pore sizes of 25 nm (**Figure 5.1a**). Each sample was rinsed thoroughly with ethanol and dried under a stream of nitrogen after the electrochemical etch. The samples were then subjected to varying thermal oxidation conditions in air as shown in **Table 5.1**. In order to completely oxidize the PSi framework, samples were oxidized at 1000 °C for 3 hrs.

Table 5.1. Thermal oxidation conditions for partially oxidized PSi samples.

Temperature (°C)	Time (min)		
500	5	30	180
800	5	30	180
1000	0.083	0.167	3

The oxidized samples were incubated for 10 min in 3% polydiallyldimethylammonium chloride (PDDA) aqueous solution at pH = 3.0, followed by a deionized (DI) water rinse to remove excess molecules. PDDA molecules impart a positive charge to the oxidized PSi substrates upon attachment, which facilitates the

monolayer assembly of colloidal QDs utilized for the studies conducted in this work. Visible light emitting CdTe/CdS QDs stabilized by glutathione were synthesized according to a procedure reported earlier.[152-153] The CdTe/CdS QDs were approximately 3.5 nm in diameter as estimated by transmission electron microscopy. Negatively charged CdTe/CdS QDs were electrostatically bound to the positively charged PDDA coated oxidized PSi surface during a 20 min incubation period to achieve monolayer QD distributions within the matrix. Unattached CdTe/CdS QDs were then washed away with thorough rinsing under DI water. A schematic representation of the material system under investigation – CdTe/CdS QDs attached inside an oxidized PSi film is shown in **Figure. 5.1b**.

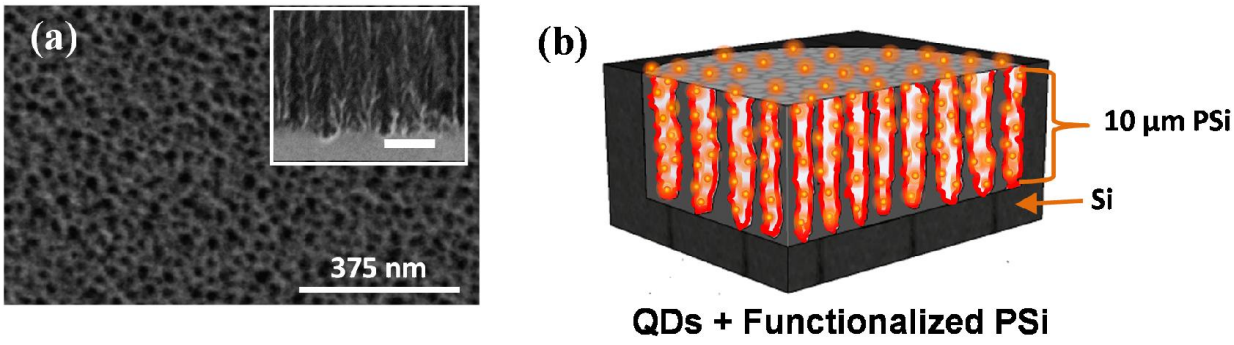

Figure. 5.1. (a) Top-view SEM image of PSi. The inset shows the cross-sectional SEM image of the PSi film with the scale bar indicating 200 nm. The pore diameters are ~25 nm and the inter-pore wall dimensions are ~9 nm. Nanowire branches present along the pore lengths are < 5 nm on average. (b) Schematic representation of CdTe/CdS QDs immobilized within a partially oxidized PSi thin film with an electrolytic PDDA polymer coating.

5.3 Experiments and Results

Absorbance and reflectance spectra were measured at room temperature with a Varian Cary 5000 UV-VIS-NIR spectrophotometer at a step size of 0.5 nm. Absorbance spectra were collected over a wavelength range of 300 nm - 800 nm. Reflectance spectra were collected over a wavelength range of 500 nm - 2000 nm using a spot size of ~6 mm. Continuous wave photoluminescence (CWPL) measurements were made using an Ar-Kr laser (Coherent Innova 70C) operating at a wavelength of 488 nm and power of 3 mW as the excitation source and a CCD spectrometer (Ocean Optics USB4000) fitted with a 1000 μm diameter optical fiber to record visible QD emission from the samples between 500 nm and 800 nm.

Based on Bruggeman effective medium theory and the measured blue-shift in the reflectance spectra of the PSi films after oxidation (not shown), we calculate the reduction in equivalent thin film optical thickness (ΔEOT), and estimate the oxide growth as shown in **Table 5.2**. We estimate that PSi films with interfacial oxide thicknesses ranging between approximately 0.4 nm and 2.7 nm were formed. The average length of a silicon oxide bond is 0.162 nm and the distance between the oxygen ions is 0.227 nm. So the minimum oxide thickness that may be grown is approximately 0.389 nm which is close to our minimum estimated oxide thickness of 0.4 nm. The range of oxide thickness estimated for a given thermal oxidation treatment condition arises from the estimations of the initial porous silicon thin film porosity, which affects the estimated effective refractive indices of the films both before and after thermal oxidation.

Table 5.2. Estimated decrease in EOT of PSi film and corresponding oxide thickness grown for varying thermal oxidation conditions.

Thermal Oxidation Parameters	ΔEOT (nm)	Estimated Oxide Growth (nm)
500 °C, 5 min	1191	<0.5
500 °C, 30 min	1582	0.5 – 0.7
500 °C, 3 hrs	1963	0.6 – 0.8
1000 °C, 0.083 min	2108	0.6 – 0.9
1000 °C, 0.167 min	2443	1.2 – 1.7
1000 °C, 3 min	3910	2 – 2.7

Figure 5.2a shows the shifts in reflectance spectra for the PSi substrates following the attachment of PDDA molecules and QDs over a narrowed spectral range for clarity. **Figure 5.2b** shows the absorbance and CWPL measurements of the QDs in solution. For

the minimally oxidized PSi matrix, the observed red-shift of ~15 nm in the reflectance spectrum after QD immobilization corresponds to ~10^{15} QDs captured within the PSi film and a near 8% surface area coverage, similar to what we reported in earlier work.[154] The smaller red-shift of ~9 nm that results from QD attachment to the $PSiO_2$ matrix can be explained by considering the additional oxide growth that reduces the effective pore size; the correspondingly reduced internal surface area in the $PSiO_2$ matrix leads to a reduction in the number of QDs attached [~10^{14} QDs for a 1 – 2% surface area coverage]. In both the NSi and $NSiO_2$ matrices, we estimate inter-QD spacing to be greater than 10 nm, which is sufficient to suppress strong inter-QD carrier coupling.[155-156]

The measured CWPL spectra of the immobilized QDs in both substrates, as shown in **Figure 5.2c**, show good spectral agreement with the CWPL of QDs in solution (**Figure 5.2b**). The intensities of the CWPL peaks scale with the number of QDs in the sample volume and, in the case of the QDs attached to the sub-nm oxidized PSi matrix, some of the QD emission is absorbed by the PSi. As reported previously, the spectral fringes seen in the CWPL spectra in **Figure 5.2c** confirm QD infiltration and immobilization throughout the scaffold and are a signature of Fabry-Perot interference.[19] The inset shows camera images for the two samples under 365 nm UV excitation with the strong QD PL directly visible by the naked eye.

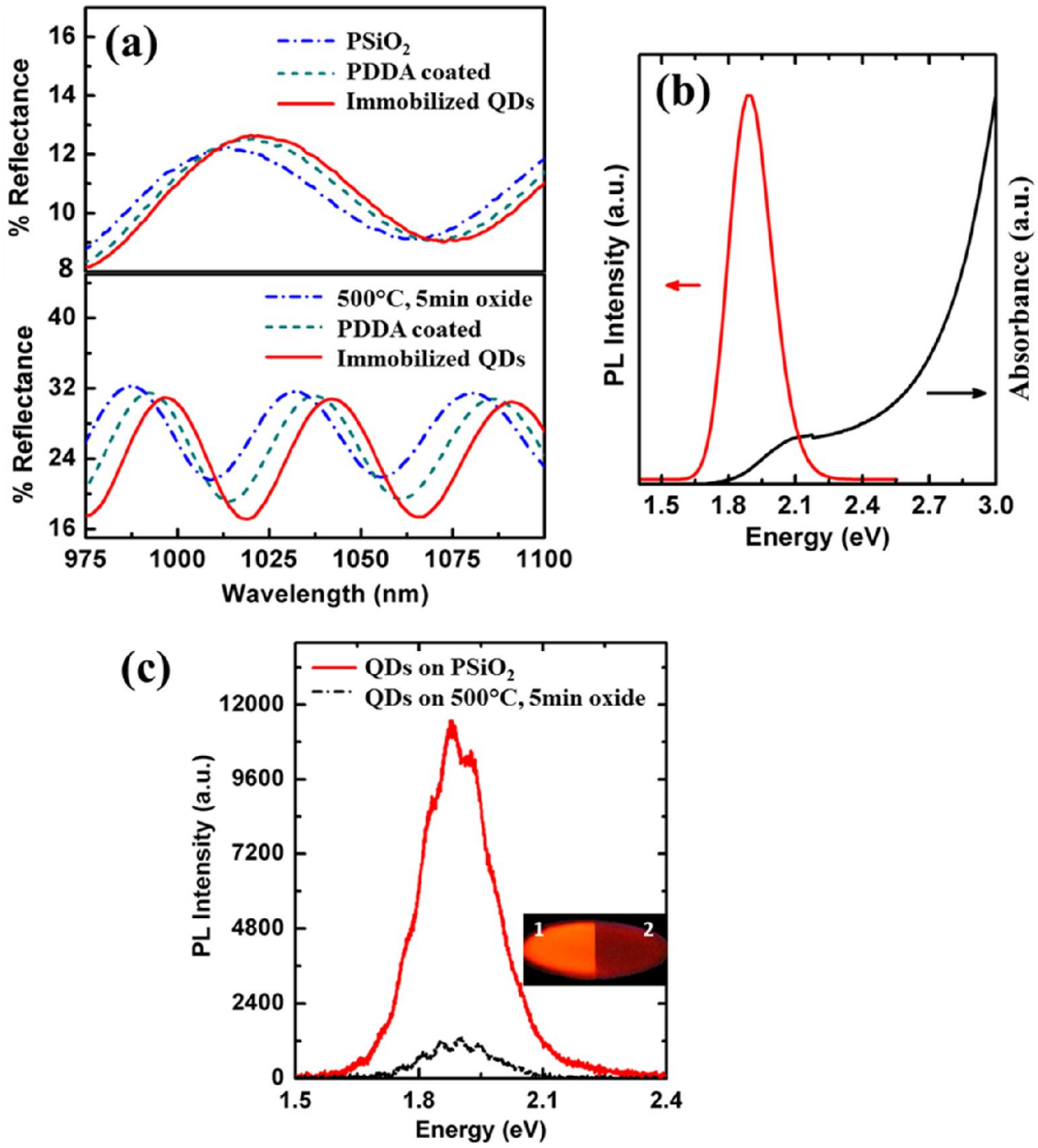

Figure 5.2. (a) Reflectance spectra measured for PSi thin films following complete ($PSiO_2$) or partial (PSi oxidized at 500 °C for 5 min) oxidation, PDDA coating, and QD attachment. (b) Absorbance and CWPL spectra for CdTe/CdS QDs in 0.1 mM aqueous solution. (c) CWPL spectra of monolayer QDs immobilized in a $PSiO_2$ thin-film and in a sub-nm

oxidized PSi thin-film. The inset shows camera images of the samples under UV (365 nm) excitation: 1- $PSiO_2$ with QDs and 2 - Partially oxidized PSi with QDs.

Time-resolved photoluminescence (TRPL) measurements were carried out with an intensified CCD detector (iDUS490A, Andor Technology) attached to a spectrograph (Shamrock, SR303i, Andor Technology). A Nd:YAG Q-switched laser (Minilite-10, Continuum Inc.) operating at a wavelength of 355 nm in low power mode (10 mW) with 10 ns pulse duration and 10 Hz repetition rate was used as the excitation source for the TRPL experiments.

Figure 5.3 shows that QDs immobilized in $PSiO_2$ exhibit exciton lifetimes that are closely matched to those of QDs in solution, with decay times (τ) of ~78 ns, consistent with prior work.[157] All data in **Figure 5.3** are for measurements at the peak emission wavelength of the QDs (~1.85 eV). **Figure 5.3b** shows the evolution of QD lifetimes with increasing thermal oxidation of the PSi matrix at 1000 °C. These measurements suggest that when PSi has an interfacial oxide growth at high temperature and with thickness greater than approximately 1 nm, the exciton lifetimes are approximately the same as those for QDs attached in porous silica substrates ~78 ns and QDs in solution. This result rules out any possibility of long-range non-radiative energy transfer from the QDs to the partially oxidized PSi framework across a high quality interfacial oxide and also suggests that the high-temperature grown oxide is largely defect free with excitons largely confined to the QDs themselves. Defect densities of the thermally grown SiO_2 have been extensively studied and, consistent with our conclusion, it has been shown that high temperature

thermal oxidation results in a relatively low number of Si/SiO_2 interface trapped charges and oxide trapped charges with fewer sub-oxide species and primarily $Si\text{-}SiO_2$ groups (interface defect density $<10^{10}$ cm^{-2} eV^{-1}).[158-159] Moreover, due to the unchanged exciton lifetime of QDs in solution and in the $PSiO_2$ matrix, the results in Fig. 3 suggest that the conformal PDDA coating in the oxidized PSi matrix does not influence QD exciton dynamics within the matrix and allows for uniform, monolayer attachment of the QDs.[106, 160-161] The interfacial effects of the disordered nature of PSi, arising from varying nanocrystallite sizes, density of states, and defect levels at the band edges, become apparent when the QDs are immobilized in a sub-nm oxidized PSi framework, with exciton lifetimes decreasing by nearly five times to ~16 ns, as shown in **Figure 5.3a**. Prior studies suggest that low temperature oxide growth increases intrinsic stress and oxide densities.[162] Accordingly, the low temperature (500 °C) thermal oxidation of PSi likely results in a substantially higher interfacial defect density partially attributable to the presence of sub-oxides, Si-O-H groups with some Si-H bonds still present, intrinsic stress, and trapped charges.[160] **Figure 5.3c** shows the influence of low temperature grown interfacial oxide thickness on QD PL lifetimes; QD PL lifetimes vary from 16 – 52 ns for oxide thicknesses ranging from less than 5 Å to approximately 0.8 nm. It is clear that the QD PL lifetime is directly affected by the interfacial oxide thickness within this thickness range and for the lower quality oxide. We note that for an oxide thickness between 0.6 nm – 0.9 nm for both the low and high temperature oxidation conditions, QD lifetimes close to 50 ns are measured, further indicating an oxide thickness dependent QD lifetime in the porous heterostructures. A plot of the peak QD PL lifetimes versus the thermally grown interfacial

oxide thickness in the PSi samples under all oxidation conditions reveals an exponential dependence, as shown in **Figure 5.3d**, and is indicative of charge transfer dynamics across the oxide interface.

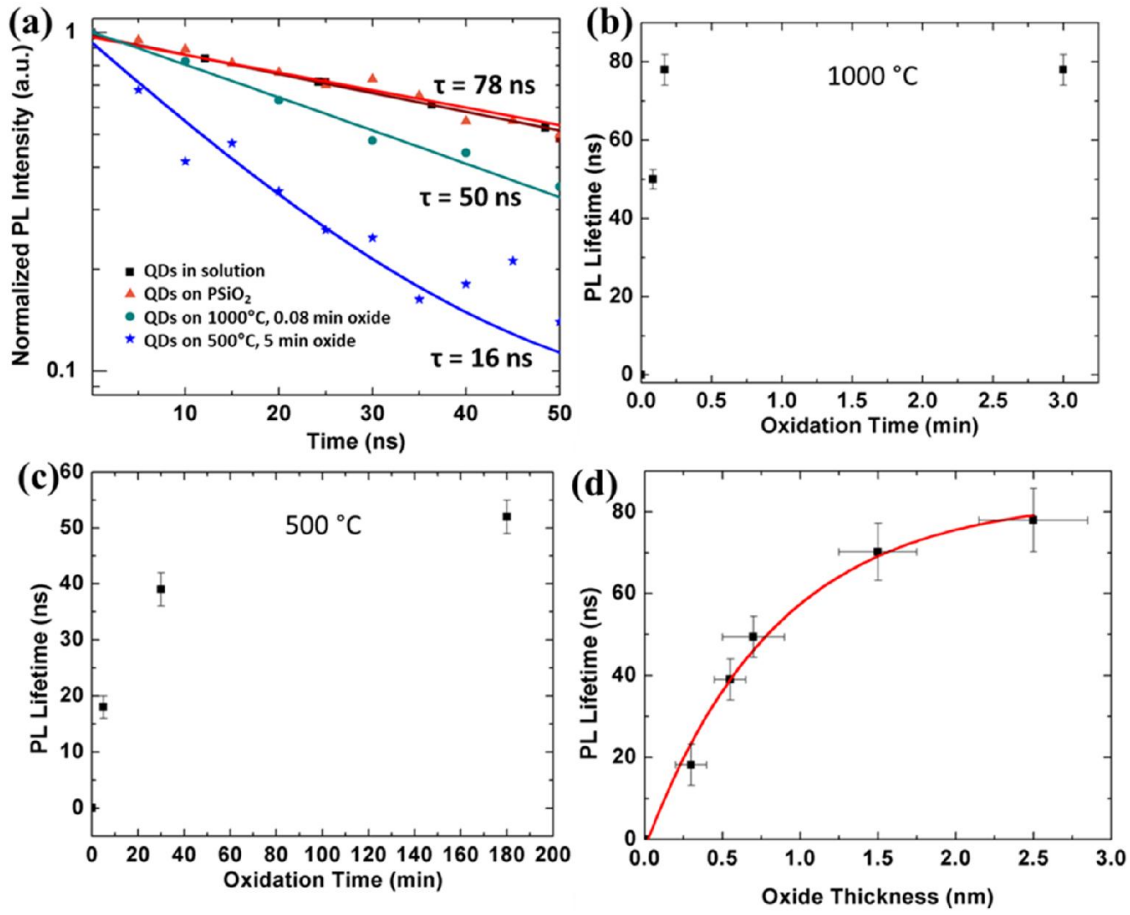

Figure. 5.3. (a) Time-resolved photoluminescence measurements of QDs in solution (squares), on $PSiO_2$ (triangles), on 1000°C, 0.08 min oxidized PSi (circles), and on 500°C, 5 min oxidized PSi (stars) with solid lines indicative of a single exponential decay. (b) Evolution of QD PL lifetime with increasing thermal oxidation at 500 °C. (c) Evolution of QD PL lifetime with increasing thermal oxidation at 1000 °C. (d) Relationship between QD PL lifetime and thermally grown oxide thickness in oxidized PSi matrices. Solid line

is indicative of a single exponential fit. All data are measured at peak wavelength of QD emission.

To provide insight into the mechanisms responsible for the different QD exciton lifetimes in PSi matrices with different interfacial oxide quality and thickness, we propose possible exciton quenching pathways, which are shown in **Figure 5.4** along with the relative energy levels for the QDs and embedding matrices. The energy levels are based on those reported in the literature for PSi and CdTe/CdS QDs.[163-168] Prior studies have suggested that CdTe/CdS QDs may exhibit either Type I or Type II behavior depending upon core and shell thickness and the influence of lattice strain.[169] Discrepancies in the band offset calculations between CdTe and CdS can also change the suggested classification of the heterostructure.[157, 163] The type of QD emission observed in our experiments is mostly Type II centered near 1.85 eV. Based on the relative position of the energy levels, the holes are expected to be strongly confined within the core while the electrons are most likely delocalized over the CdS shell and, in the case of the sub-nm oxidized PSi substrate (**Figure 5.4b**), may couple into the PSi region via an energetically favorable transition. As a result, exciton dynamics are greatly affected by electron wave function overlap with surface and substrate states which is further evidence of the possibility of charge transfer. Since the inter-QD separations estimated in the PSi frameworks suggest minimal QD-QD exciton coupling will occur, interfacial defects and thicknesses of the interfacial oxide region between the QDs and PSi scaffold are expected to dominate QD exciton dynamics, which is consistent with our experimental results shown in **Figure 5.3**.[170-171] The reduced exciton lifetime for the QDs immobilized within the PSi

matrix with thinner oxides is probably due to exciton quenching, either through non-radiative carrier recombination or phonon assisted transitions influenced by defect sites within the oxide as well as the high density of disordered states present in the PSi substrates where defect densities may be close to 10^{16} cm^{-2} (**Figure 5.4b**).[172-173] We note that some studies of the non-radiative phonon transition processes related to PSi have been performed but are not entirely understood.[167, 47] Photocurrent studies investigating the role of a thin high quality oxide at the interface would be able to provide greater insights into charge transport within such complex structures. For the case of QDs attached to completely oxidized $PSiO_2$ substrates, the prolonged high temperature oxidation is expected to result in lower carrier trap sites within the immediate vicinity of the QDs. The thicker oxide also prohibits tunneling of carriers to PSi disordered states and suppresses non-radiative carrier recombination pathways. As a result, the dominating photo-physical mechanisms for QDs in $PSiO_2$ are exciton generation and radiative recombination (**Figure 5.4a**). Therefore, $PSiO_2$ based optical structures such as microcavities and distributed Bragg reflectors with embedded QD emitters are a potentially advantageous platform for QD based light emitting applications.[42] While the work presented here provides insights into the importance of the interface in colloidal QD-integrated porous silicon heterostructures, further experiments that can resolve exciton lifetimes below 10 ns and therefore allow for the possibility of multi-exponential fits are needed to more definitively elucidate the radiative and non-radiative mechanisms involved in QD exciton decay within three-dimensional porous heterostructures.

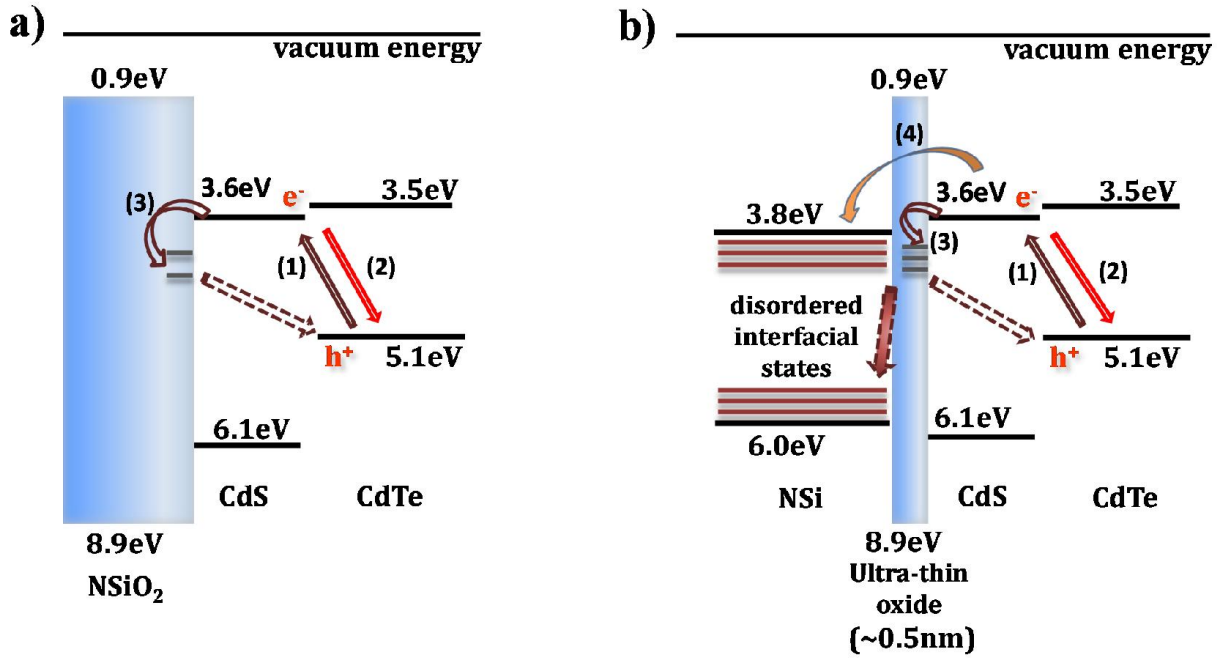

Figure 5.4. Energy level representations of CdTe/CdS QDs immobilized in a) completely oxidized $PSiO_2$ and b) PSi with ultra-thin oxide. Possible photo-physical mechanisms are: (1) absorption of photon energy and creation of an exciton. (2) Radiative decay of exciton through CdTe/CdS band-edge emission. (3) Migration of an exciton to lower energy sites in the interfacial oxide, causing exciton dissociation. The mobile electron may then remain trapped for extended periods of time in oxide defect states or non-radiatively decay either to the CdTe/CdS valence band or relax to the PSi valence band in b) via coupling to the disordered PSi interfacial states and decaying via phonon modes. (4) The energetically favorable transition of electrons from the CdTe core to the PSi interfacial states in b). The energy levels shown are based on those reported in [163, 165-168].

5.4 Conclusions

In summary, we demonstrate the influence of interfacial oxide thickness on attached QDs in high surface area PSi structures that may advantageous for QD-PSi based applications spanning photovoltaics, energy storage, photodetectors, and light sources. By altering the coupled QD material interface from a sub-nm oxidized PSi to a completely oxidized $PSiO_2$ framework, we are able to significantly suppress non-radiative recombination pathways of photogenerated excitons and achieve nearly 5 times longer exciton lifetimes of ~78 ns that are on par with QDs in solution. The exponential dependence of lifetime on interfacial oxide thickness suggests that charge transfer processes play an important role in the exciton dynamics. Further theoretical calculations of exciton localization and transfer mechanisms in the PSi-QD heterostructures and temperature dependent, time-resolved spectroscopic studies could help provide a greater understanding of exciton dynamics within QD integrated porous silicon scaffolds.

6. OPTICAL RESPONSE OF MONOLAYER CDTE/CDS QDS TO X-RAYS AND GAMMA-RAYS

6.1 Introduction

Over the past decade, there have been tremendous improvements in the synthesis of colloidal quantum dots (QDs), enabling the artificial engineering of wavelength specific, strong light emitters with controllable surface chemistries. Due to their unique optical properties, QDs have found many applications ranging from photovoltaics,[48, 140-143] photodetectors,[51-52] fluorescence probes,[50, 174-175] and LEDs[131-135] to radiation scintillators,[144-145] radiation oncology,[176] and X-ray imaging screens.[177] For some of these applications, knowledge of the influence of highly energetic photons on the optical properties of QDs immobilized on a substrate is essential for achieving reliable and robust QD-based device operation over extended periods of time in high risk and high radiation environments. Several studies have examined the radiation hardness of QD-based devices grown by metal organic chemical vapor deposition or molecular beam expitaxy.[178-179] Very few studies have investigated the effects of high energy radiation on colloidal QDs. One study reported rapid degradation of CdSe/ZnS colloidal QDs in hexanes under gamma-ray (γ-ray) irradiation in air[180] and another showed that 20 keV picosecond electron pulses incident on multilayer close-packed CdSe/ZnS colloidal QD films lead to charged exciton species and multiexciton states.[181] However, the influence of high energy photons on the optical properties of colloidal QDs immobilized on a substrate remains to be explored in detail.

In this work, we report a detailed analysis of the optical properties of sub-monolayer CdTe/CdS colloidal QDs immobilized within porous silica ($PSiO_2$) scaffolds under increasing X-ray and γ-ray exposure doses in air and nitrogen environments. Recent work demonstrated that colloidal QDs may be dispersed in a $PSiO_2$ framework with little influence on their solution phase optical properties.[154] The exceptionally high surface area of $PSiO_2$ (~200 m^2 cm^{-3}) enables the attachment of a large quantity of QDs (~10^{14} QDs for 1 – 2% surface area coverage), spaced sufficiently far apart to suppress inter-QD exciton couplings.[154] This facilitates the formation of highly luminescent QD distributions that are surface-bound but still largely accessible for surface modification. Using the QD-$PSiO_2$ platform, we can study QD radiation sensitivity on a solid surface that mimics a potential device configuration while preventing inter-QD exciton couplings that may otherwise encourage other avenues for non-radiative exciton annihilation and interfere with conclusions that are drawn purely from radiation induced changes in exciton dynamics.[170-171, 182]

Here, a sub-monolayer of CdTe/CdS QDs **(Figure 6.1)** are electrostatically attached within a 10 μm thick $PSiO_2$ framework **(Figures 6.2-6.4)**, although other types of QDs could be similarly studied using this approach. HRTEM images were acquired using FEI Tecnai Osiris TEM operating at 200 kV. The samples for TEM analysis were prepared by placing a drop of QDs solution onto carbon coated copper grid and wiping off the excess of the liquid. **Figure 6.3** contrasts the high optical density achievable by using the porous scaffold with that achieved by depositing the QDs on a planar silicon sample obtained by a fluorescence microscope.

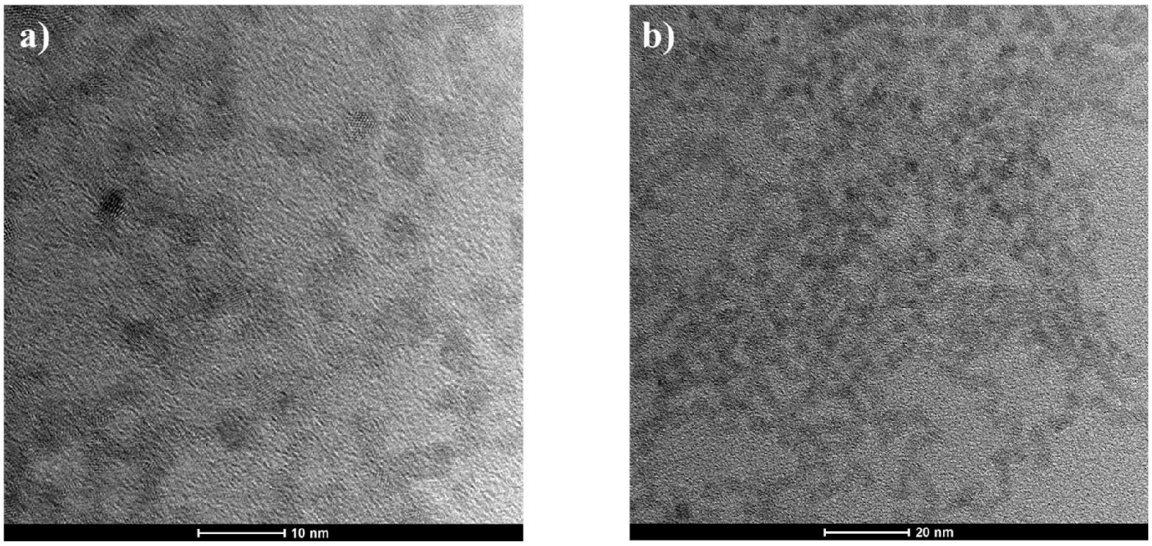

Figure 6.1. TEM images of the ~3.5 nm CdTe/CdS QDs.

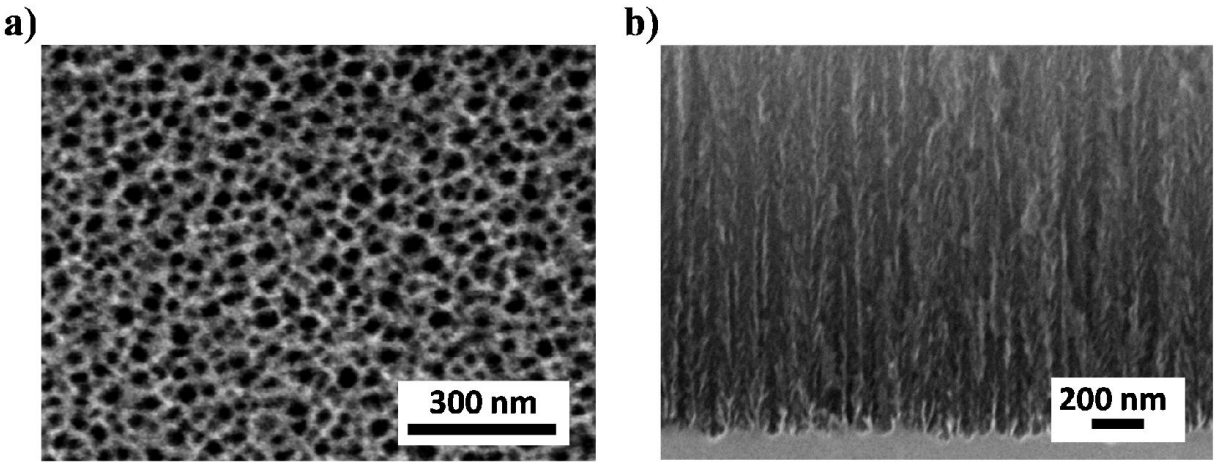

Figure 6.2. SEM images of freshly prepared PSi showing a) top view and b) cross-sectional profile. The average pore sizes are ~25 nm with inter-pore nano-wall dimensions of ~9 nm on average. Nanowire branches present along the pore lengths are < 5 nm on average.

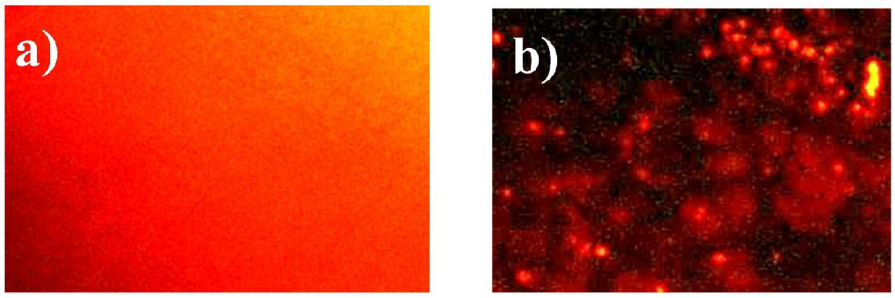

Figure 6.3. Fluorescence microscopy images of CdTe/CdS QDs attached to PDDA coated substrates: a) 10 μm thick $PSiO_2$ film and b) flat Si sample. Due to the large internal surface area of the $PSiO_2$ film, a significantly larger quantity of QDs is attached to $PSiO_2$ compared to flat Si, as is indicated by the brighter fluorescence microscopy image.

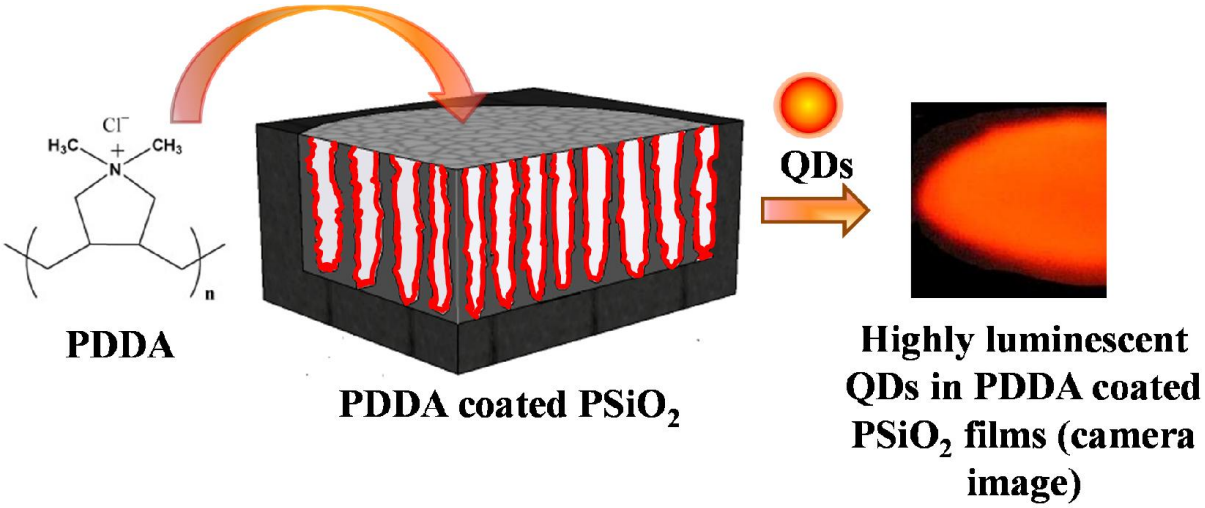

Figure 6.4. Schematic illustration of the attachment of CdTe/CdS QDs to PDDA coated $PSiO_2$ film and a camera image of the sample under UV lamp excitation at 365 nm.

The continuous wave and absorbance spectra of the CdTe/CdS QDs used in the study are shown in **Figure 6.5**.

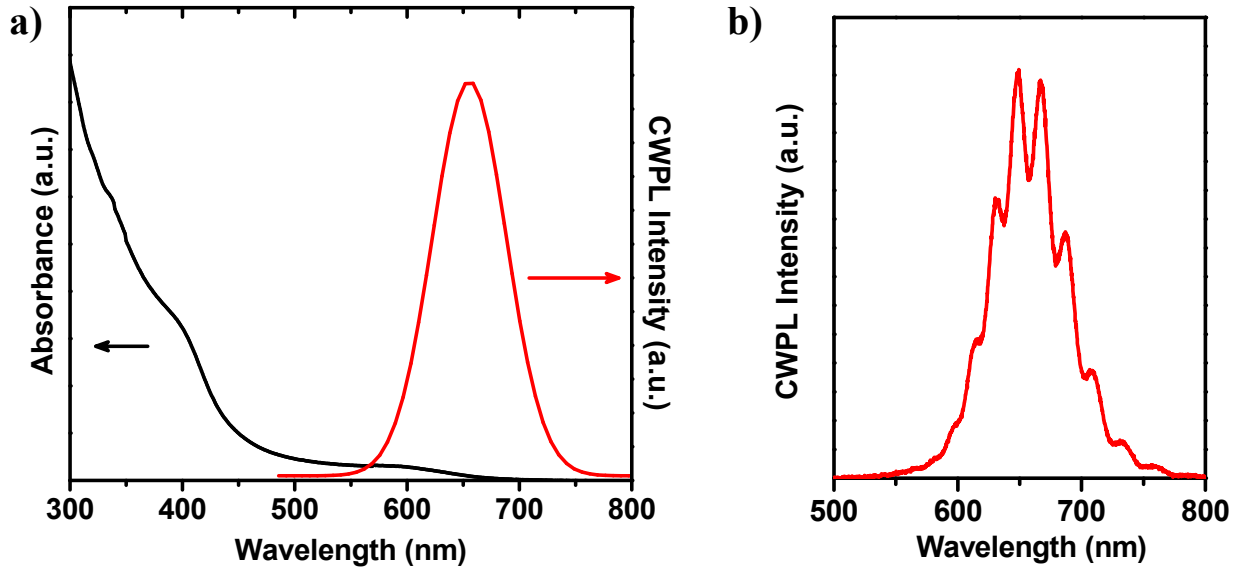

Figure 6.5. a) Absorbance and CWPL spectrum for CdTe/CdS QDs. b) CWPL spectrum of sub-monolayer CdTe/CdS QDs immobilized in a $PSiO_2$ thin-film.

We show that cumulative 10 keV X-ray irradiation of the QD-$PSiO_2$ samples in air from 2.2 Mrad(SiO_2) to 6.6 Mrad(SiO_2) leads to an exponential decrease in QD peak emission intensity and a concurrent exponential blue-shift of the QD peak emission to higher energies due to accelerated photo-oxidative effects. Irradiating QD-$PSiO_2$ samples with higher energy and more highly penetrating 662 keV γ-rays allows for enclosure of the samples in nitrogen purged vials to suppress the effects of radiation-induced accelerated photo-oxidation; however, the QDs experience severe photodarkening with significant loss of emission intensity for less than 1 Mrad(SiO_2) total exposure dose. Importantly, it is shown that the effects of X-ray and γ-ray irradiation are largely reversible following a surface treatment procedure that involves the exposure of QDs to a thiol-containing

solution. Consequently, this work provides a means of assessing the influence of high energy radiation and surface treatments on the photophysical properties of QDs for future QD-integrated device applications, and offers exciting avenues into developing quantifiable, low cost, flexible, large area, re-useable radiation dosimeters for space and other high-risk environments where low mass and robustness are key criteria for selecting dosimeters for extended space missions.[12, 183]

6.2 Interactions of High Energy Photons with Matter

It is well known that high energy photons such as X-rays and gamma-rays (γ-rays) interact primarily with irradiated materials through ionization events. Depending upon the incident photon energy and atomic number (Z) of the irradiated material, two types of effects are known to be responsible for photo-ionization events. Photoelectric effects dominate for low photon energies (usually <100 keV) scaling approximately with Z^4 while Compton effects are dominant for higher photon energies (0.8 MeV upto 4 MeV) and even for lower photon energies in materials with low Z.[184-185] The interaction of 10 keV X-rays with the QD-PSiO_2 sample results in complete absorption of primary photons through interaction with atoms and the generation of photoelectrons whose energy depends on energy of incident X rays and binding energies of electrons in QDs and silicon. On the other hand, 662 keV γ-rays interact with QD-PSiO_2 samples by the partial transfer of their energy resulting in the creation of Compton electrons and Compton scattered photons. The energy transferred to Compton electrons primarily depends on the energy of the γ-rays with higher energy rays transferring a greater percentage of their energy to Compton electrons

and the scattering angles. Thus, high energy photons can generate thousands of electron-hole pairs, the primary source of radiation induced damage and ionization effects in irradiated materials. In this work, we focus on furthering our understanding of the effects of X-rays and γ-rays on QD-$PSiO_2$ samples in air and dry nitrogen environments that suppress photo-oxidative related effects[186].

6.3 Sample Preparation

Nanostructured PSi films were fabricated by electrochemical etching of boron doped p+ silicon wafers (<100>, 0.01Ω-cm, Silicon Quest) in a two-electrode configuration. A platinum wire counter-electrode and silicon wafer with an exposed area of 1.7 cm^2 were mounted on a silver plate in a Teflon etching cell. The electrolyte consisted of an ethanolic HF solution (3:8 v/v 49-51% aqueous HF:ethanol, Sigma Aldrich). Anodization was carried out in the dark for 334 s at an etching current density of 48 mA/cm^2 to form 10 μm thick nanostructured porous silicon films with average pore sizes of 25 nm. (**Figure 6.2**) Each sample was rinsed thoroughly with ethanol and dried under a stream of nitrogen after the electrochemical etch. The samples were then cleaved in half and thermally oxidized at 1000 °C in air for 3 h to form $PSiO_2$ thin-films. Little sample-to-sample variation is expected when analyzing the effects of radiation on irradiated versus control sample halves that originated from the same $PSiO_2$ film. The $PSiO_2$ samples were incubated for 10 minutes in 3% poly(diallyldimethylammonium chloride) (PDDA) aqueous solution at pH = 3.0, followed by a deionized (DI) water rinse to remove excess

molecules. PDDA molecules (~1 nm) impart a positive charge to the $PSiO_2$ substrates upon attachment (**Figure 6.4**).

CdTe/CdS QD preparation method: Glutathione (GSH) stabilized CdTe/CdS QDs were synthesized according to a modified procedure[153, 187] where, negatively charged CdTe/CdS QDs electrostatically bind to the positively charged PDDA coated $PSiO_2$ surface during a 20 minute incubation period. Unattached CdTe/CdS QDs were then washed away with thorough rinsing under DI water.

6.4 Results and Discussions

6.4.1 10 KEV X-RAY IRRADIATIONS

Figure 6.6 shows the exponential decrease in PL peak intensities for CdTe/CdS QDs attached to $PSiO_2$ scaffolds under increasing 10-keV X-ray exposure (36.7 krad(SiO_2)/min) in air.

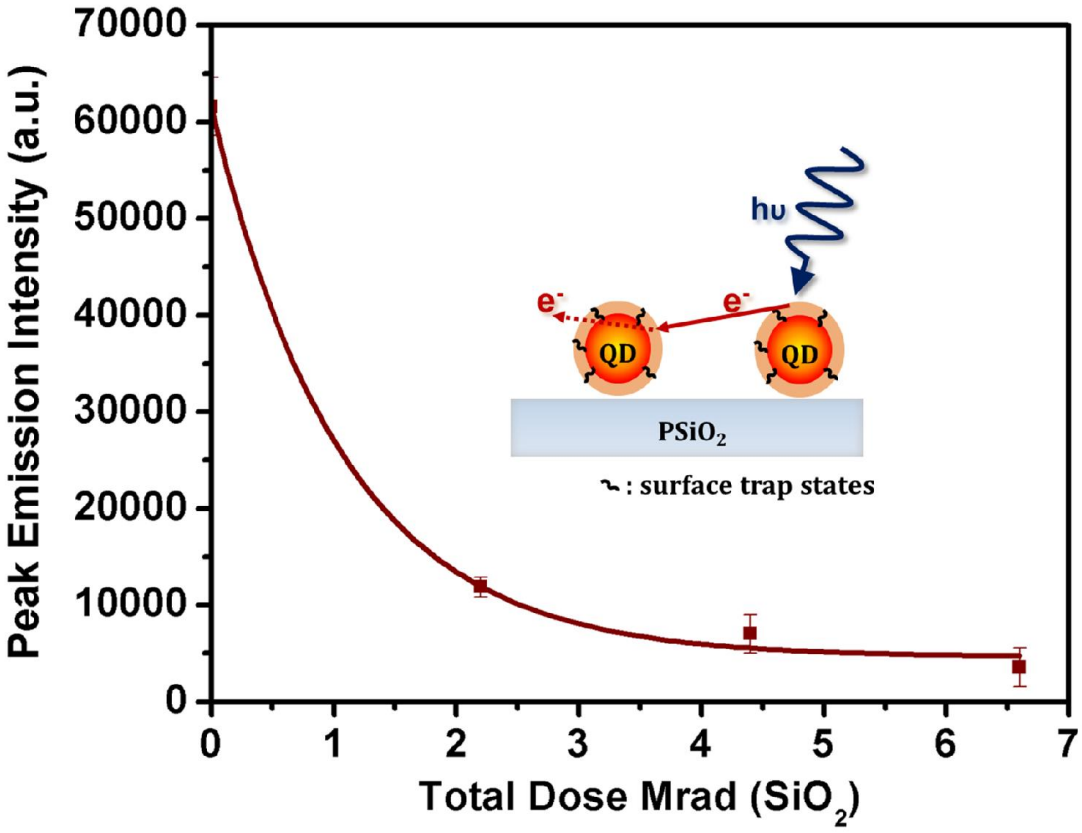

Figure 6.6. Decrease in CdTe/CdS QD PL peak intensities following increasing total exposure dose under X-ray irradiation. The solid line is a single exponential fit. Inset: Schematic representation of the interaction of 10 keV X-rays (hυ) with a QD. The ejected photoelectron is denoted as e^-. Radiation induced surface transformations and photocatalytic oxidation of the thiol ligands results in the formation of surface trap states.

Since the photoelectric effect dominates for low energy (<100 keV) photon interactions with materials, the interaction of 10 keV X-rays with the $PSiO_2$-QDs results in absorption of the primary photons through interactions with atoms and the generation of photoelectrons whose energy depends on the energy of the incident X-rays and the binding

energies of electrons in the QDs and $PSiO_2$ framework.[185, 188] As a result, the primary source of radiation induced damage for X-ray irradiated colloidal CdTe QDs is most likely through the creation of secondary electron-hole pairs formed along the track of an ejected photoelectron. $PSiO_2$-QD samples were irradiated at room temperature with 10 keV X-rays at a dose rate of 36.7 krad/min(SiO_2) in an ARACOR Model 4100 Irradiator for exposure times varying from 1 h to 3 h in air. As illustrated in the inset of **Figure 6.6**, the ejected primary photoelectron may interact with neighboring QDs, resulting in the creation of secondary electron-hole pairs along the track of the primary photoelectron. Acquired charges on the QDs may initiate a permanent dark state within the QDs wherein non-radiative Auger processes are known to greatly influence the relaxation of excited electrons through Coulombic interactions with coupled holes.[172] Recent work by Zhao et. al. offers another possibility; charged QDs enter an intermediate state or "grey state", wherein they are weakly emissive with much faster radiative decays.[189] However, multiple charges present on QDs would lead to dominant non-radiative Auger processes and a complete dark state within the QDs. Additionally, in the presence of air and highly ionizing radiation, thiol-capped CdTe/CdS QDs likely undergo accelerated photooxidation of the nanocrystal/ligand complex. Previous research has demonstrated air-induced or UV-catalyzed oxidation of II-VI chalcogenides such as CdS and CdTe as well as CdSe nanocrystals coated by hydrophilic thiols. Upon photooxidation, chalcogenides such as S or Te oxidize to form sulfates and oxides or sub-oxides of Te, respectively. In turn, this photooxidation results in the desorption of Cd^{2+} ions or CdTe complexes from the core.[190-191] For thiol coated QDs, photogenerated holes in the QDs photocatalytically lead to

oxidation of the thiol ligands and the formation of disulfides.[192] Such surface transformations or re-arrangements of surface capping agents may create trap sites present on the QD surface, core/shell interface or within core/shell structure itself, and alter QD exciton dynamics through trap-mediated or Auger-assisted non-radiative carrier recombination. Hence, the cumulative effects of increased carrier traps, photoionization, and multiexciton creation are the most likely causes for the exponential decrease of peak QD intensities shown in **Figure 6.6**.

In order to investigate the role of photooxidation, X-ray photoelectron spectroscopy (XPS) measurements were carried out on an X-ray irradiated CdTe/CdS QD-PSiO$_2$ sample. As shown in **Figure 6.7**, the analysis focused on the S2p$^{3/2}$ and Te3d$^{5/2}$ core levels associated with CdS and CdTe bonds, respectively. After X-ray irradiation, there is an increase in the CdS binding energy from approximately 161 eV to 161.6 eV, which is consistent with oxidation, and a new peak appears at 575.9 eV, suggesting the formation of sub-oxides of Te. These results support the conclusion that the QDs are oxidized as a result of X-ray irradiation.

Previous studies have shown that the exposure of photocatalytically oxidized chalcogenide QDs to thiol-capping agents can help replace unstable disulfides that form during the photooxidation process with thiol ligands to maintain the stability of the QDs.[192] Accordingly, an X-ray irradiated CdTe/CdS QD-PSiO$_2$ sample was exposed to a solution of glutathione containing free thiols to replace the disulfides, help re-passivate surface dangling bonds of Cd ions, and possibly reduce photoionized Te atoms.[193] 100 μL of a freshly prepared aqueous glutathione solution (0.3 mM, pH = 7.3) was pipetted onto

irradiated QD samples for varying amounts of time (5 min, 10 min, 20 min, 30 min, and 40 min). The samples were then rinsed with DI water and dried under nitrogen. An incubation time of 25 min was found to be sufficient to achieve almost complete recovery of QD emission intensities.

As shown in the XPS spectra in **Figure 6.7**, after the glutathione treatment, the peak at 575.9 eV is significantly decreased, suggesting removal of the sub-oxides of Te by the free thiols. In addition, two distinct peaks appear at energies near 162.1 eV and 160.9 eV. The higher energy peak at 162.1 eV suggets the formation of sulfates, while the peak near 161 eV indicates the re-formation of the CdS shell. These results suggest possible repassivation of the core/shell structure.

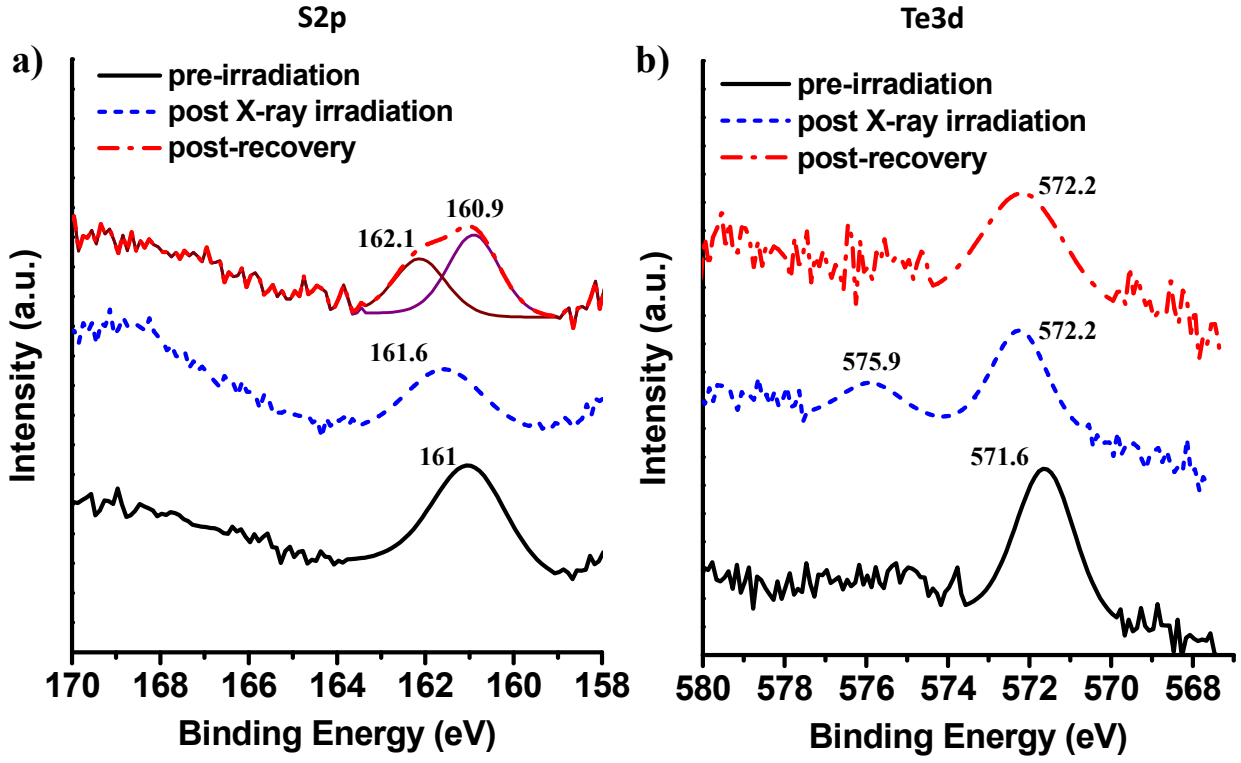

Figure 6.7. XPS spectra acquired from CdTe/CdS QDs attached to $PSiO_2$ after preparation, post X-ray irradiation, and post glutathione surface treatment: a) CdS S2p and b) $Te3d^{5/2}$

core levels. Values shown represent peak binding energies (eV) that have been calibrated to the lowest energy carbon peak at 284.8 eV.

Continuous wave photoluminescence (CWPL) measurements were then carried out to determine the effect of the glutathione treatment on the QD emission. As shown in **Figure 6.8a**, following the surface treatment, there is an almost complete recovery of the net PL intensity, which decreased by over an order of magnitude following a total X-ray exposure dose of 4.4 Mrad(SiO_2) in air. A 0.035 eV blue-shift in QD emission wavelengths is also observed following exposure to the free-thiols in solution, which likely results from the etching of the oxide species of S and Te formed during the X-ray irradiation. QD emission energy can be related to the effective QD diameter via **equation (6.1)**, where $E_g(QD)$ is the bandgap of the QD, h is Planck's constant, a is the diameter of the QD, m_{eff} is the effective mass of an electron, and $E_g(bulk)$ is the bulk bandgap energy.[194]

$$E_g(QD) = \left(\frac{h^2}{8m_{eff}a^2}\right) + E_g(bulk) \quad (1)$$

Given that $E_{g(bulk)}$ ~1.5 eV [195] and m_{eff} ~0.11m_e [196] for CdTe, we estimate that the effective QD diameter decreases by Δa ~130 pm for the measured $\Delta E_{g(QD)}$ ~0.035eV, given that the initial QD diameter is ~3.5 nm. This corresponds to a decrease in effective QD diameter by about one atomic layer and increased exciton confinement that shifts the QD emission to higher energies. The magnitude of the PL peak blue-shift is related to the total ionizing dose of X-rays irradiating the QD-$PSiO_2$ samples. **Figure 6.9** shows the corresponding increase in QD peak emission energy after the glutathione surface treatment procedure is

performed on samples exposed to X-ray irradiation to doses of 2.2 Mrad(SiO_2), 4.4 Mrad(SiO_2), and 6.6 Mrad(SiO_2).

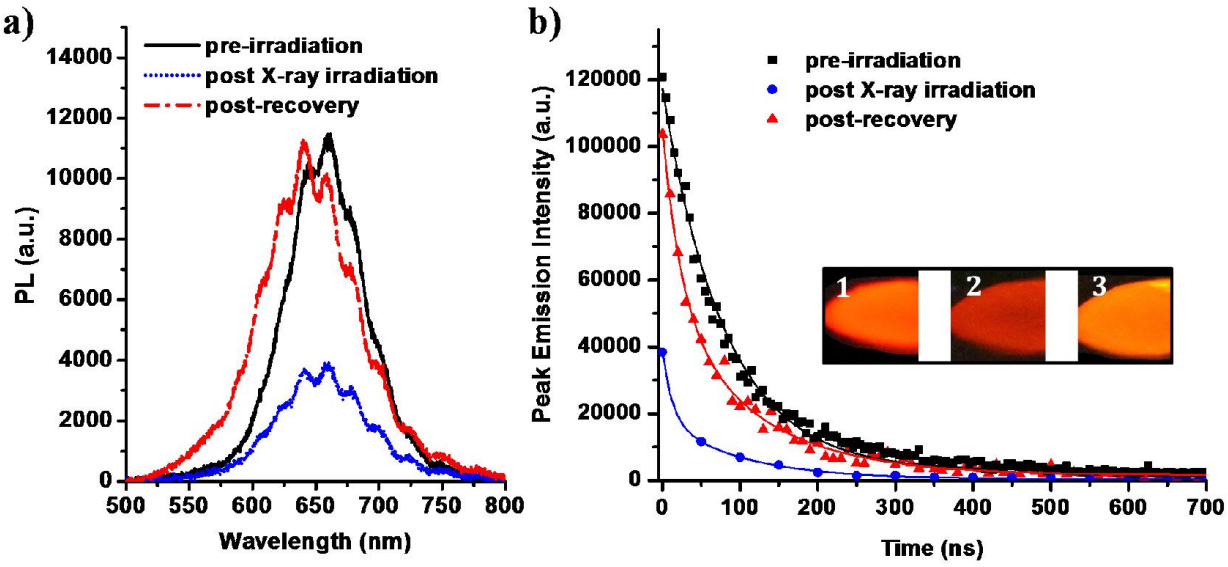

Figure 6.8. a) CWPL measurements of sub-monolayer CdTe/CdS QDs immobilized within a $PSiO_2$ thin-film as-prepared (black line), following a 4.4 Mrad(SiO_2) X-ray irradiation in air (blue dotted line), and post glutathione treatment (red dash-dotted line). The distinct fringes present in the spectra confirm QD infiltration and immobilization throughout the $PSiO_2$ layer.[197] b) TRPL measurements for CdTe/CdS QD-$PSiO_2$ samples as-prepared (black squares), following a 4.4 Mrad(SiO_2) X-ray irradiation (blue circles) and post glutathione treatment (red triangles). All data points are fit to a single exponential decay. Insets show camera images of samples under UV (365 nm) excitation: 1-pre-irradiation, 2-post X-ray irradiation, and 3-post glutathione treatment.

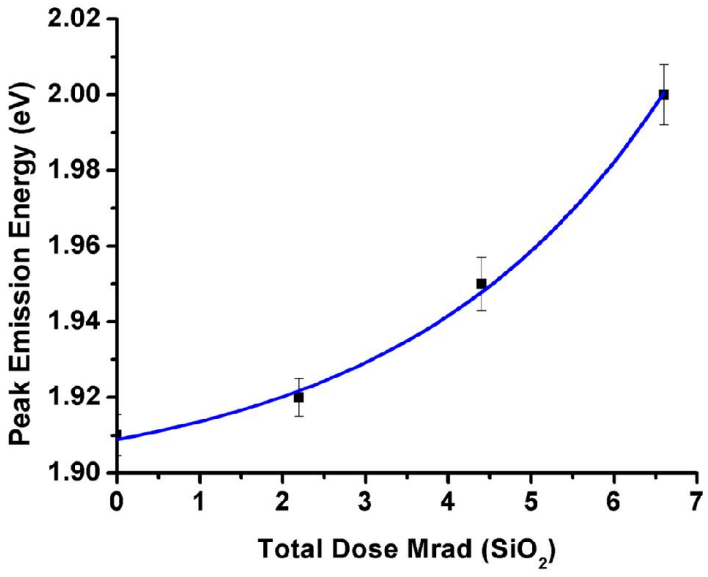

Figure 6.9. Increase in QD peak emission energy following surface recovery treatment for CdS/CdTe QD-PSiO$_2$ samples subjected to increasing X-ray doses. An exponential line fit is shown.

Control experiments show that the glutathione surface treatment procedure does not lead to increased PL intensity or a blue-shift in the PL spectrum when performed on a non-irradiated QD-PSiO$_2$ sample **(Figure 6.10)**.

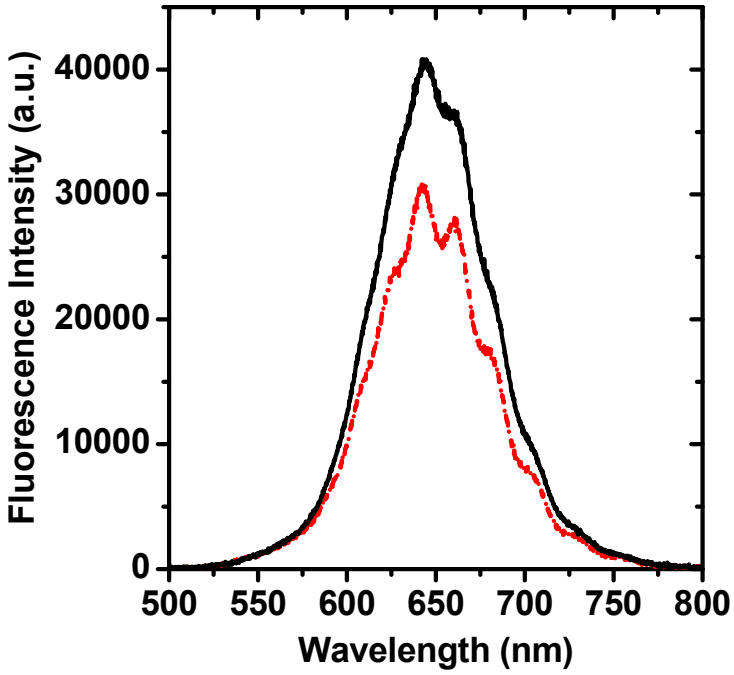

Figure 6.10. Fluorescence spectra of a QD-PSiO$_2$ sample before (black solid line) and after (red dashed line) incubation in 0.3 mM aqueous glutathione solution for 20 min. The latter measurement was performed after a 2 h time interval that corresponds to the time duration of a 4.04 Mrad(SiO$_2$) total ionizing dose X-ray irradiation carried out at a dose rate of 36.7 krad/min(SiO$_2$). The QD-PSiO$_2$ samples were freshly prepared prior to performing the experiments.

By correlating the degree of accelerated photo-oxidation to the X-ray total dose exposure, and re-passivating the surface, these results may potentially enable a means of realizing quantitative, re-useable QD-based radiation dosimeters.

Time-resolved photoluminescence (TRPL) measurements were also carried out on the CdS/CdTe QD-PSiO$_2$ samples before and after X-ray irradiation and the glutathione treatment, as shown in **Figure 6.8b**. **Table 6.1** lists the average radiative lifetimes for peak QDs emission wavelengths before and after a total exposure dose of 4.4 Mrad(SiO$_2$), and

following the glutathione surface treatment. The decreased lifetime measured after X-ray irradiation is consistent with the CWPL measurements (**Figure 6.8**) and likely results from a combination of increased carrier traps, photoionizations, and multiexciton creation caused by the X-ray irradiation. The increase in carrier lifetime after the glutathione treatment is likely due to a reduction in surface defect states that results from the surface treatment etching away oxide species and partly reforming the CdS shell, as suggested by the XPS (**Figure 6.7**) and CWPL (**Figure 6.8**) data.

Table 6.1* QD PL lifetimes following X-ray irradiations in air

Timeframe	PL Lifetime, τ (ns)
Initial	78 ns ± 5
Post X-ray irradiation	47 ns ± 5
Post-treatment	66 ns ± 5

*Note: The exponential decay rates are the average values obtained from two sets of experiments.

6.4.2 662 KEV Γ-RAY IRRADIATIONS

Higher energy γ-ray irradiation (662 keV, Cesium-137 source) experiments were carried out on the QD-PSiO$_2$ samples in air and nitrogen environments to determine how the different sources of radiation and ambient conditions affect the luminescence properties of the irradiated and glutathione-treated samples. A Cesium-137 source was used for 662 keV γ-irradiation of QD-PSiO$_2$ samples at a dose rate of 0.7 krad/min(SiO$_2$) to a total dose of ~700 krad(SiO$_2$) at room temperature. For some experiments, the samples were sealed in nitrogen purged glass vials prior to being irradiated to minimize the effects of oxygen

and moisture on QD exciton dynamics. The effects of γ-irradiation on the QD-$PSiO_2$ samples in air were similar to those observed for X-ray irradiation (**Figure 6.11 and Table 6.2**).

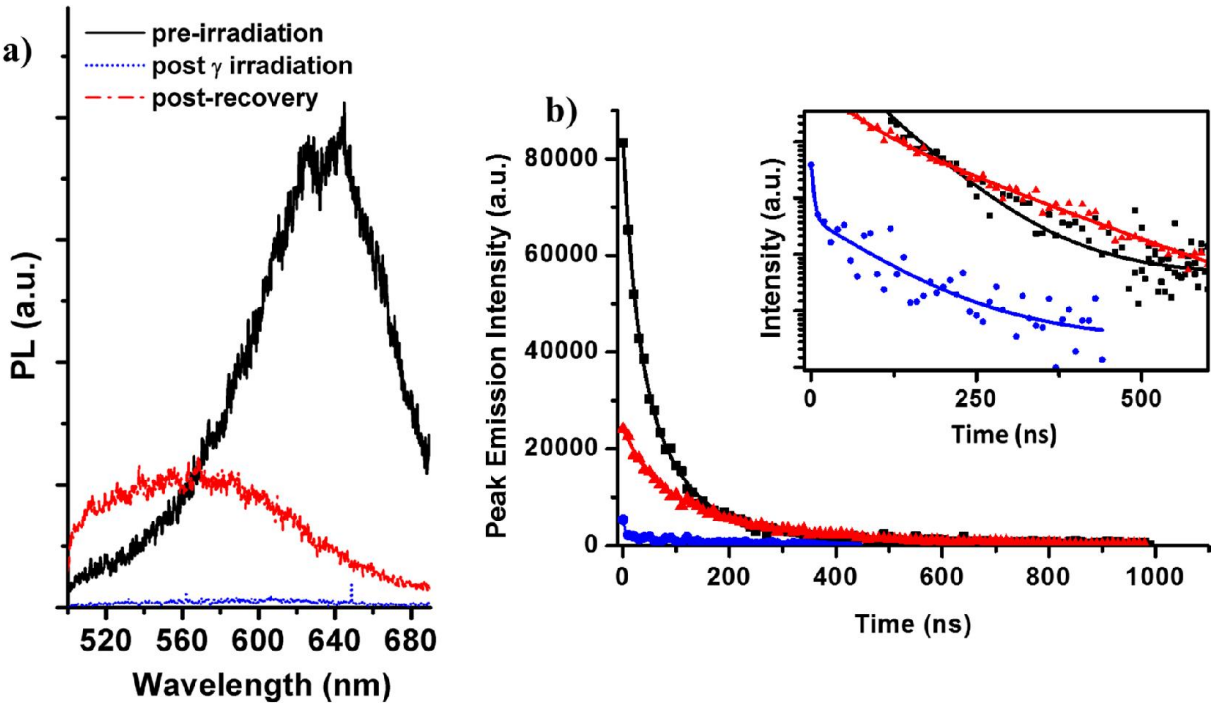

Figure 6.11. a) CWPL measurements of as-prepared sub-monolayer CdTe/CdS QDs immobilized within $PSiO_2$ thin-films (black line), post ~700 krad(SiO_2) γ-irradiation at 0.7 krad/min(SiO_2) in air (blue dotted line), and post surface treatment (red dash-dotted line). b) TRPL measurements of CdTe/CdS QD-$PSiO_2$ samples as-prepared (black squares), post γ-irradiation at 0.7 krad/min(SiO_2) for 17 h in nitrogen (blue circles) and post surface treatment (red triangles). All data points are fit to a bi-exponential decay. The inset shows a zoomed-in plot for the QD carrier lifetime curves. Post-γ irradiation, the bi-exponential fit is clearly evident.

Table 6.2. QD exciton lifetimes post γ-ray irradiations in air.

Initial	~80 ns
Post γ irradiation (Air)	~4 ns + 120 ns
Post-treatment	~53 ns + 216 ns

However, for γ-ray irradiation, a dose of only 700 krad/(SiO_2) was sufficient to cause near complete photodarkening of the samples accompanied by a rapid decrease in lifetime. We note that, due to the lower dose rate of the γ-irradiation (0.7 krad(SiO_2)/min), the total exposure time of the samples to γ-rays as opposed to X-rays was significantly longer. In addition, after the glutathione surface treatment, γ-ray irradiated QD-PSiO_2 samples experienced a significantly higher blue-shift in peak QD emission wavelength compared to X-ray irradiated samples after the same surface treatment procedure, and the surface treatment only partially reversed the γ-radiation induced photodarkening effects (**Figure 6.11**). We attribute the blue-shift in peak QD emission to γ-ray induced photo-oxidation and the subsequent etching of oxide species during the surface treatment. The lack of complete recovery of the QD emission intensity following the surface treatment is likely due to partial or incomplete passivation of the surface dangling bonds after the photocatalytic oxidation of the thiolated ligands, desorption of Cd^{2+} ions or CdTe complexes from the core, and/or permanent lattice displacement damage effects. The minimum energy for lattice displacement damage in bulk CdTe crystals is approximately 250 keV, and the maximum energies of secondary electrons generated by 662 keV γ-rays through Compton scattering is approximately 480 keV.[36,37] Secondary electrons possessing energies higher than 250 keV may therefore cause displacement of atoms in the QD

core/shell structure, resulting in rearrangements in the core-shell QD lattice that may lead to significant loss of QD emission intensities through the creation of several non-radiative mid-gap defect states.

Due to the deeper penetration depth of 662 keV γ-rays into materials, it is also possible to conduct γ-ray irradiation studies on QD-PSiO$_2$ samples enclosed in a nitrogen purged glass vial with a septum. This approach enables suppression of the effects of atmospheric humidity and oxygen on QD surface states that is not possible in the case of low-energy X-rays, which attenuate rapidly in glass such that any sample enclosed in a vial would be shielded from the radiation. CWPL measurements for a QD-PSiO$_2$ sample prior to and following a 700 krad(SiO$_2$) γ-irradiation in a nitrogen environment are shown in **Figure 6.12a**. An 80% decrease in net QD emission results from the γ-irradiation. Following exposure to the thiolated surface treatment solution, the net QD emission increases to 72% of the pre-irradiation value but is not completely reversible. Unlike the X-ray γ-irradiated samples in air, QD-PSiO$_2$ samples irradiated by γ-rays in nitrogen experience no observable blue-shift in the measured QD emission spectra following the glutathione surface treatment, confirming the absence of photo-oxidative effects on the thiolated ligands. Consequently, we conclude that the damage to surface states is lower in the absence of accelerated photo-oxidative effects on the thiolated ligands. The recovery in CWPL observed following exposure to the free-thiol solution (**Figure 6.12**) hints at the possibility of reduction of the Te atoms by the free-thiols. Prior work done by Zhang et. al. also suggests an ability of hydrophilic thiols to passivate surface defect states in addition to reducing Te atoms in the case of photoionization events.[193] From this, we hypothesize

that the main contributing factor towards photodarkening of the QDs under γ-irradiation in purely nitrogen environments is the creation of multi-excitons or dark states that are subsequently reversed post-treatment.

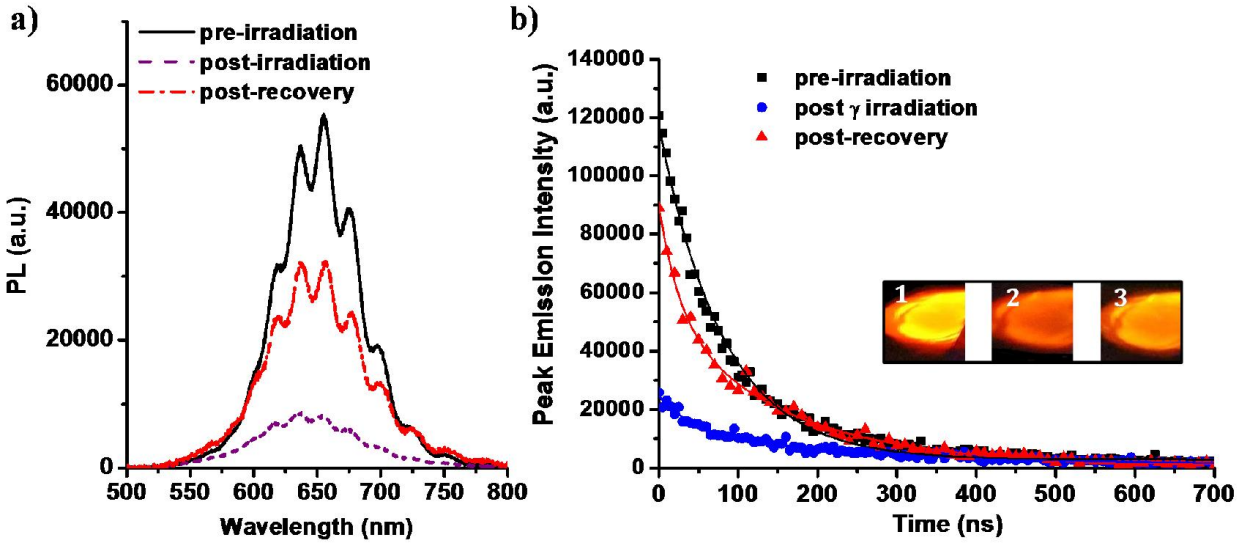

Figure 6.12. a) CWPL measurements of as-prepared sub-monolayer CdTe/CdS QDs immobilized within $PSiO_2$ thin-films (black line), following ~710 krad(SiO_2) γ irradiation at 0.7 krad/min(SiO_2) in a nitrogen environment (blue dotted line), and post glutathione treatment (red dash-dotted line). b) TRPL measurements of CdTe/CdS QD-$PSiO_2$ samples as-prepared (black squares), post γ irradiation at 0.7 krad/min(SiO_2) for 17 h in nitrogen (blue circles) and post glutathione treatment (red triangles). All data points are fit to a bi-exponential decay. Insets show camera images of samples under UV (365 nm) excitation: 1-pre-irradiation, 2-post γ -ray irradiation, and 3-post glutathione treatment.

TRPL measurements for a QD-$PSiO_2$ sample prior to and following a 700 krad(SiO_2) γ-irradiation in a nitrogen environment are shown in **Figure 6.12b**. After prolonged γ-irradiation, the exciton lifetime may be modeled with a bi-exponential fit given by $I(t) = A1 \exp(-t/\tau_1) + A2 \exp(-t/\tau_2)$, where τ_1 and τ_2 represent the time constants, and $A1$

and *A2* represent the amplitudes of the components, respectively (**Table 6.3**).[157] The faster decay time constant τ_1 is usually attributed to exciton recombinations and the much slower decay time constant τ_2 is attributed to emission of dark excitons or other trap states.[198-199] Following γ-irradiation in nitrogen, the faster PL decay component (*A1%*) is seen to decrease accompanied by faster carrier recombination times, possibly due to increased defects. The longer PL component (*A2%*) is seen to significantly increase accompanied by a lengthening of the PL decay time following irradiation. This may result from carrier trapping. After the glutathione surface treatment, there is an overall decrease in both PL decay times.

Table 6.3. QD PL lifetime post γ-ray irradiations in nitrogen

Timeframe	*A1*%	τ_1 (ns)	*A2*%	τ_2 (ns)
Initial	79.87%	57 ± 5	20.13%	220 ± 15
Post γ irradiation (N_2)	46.56%	43 ± 5	53.44%	273 ± 7
Post-treatment	40.51%	25 ± 5	59.49%	151 ± 15

6.5 Conclusions

The effects of X-ray and γ-ray irradiation on the photophysical properties of colloidal CdTe/CdS QDs immobilized within $PSiO_2$ 3D scaffolds have been characterized. The QD emission is significantly reduced following irradiation. XPS measurements confirm photo-oxidation plays a role when irradiation is performed in air. Photoionization, carrier traps, and multiexciton generation also likely play a role in the radiation-induced photodarkening and reduced exciton lifetimes that were measured following X-ray and γ-ray irradiation of the QD-$PSiO_2$ samples. More detailed investigations of QD exciton

dynamics that can resolve sub-nanosecond lifetimes would be able to shed further light on competing mechanisms of photo-oxidation, long lived carrier traps, and mid-gap defect states. Due to their higher energy, γ-rays also likely cause lattice displacements in the QDs that lead to a permanent reduction in the QD emission. CdTe/CdS QDs demonstrate near complete recovery of QD peak intensity and lifetime after X-ray irradiation when a thiol-rich surface treatment procedure is performed; partial luminescence recovery was observed for γ-irradiated samples. We believe the surface treatment is instrumental in not only reforming a CdS shell but also reducing photoionized QDs that have entered into a dark state. Quantification of the total exposure dose through monitoring changes in QD peak emission intensity and energy may enable applications in passive radiation dosimetry in high risk, high radiation environments. Lightweight and flexible QD-based thin film substrates could be realized for a variety of applications with sub-monolayer QD distributions in $PSiO_2$ 3D scaffolds that reduce carrier-trapping and charge transfer between QDs and maintain access to QDs surfaces for re-passivating solutions.

7. CONCLUSIONS AND FUTURE WORK

7.1 Conclusions and Research Contributions

In summary, novel optical sensors for point-of-care diagnostics and high energy radiation environments have been explored. By combining two unique material systems, namely porous silicon and quantum dots, we demonstrate improved performance metrics for small molecule optical sensors and provided an alternative approach towards realizing all-optical, low-cost, large area radiation dosimeters.

Chapter 1 serves as an introduction to the concepts, ideas, devices, and applications that have been developed and demonstrated in this dissertation as well as provides a backdrop to the motivations behind the research conduct.

Chapter 2 provides a detailed and thorough analysis of the PSi material system that serves as a backbone for developing all of the applications, and devices covered in the following chapters of the dissertation. Due to the detailed PSi characterizations undertaken in this Chapter, it is possible to better estimate the target size range for possible small molecule and QD infiltration, and thereby quantify the capture of target small molecules and quantum dots within the porous scaffold. This allows for careful sensor design and optimization to achieve the best possible sensing metrics for biosensor development and high energy radiation dosimetry.

Chapter 3 delves into the conceptual development of thin-film reflectance interferometers and demonstrates their practicality as a low-cost, highly sensitive, robust means of target analyte detection using QD-labeled, dual-mode optical sensing. The QDs have been

demonstrated to function as refractive index signal amplifiers as well as target specific fluorescence biomarkers. QD-labeled detection of a 1 nm sized small molecule, biotin, was achieved with over two orders of magnitude improved detection sensitivity. This project has the potential for further developments to make it more aligned with smartphone compatible detection methods as outlined in the following **Chapter 4** and the future research opportunities **Section 7.2**.

Chapter 4 demonstrates the design and simulation results for two resonant optical cavity structures that are capable of low-cost, portable, and highly sensitive target molecule capture. The PSi μC-HCG and the PSi-ABR, both support optical monitoring of target molecule capture, free of any complex coupling optics, through the detection of refractive index changes upon the capture of target molecules that are translatable through shifts in their respective resonance wavelengths. A straightforward detection scheme that is compatible with smartphone cameras in the reflectance mode requires the use of either a broadband light source or low cost excitation LED for the PSi μC-HCG or the PSi-ABR respectively.

Chapter 5 investigates the influence of interfacial oxide thickness, on the optical properties of monolayer QDs, when immobilized in 3D PSi scaffolds. An exponential dependence of QD carrier lifetime on the interfacial oxide thickness was found to be strongly indicative of charge transfer exciton dynamics. The fundamental analysis of QD exciton lifetimes and CWPL intensities when integrated with complex heterostructures provides important insight into the influence of electron wavefunction overlap with neighboring defect states and disordered energy levels. This work has the potential of contributing to an improved

understanding of the electrical and optical properties of QDs when integrated with PSi structures for applications in photovoltaics and energy storage.

Chapter 6 investigates the influence of X-ray and gamma-ray (γ-ray) irradiation on the photophysical properties of sub-monolayer CdTe/CdS quantum dots (QDs) immobilized in porous silica ($PSiO_2$) scaffolds. The highly luminescent QD-$PSiO_2$ thin films allow for straightforward monitoring of the optical properties of the QDs through continuous wave and time-resolved photoluminescence spectroscopy. The $PSiO_2$ host matrix itself does not modify the QD properties. X-ray irradiation of the QD-$PSiO_2$ films in air leads to an exponential decrease in QD emission intensity, an exponential blue-shift in peak emission energy, and substantially faster exciton decay rates with increasing exposure doses from 2.2 Mrad(SiO_2) to 6.6 Mrad(SiO_2). γ-ray irradiation of a QD-$PSiO_2$ thin film at a total exposure dose of 700 krad(SiO_2) in a nitrogen environment results in over 80% QD photodarkening but no concurrent blue-shift in peak emission energy due to a lack of photo-oxidative effects. Near-complete and partial reversal of irradiation-induced photodarkening was demonstrated on X-ray and γ-ray irradiated samples, respectively, through the use of a QD surface ligand, re-passivating solution, suggesting that there are different contributing mechanisms responsible for photodarkening under different irradiation energies. This work contributes to improving the reliability and robustness of QD based heterogeneous devices that are exposed to high risk, high energy radiation environments, with the possibility of also developing QD-based large area, low-cost, re-useable, and flexible optical dosimeters.

7.2 Future Research Opportunities

7.2.1 Enhanced Light Matter Interactions

Further design parameter optimizations of the PSi μC-HCG and the PSi-ABR sensors are capable of achieving higher field confinements within active sensing regions. The PSi μC-HCG demonstrated in **Chapter 4** is polarization dependent. A 2D HCG may be designed and optimized to be polarization independent and then integrated with a PSi Bragg stack to achieve a narrow linewidth resonance at designed wavelengths. More rigorous optimizations of the ABR based on parameter sweeps, have demonstrated Q-values as high as $1x10^6$, which are on-par with those achievable by 2D PhCs.[39] Preliminary work on the integration of CdTe/CdS QDs with PSi μCs demonstrated an over 2 fold enhancement of QD PL intensities at the μC resonance wavelength (**Figure 7.1**). The design criteria for these μCs has been outlined earlier in **Chapter 1, Figure 1.11**. The peak QD emission wavelength for the CdTe/CdS QDs in solution is ~640 nm. The attachment of QDs in the μCs is carried out as per the same procedure described in **Chapter 5** using electrostatic attachment of QDs to a PDDA functionalized PSi surface. The simulated and experimental Q factors for the PSi μC were 450 and 150 respectively. Taking into consideration improved QD infiltration efficiencies and higher Q factors for the deigned μCs-HCGs and ABRs, the enhancements in QD PL intensities at cavity resonance wavelengths is expected to be much higher.

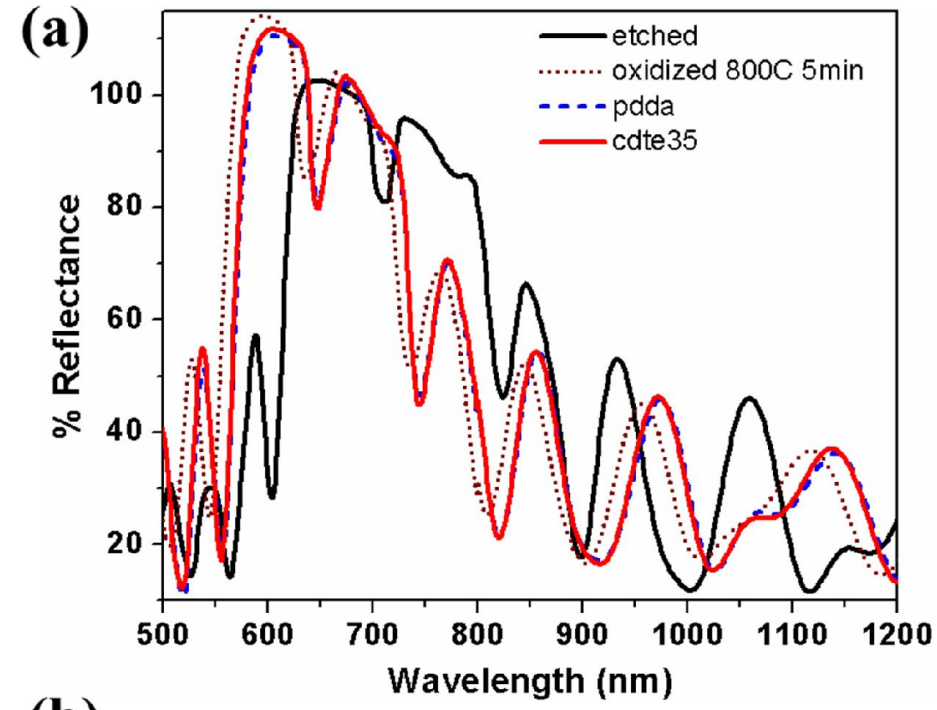
(a)
etched
oxidized 800C 5min
pdda
cdte35
% Reflectance
100
80
60
40
20
500
600
700
800
900
1000
1100
1200
Wavelength (nm)

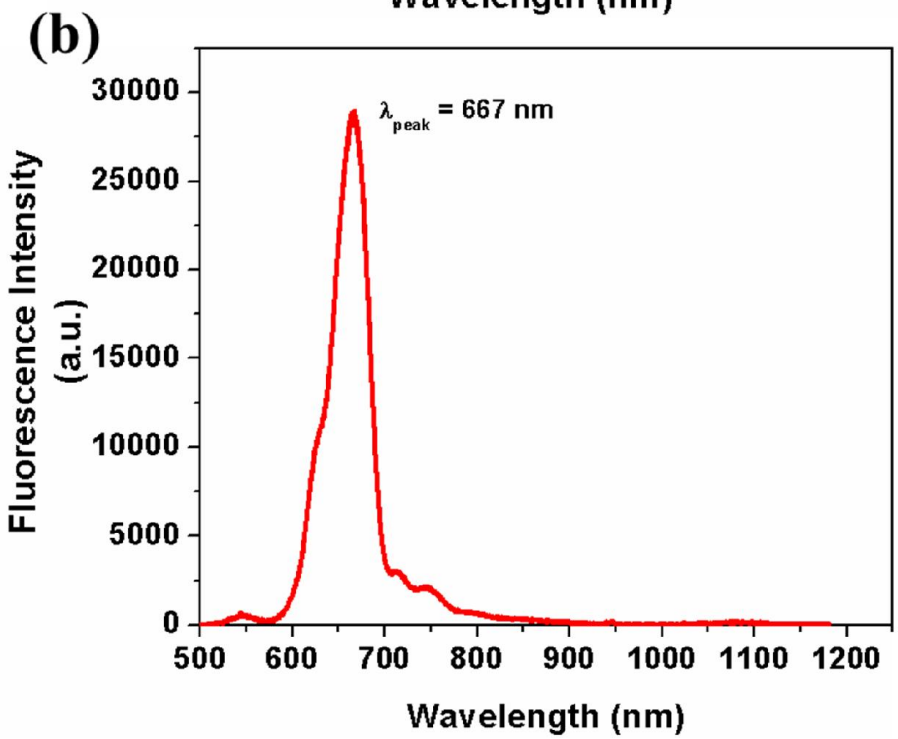
(b)
λpeak = 667 nm
Fluorescence Intensity (a.u.)
30000
25000
20000
15000
10000
5000
0
500
600
700
800
900
1000
1100
1200
Wavelength (nm)

Figure 7.1. a) Experimentally measured reflectance spectra for a PSi μC for successive surface functionalization steps and attachment with CdTe/CdS QDs. b) Measured QD PL spectra from the PSi μC under 488 nm laser excitation.

The experimental realization of the optical resonators with enhanced light-matter interactions, can help demonstrate detection sensitivity improvements for sub-nM target analytes, with μL analyte volumes, in a straightforward detection schemes. The opto-fluidic integration of the resonators can additionally provide real-time binding kinetics while ensuring the delivery of target molecules to the active sensing regions. As a result, the PSi μC-HCGs and PSi-ABRs are sensing platforms that are capable of contributing towards the implementation of robust, and portable, point-of-care diagnostics.

7.2.2 QD Based Optical Radiation Dosimeters

Further studies exploring the use of QDs as radiation dosimeters could provide more detailed response curves of changes in QD PL versus total absorbed dose. Additionally, the influence of high energy charged particles such as protons is expected to result in new findings. If studies were able to differentiate the impact of different sources of radiation based on the optical response of QDs, it would provide an exciting alternative to currently used space radiation dosimeters such as TLDs and SSNTDs.

Another alternative research direction is the integration of QDs into nuclear containment facility structures. Stress or strain related cracks or other structural defects will expose the QDs contained within such structural materials to high energy radiation and atmospheric influences, thereby significantly altering their optical properties. Routine inspections of such facilities by a straight-forward, low cost, optical detection scheme can

then reveal the formation of structural cracks due to the distinct changes in the optical properties of the exposed QDs. This method has the potential to detect cracks and other structural deformations, and save lives, in high-risk, radiation environments, in a timely and highly sensitive manner, with remote sensing capabilities.

MATLAB CODES

```
%Determining Pore Size in Pixels
%Girija 2010

file = 'p60(3)_b.tif'; %filename
x = LoadTif(file);

y = gt(x,55);        %user-defined thresholding value (depends upon image brightness etc)

% y=bwmorph(y,'clean');%performs removal of isolated pixels from image.
% y=bwmorph(y,'spur');%performs removal of end points from image.
%imshow (y)
 y = 1-y;

%hold on;
%imshow (y)

%L = medfilt2(y,[3 3]);

for i = 1:829
   for j = 1:552
      new(j,i)=y(j,i);
   end
end

figure;
imshow (new)
hold on;

label = bwlabel (new);
stats = regionprops (label, new, 'Area');
idx = find([stats.Area] > 140); %Ignoring stray pixel noise and finding pixel areas greater than 10 or user-defined
L2 = ismember(label,idx);

label2 = bwlabel (L2);
stats2 = regionprops (label2, L2, 'Area');

idx2 = find([stats.Area] < 1000);
L3 = ismember (label,idx2);

areas = [stats2.Area];
pores = size (areas);
diam = 2*(sqrt(areas/3.14));

diam_nm = diam.*1.2; %conversion factor using Image J depending upon image scale bar
```

```
%y = hist(diam_nm,46);
%hist(diam_nm,8)
%figure(gcf); %80 bins for 55% porosity
sum = 0;
for i = 1 : pores(2)
   sum = sum + diam_nm(i);
end
%sum
avgporesize = sum/pores(2) %outputs the average pore size for PSi image
```

Function Called:
LoadTif

```
function x = LoadTif(fileName)

x= imread(fileName,'tif');
x = double(x);



% Surface area coverage
% Girija

%number of pores = n;
clc;
pi = 3.14;
r_etch = 0.75E-2; %m  sample is 1.5cm in diameter
%h = 2.0E-6; %sample thickness in nm
h = 9000E-9; %sample thickness in nm
r_qd = 2E-9; %nm or 3.75nm/1.4nm
r_pore = 6.0E-9; %nm of one pore
p = 0.30; %porosity

vol_pore = pi*r_pore^2*h;
vol_etch = pi*r_etch^2*h;

%p = (n*vol_pore)/ vol_etch;

n = (p*vol_etch)/vol_pore

%volume of pores in m3
%V_pores = p*vol_etch;
V_pores = n*vol_pore;
%fillfactor as determined using EMA

%ff = 0.05; %for PbS14 in small pores
number_qds = 1.0067e+14; %

surface_area_qds = number_qds*pi*r_qd.^2   %m2
```

```
%number_pores = (p*0.525*pi)/(pi*r_pore^2)
total_sa = n*(2*pi*r_pore*h)

percent_SA = (surface_area_qds/total_sa)*100


% Bruggeman's EMA:
clc;
clear all;
x = 1:0.001:4;

n1 = 1.00 %refractive index of pores (host material)
n2 = 3.45; %refractive index of Silicon (filling material)
p = 0.73; % porosity or volume fraction of host material

y = (p)*((n2^2)+ 2*(x.^2)).*((n1^2)-(x.^2)) + (1-p)*((n2^2)-(x.^2)).*((n1^2)+2*(x.^2));

y0 = zeros(1,length(x));

plot(x,y,x,y0);

% zero crossing point or effective index
for i = 1:3000
   if y(i) <0.02
      if y(i) > -0.015
      neff = x(i);
      end
   end
end
neff


 % Oblique incidence on a layered structure, incidence in air and %silicon substrate
% Transfer Matrix Code
% Girija 2/26/2013

clc;
clear all;

mode = 'TE';          % TE or TM simulation
c = 2.99792458E+8;     % m/s speed of light in vacuum
mp0 = 4*pi*10^-7;      % H/m magnetic permeability constant
ep0 = 8.854187817E-12;  % F/m vacuum permittivity or epsilon
h = 6.626068E-34;      % m2.kg/s Planck's constant
e = 1.6E-19;          % C electron charge

% Define experimental parameters
n_inc = 1;             % air
n_sub = 1;            % index of refraction of silicon substrate
```

```
thetai = 0;             % angle of incidence of white light
theta_I_deg = 0;
theta_I = theta_I_deg/180*pi;  % angle of incidence in radians
lambdas = 300:1:2000;    % wavelength range of interest in nm
k0 = 2*pi./(lambdas.*1E-9);       % wave vector in air
w0 = k0.*c;             % angular freq.

% Define structure to be simulated
S1 = 2;               % number of periods in 1st Bragg mirror
S2 = 3;               % number of periods in 2nd Bragg mirror
S = S1 + S2;
np1 = [3.45 1];      % refractive indices of periodic layers in 1st Bragg mirror
np2 = [1 3.45];      % refractive indices of periodic layers in 2nd Bragg mirror

npp1 = repmat(np1,[1 S1]); % n in 1st Bragg
npp2 = repmat(np2,[1 S2]); % n in 2nd Bragg

nm = [npp1, npp2];         % refractive indices string for entire microcavity

% n1 = 1.5;
% n2 = 1.8;
% nm = [n1 n2 n1 n2 n1 n2];
 N=length(nm); %N is the number of layers

d1 = [150e-9 185e-9];
d2 = [185e-9 150e-9];
dpp1 = repmat(d1,[1 S1]);
dpp2 = repmat(d2,[1 S2]);
d = [dpp1 dpp2];

% d1 = 1*1E-6;
% d2 = 2*1E-6;
% d = [d1 d2 d1 d2 d1 d2];
theta=zeros(N);
theta_0 = asin((n_inc*sin(theta_I))/nm(1)); % From Snell's Law

theta(1) = asin((nm(1)*sin(theta_0))/nm(2)); % From Snell's Law, theta(1)=theta0
kx(1,:)=k0.*nm(1).*cos(theta(1));
phi(1,:)=kx(1,:).*d(1);
       for a=2:N
        theta(a) = asin((nm(a-1)*sin(theta(a-1)))/nm(a)); % From Snell's Law, theta(1)=theta0
        kx(a,:)=k0.*nm(a).*cos(theta(a));
        phi(a,:)=kx(a,:).*d(a);
       end

%theta_sub = asin((nm(N)*sin(theta(N)))/n_sub); % From Snell's Law

tp1 = [200*1E-9 400*1E-9];
tp2 = [400*1E-9 200*1E-9];
% ******************************
```

```
% Calculate relative permittivities
e_r=nm.^2;

e_rinc = n_inc.^2;
e_rsub = n_sub.^2;


L = [5e-6 d 5e-6];
n = [n_inc nm n_sub];
Tlength = sum(L);
zz=[];
for a = 1:length(L)
   zz = [zz sum(L(1:a))];
end
zz = [0 zz];
nzz = [n n(length(n))];
subplot(3,1,1);
hold on
stairs(zz,nzz,'k');
xlabel('Depth (nm)','fontsize',10)
ylabel('Index','fontsize',10)
axis([0 Tlength 1 4])

%**************************
switch mode
      case {'TE'}
      D0 = [1,1;n_inc*cos(theta_I),-n_inc*cos(theta_I)];
      D0_i = inv(D0);
      D1 = [1,1;nm(1)*cos(theta(2)),-nm(1)*cos(theta(2))];
      D1_i = inv(D1);
      P1 = [0,0;0,0];
      M = [0,0;0,0];

      theta_sub = asin((nm(N)*sin(theta(N)))/n_sub);
      Ds = [1,1;n_sub*cos(theta_sub),-n_sub*cos(theta_sub)];

       for ii = 1:length(lambdas)

            P1 = [exp(1i*phi(1,ii)),0;0,exp(-1i*phi(1,ii))]; % Propagation matrix medium 1
            MM = D1*P1*D1_i;


        for a=2:N-1
      MM_bk=MM;
      D = [1,1;nm(a)*cos(theta(a+1)),-1*nm(a)*cos(theta(a+1))];
      D_i = inv(D);

      P(:,:)   = [exp(1i*phi(a,ii)),0;0,exp(-1i*phi(a,ii))]; %

      MM = D*P(:,:)*D_i*MM_bk;
```

```
        end
       M(:,:) = D0_i*MM*Ds;
        R(ii) = 100*abs(M(2,1)./M(1,1)).^2;
        t(ii)  = 1/M(1,1);
        T(ii) = 100*(abs(t(ii)).^2).*((n_sub.*cos(theta_sub))./(n_inc.*cos(theta_I)));

       end

       case {'TM'}
       D0 = [cos(theta_I),cos(theta_I);n_inc,-n_inc];
       D0_i = inv(D0);
       D1 = [cos(theta1),cos(theta1);n1,-n1];
       D1_i = inv(D1);
       D2 = [cos(theta2),cos(theta2);n2,-n2];
       D2_i = inv(D2);
       Ds = [cos(theta_sub),cos(theta_sub);n_sub,-n_sub];
end

P1 = [0,0;0,0]; P2 = [0,0;0,0]; M = [0,0;0,0];
for iii=1:N

end
    RR = R';
    TT = T';
% M = D0_i*(D1*P1.*D1_i*D2*P2.*D2_i).^length(n)*Ds;

subplot(3,1,2)
hold on
plot(lambdas, RR,'b')
xlabel('Wavelength (nm)','fontsize',12)
ylabel('% Reflectance','fontsize',12)
xlim([min(lambdas) max(lambdas)])
subplot(3,1,3)
hold on
plot(lambdas, TT,'b')
xlabel('Wavelength (nm)','fontsize',12)
ylabel('% Transmittance','fontsize',12)
xlim([min(lambdas) max(lambdas)])
```

APPENDIX A

RADIATION EFFECTS ON QD-PSI SUBSTRATES WITH SUB-NM INTERFACIAL OXIDE

The effects of X-ray and gamma irradiation on the optical properties of CdTe/CdS quantum dots (QDs) immobilized in a functionalized porous silicon film have been investigated via continuous wave and time-resolved photoluminescence measurements. Carrier lifetimes of the QDs and photoluminescence intensities decrease with increasing exposure dose from 500 krad(SiO_2) to 16 Mrad(SiO_2).

Figure A1 shows the CWPL spectra for PDDA functionalized PSi before and after immobilization of QDs (no irradiation). As reported previously, the distinct fringes present in the QD fluorescence spectrum confirm QD infiltration and immobilization throughout the PSi layer.[197]

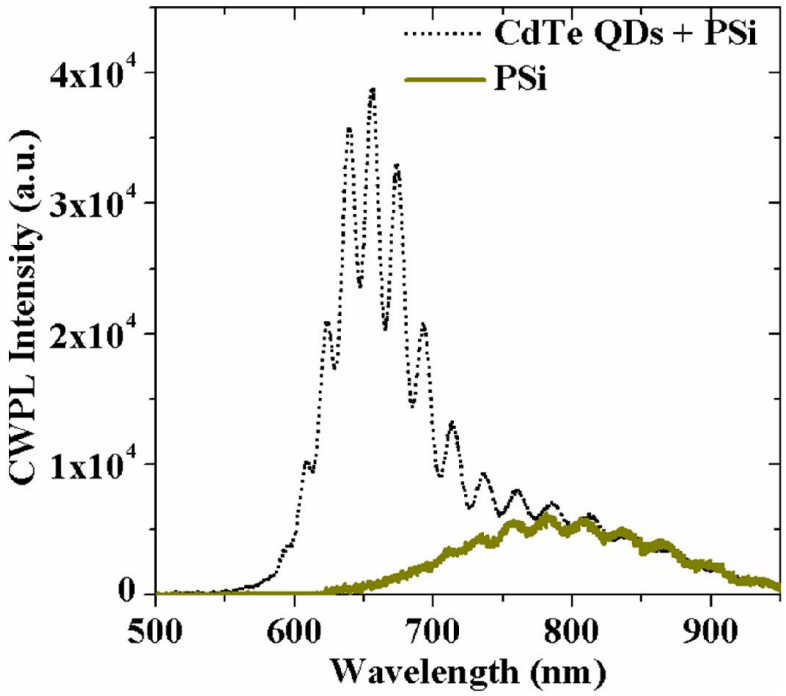

Figure A1. CWPL spectra for PDDA functionalized PSi before (solid line) and after (dotted line) immobilization of CdTe QDs.

PSi-QD samples were irradiated with 10 keV X-rays at a dose rate of 31.5 krad/min(SiO_2) in an ARACOR 4100 X-ray irradiator for exposure times varying from about 15 min to 8.5 h in an ambient environment. The measured CWPL spectra are shown in **Figure A2a**. With each successive exposure dose, the QDs darken further with almost complete loss of measureable fluorescence intensity at irradiation doses above 4 Mrad(SiO_2). We observe no blue-shift in the collected PL spectra, possibly suggesting well-passivated QD surface states in the CdS shell that are not prone to further oxidation. X-ray irradiation effects on the CWPL intensities of PSi are much less pronounced with only a slight decrease noted over the 600 nm to 900 nm wavelengths as seen from **Figure A2a**. The corresponding CWPL measurements made on the control sample stored in ambient environment, over the

same time duration, are shown in **Figure A2b**. The QD fluorescence of the control sample remains nearly constant for the first 127 min before decreasing by ~25% during the subsequent 381 min.

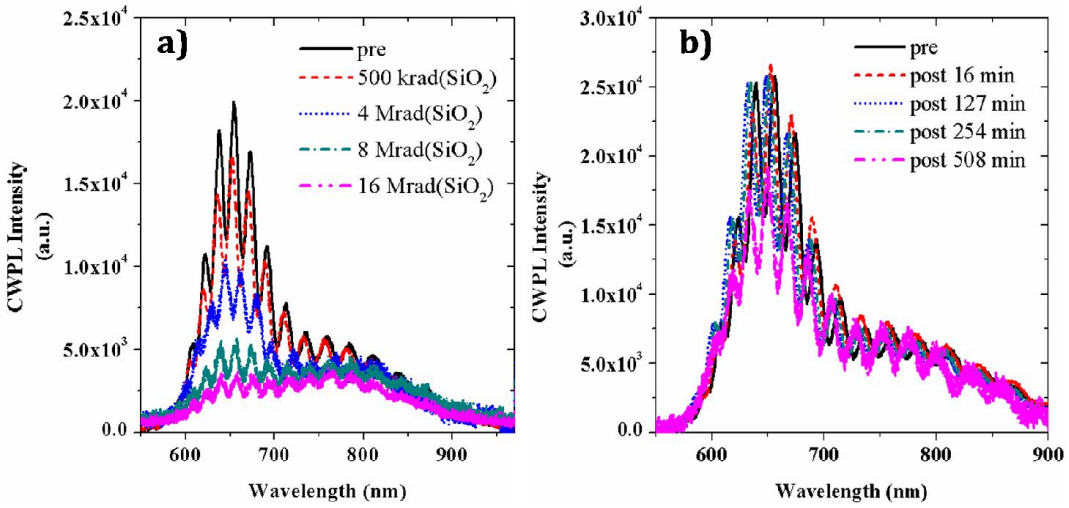

Figure A2. CWPL spectra of PSi-QD samples. a) QD fluorescence of the irradiated sample before X-ray irradiation (pre), followed by total exposure doses of 500 krad(SiO_2), 4 Mrad(SiO_2), 8 Mrad(SiO_2) and 16 Mrad(SiO_2). The QD peak fluorescence intensity decreases with X-ray irradiation total dose. b) Control experiment carried out for same time durations as the irradiations in (a) but the PSi-QD control sample was maintained in ambient environment without X-ray irradiation.

The effect of X-rays on irradiated materials is primarily classified as a point interaction with the creation of several secondary electron-hole pairs. The number of such secondary particles generated can be estimated from the average energy necessary to create an electron-hole pair, which is approximately 4.4 eV for cubic CdTe QDs.[200] The ejection of

an electron from the QD core will result in ionization and non-radiative Auger processes that occur on much faster time scales than radiative processes, and will initiate a dark state in the QD.[201] As a result, even in the event of absorption of a photon, an excited electron will not decay radiatively to the ground state and instead will transfer the acquired energy to a coupled hole through Coulombic interactions which may then rapidly relax through valence band states.[202] **Figure A3** shows the QD fluorescence lifetime decay before and after 5.4 Mrad(SiO_2) X-ray irradiation at 36.7 krad/min(SiO_2) (**Figure A3a**). The time-resolved photoluminescence (TRPL) intensity of a control sample measured before and after a time duration equivalent to that of the irradiation experiment is shown in **Figure A3b**. The curves shown in the figure are single exponential fits to the measured data. The control sample exhibits almost no change in QD decay time over the measurement period.

Taking into consideration the photo-physical effects of the surrounding substrate, we believe that ejected electrons from the QDs will become permanently trapped in substrate defect states or will recombine with holes present in the positively charged PDDA monolayer. Further studies are necessary to determine whether secondary electrons created in neighboring QDs or the PSi substrate can neutralize ionized QDs and reverse irradiation induced fluorescence quenching or, alternatively, contribute to the enhancement of photo-ionization by imparting some of their energy to excited electrons in bright QDs resulting in the ejection of electrons. The progressive loss of QD fluorescence, however, suggests an overall effect in which an increasing number of QDs are being photo-ionized, and thereby unable to function as electron-hole recombination centers. Additionally, irradiation

induced surface transformations and rearrangements of capping agents on the QDs[203] will also contribute to loss of exciton formation due to electrons being localized in deep traps in the CdS shell or near the QD surface for extended periods of time.[204] Therefore, the observed decrease in QD fluorescence lifetime of approximately 70% (**Figure A3a**) is attributed to a combination of reduced exciton formation, and increased non-radiative recombination processes arising from the creation of mid-gap defect states in the QD and surface capping agents upon continuous X-ray irradiation.

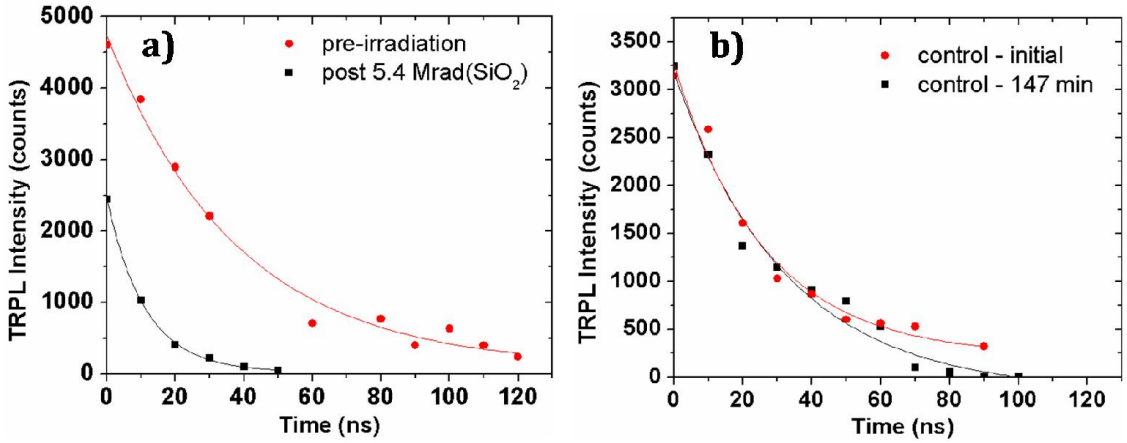

Figure A3. TRPL measured at an emission energy of 1.9 eV, showing QD fluorescence lifetime decay. a) Measurements of a PSi-QD sample pre- and post-irradiation at 5.4 Mrad(SiO_2) demonstrate a decrease in lifetime from 37 ns to 11 ns ± 4 ns. b) The control sample exhibits a slight decrease in lifetime from 32 ns to 28 ns ± 4 ns after 147 min, a time duration equivalent to the irradiation experiment, compared to an initial measurement.

Camera images of PSi-QD samples shown in **Figure A4** clearly demonstrate X-ray irradiation induced QD fluorescence darkening. **Figure A4a** shows the samples under UV excitation pre-irradiation. Significant darkening is observed on sample 1 irradiated with 5.4 Mrad(SiO_2), while the control sample 2 without irradiation shows only a slight decrease in QD fluorescence intensity after a 147 min time duration equivalent to the time taken to irradiate sample 1.

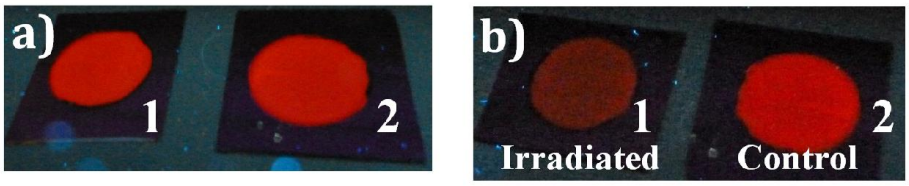

Figure A4. Camera images for PSi-QD samples under UV lamp (365 nm) excitation. a) Images taken pre-irradiation. b) Images taken after 5.4 Mrad(SiO_2) X-ray irradiation for sample 1 and after an equivalent time (147 min) for control sample 2 maintained in ambient conditions with no irradiation.

Similar to the effects observed for PSi-QD samples exposed to X-ray irradiation, QD darkening and a reduction in QD fluorescence lifetime were experimentally observed for QDs attached in a PSi matrix after γ irradiation. However, the significantly higher energy γ rays from a Cesium-137 source are expected to result in the creation of secondary electrons that possess sufficiently high energies to cause lattice displacement damage. Secondary electrons will interact with electron clouds of atoms in their path through Coulomb scattering and can lose a large fraction of their energy in a single interaction as

well as get deflected through large angles. The minimum energy for lattice displacement damage in bulk CdTe crystals is approximately 250 keV.[205] Secondary electrons possessing energies higher than 250 keV may therefore cause displacement of atoms in the QD core/shell structure, resulting in rearrangements in the core-shell QD lattice, eventually leading to complete loss of QD fluorescence through the creation of several non-radiative mid-gap defect states. Further studies are warranted for estimating the energy level distributions of the defects.

Due to the deeper penetration of 662 keV γ rays into materials, it is possible to expose PSi-QD samples enclosed in a nitrogen purged glass vial with a septum to γ ray irradiation, thereby suppressing the effects of atmospheric humidity and oxygen on the creation of additional surface defect states. Images of PSi-QD samples were taken under UV excitation prior to (**Figure A5a**) and after conducting γ ray irradiation on sample 1 (**Figure A5b**). Sample 2 served as the control and was also maintained in a nitrogen environment. Over a total time duration of the experiment of approximately 16 hrs, QDs immobilized in the control sample darken with an approximately 27% decrease in CWPL peak intensity while the irradiated sample exhibits significantly higher QD degradation with over 90% loss of CWPL peak intensities.

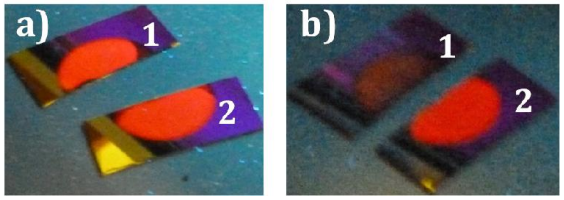

Figure A5. Camera images of PSi-QD samples under UV lamp (365 nm) excitation. a) Freshly prepared samples showing strong QD fluorescence. b) Sample 1 after exposure to 1.04 Mrad(SiO_2) γ irradiation at 1.1 krad/min(SiO_2) in nitrogen atmosphere demonstrating radiation induced fluorescence quenching and sample 2, as a control also stored in nitrogen atmosphere, showing a slight decrease in fluorescence over the same time duration.

TRPL measurements taken on these two samples, as shown in **Figure A6**, indicate that γ irradiation leads to a decreased PL lifetime from 44 ns for control sample 2 in nitrogen to ~26 ns for sample 1 irradiated for a total dose of 1.04 Mrad(SiO_2) in a nitrogen environment.

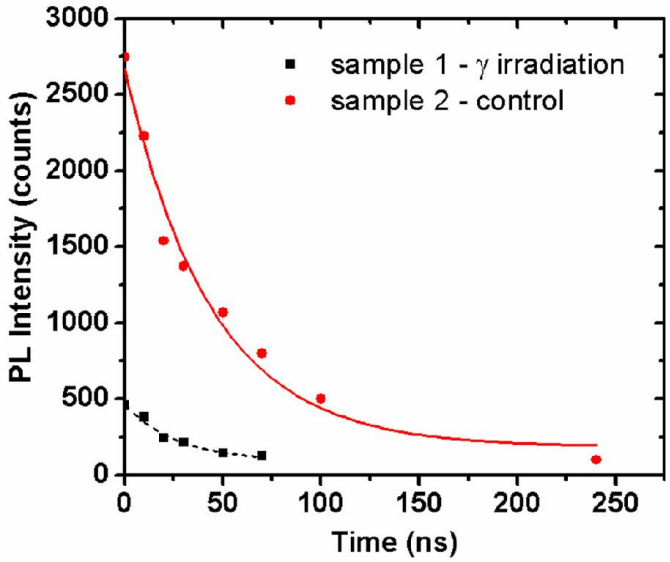

Figure A6. TRPL measurements comparing QD fluorescence lifetime decays for γ irradiated sample 1 and control sample 2 at an emission energy of 1.9 eV. Both

measurements were taken after the same time duration with only sample 1 exposed to a total dose of 1.04 Mrad(SiO_2) in a nitrogen environment. The lines are single exponential fits to the data.

Similar experiments carried out under ambient conditions demonstrated complete darkening of all the QDs immobilized in PSi when exposed to 1 Mrad(SiO_2) total dose under γ irradiation. The control sample exhibited an approximately 50% decrease in peak CWPL intensities over the same time duration. These results suggest that the presence of oxygen and moisture play a significant role in the degradation of QDs immobilized on a solid substrate. The optical properties of QDs are altered due to irradiation induced photo-ionization, creation of mid-gap defect states with strong electron-phonon couplings that reduce the decay time of internal relaxations, transformations and defects in the capping agents that affect the rate of interfacial relaxations as well as lattice displacement damage that may create several mid-gap defect states with a decrease in the quantum confinement of electron-hole wave functions and increased overlap with surface states and substrate defects.

CONCLUSION

The effects of X-ray and γ ray irradiation on the optical properties of colloidal CdTe QDs immobilized in a surface functionalized PSi film have been investigated. Quenching of QD CWPL was observed with increasing X-ray exposure dose with no blue-shift towards shorter wavelengths. In order to further investigate the effects of significantly higher energy γ rays, PSi-QD films were subjected to γ irradiation in ambient and nitrogen environments that helped to probe the influence of ambient moisture and oxygen on QD

darkening. γ irradiation led to stronger fluorescence quenching of the QDs with a 40% reduction in the carrier lifetime for a 1 Mrad(SiO_2) total dose and almost complete quenching of the QD CWPL under nitrogen, and complete loss of QD fluorescence for similar experiments conducted in air. In addition to ionization of QDs, secondary electrons generated due to the higher energy γ rays can lead to displacement damage. This study enables a better understanding of the interaction of high-energy radiation with a composite semiconductor QD-PSi system with applicability for improving potential QD-based device reliability such as in solar cells and LEDs in high-dose radiation environments.

APPENDIX B

INTERFACIAL OXIDE GROWTH IN PSI UNDER THERMAL OXIDATION

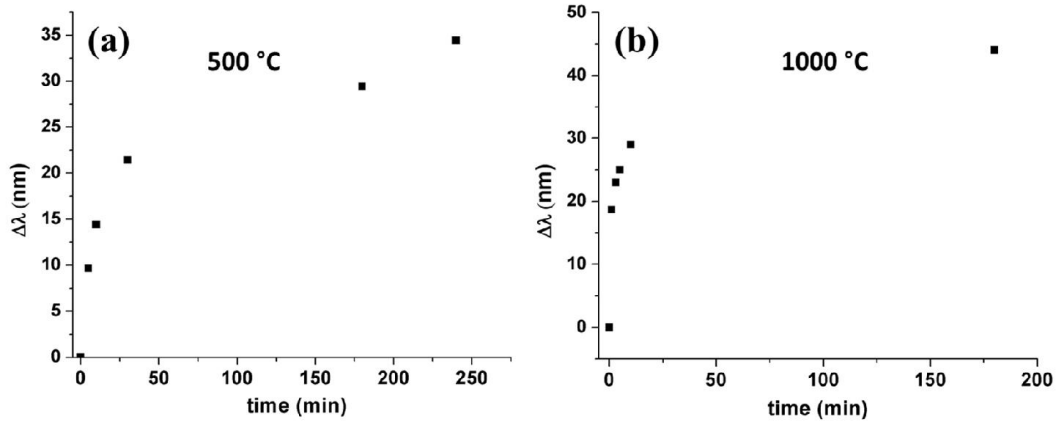

Figure B1. Shifts in reflectance spectra recorded near 1000 nm for different thermal oxidation conditions in air. a) 500 °C oxidation b) 1000 °C oxidation.

Influence of increasing thermal oxidations at 500 °C and 1000 °C on the reflectance fringe peak positions near 1000 nm, for 10 μm PSi samples, etched at 48 mA/cm^2 for 667 s. Δλ refers to the extent of blue-shift in the fringe peak position near 1000 nm.

APPENDIX C

LUMERICAL SIMULATION METHODS

The method to estimate field enhancements in Lumerical:

Do not apply any apodization. This will give the correct field amplitude which includes the sources in the field profile which is returned. The enhancement of the field amplitude due to the cavity, can then be calculated by running the simulation with the cavity and runing another reference simulation with just the source and no cavity or structure, and dividing the field results from the simulation with the cavity by the reference to get the enhancement factor.

Purcell Factor estimations using Lumerical:

The Purcell factor is the emission rate enhancement of a spontaneous emitter inside a cavity or resonator. Dipoles in FDTD Solutions automatically return the Purcell factor as a result that may be directly visualized or accessed from the Result View window after a simulation is run.

The Purcell factor result is equivalent to dividing the power emitted by a dipole source in the environment by the power emitted by the dipole in a homogeneous environment (bulk material) since the emission rate is proportional to the local density of optical states(LDOS), and the LDOS is proportional to the power emitted by the source. Note that only one simulation with one dipole orientation is used to determine the Purcell factor since

this orientation results in the maximum Purcell factor, and the maximum Purcell factor is what is being analyzed. In the case where Purcell factor of an isotropic emitter is required, the results from three orthogonal dipole orientations may be averaged.

A more specific procedure is outlined as below:

The Purcell factor depends on location and frequency so the first run is a preliminary simulation that uses a broadband source to determine the resonant frequency and location of the strongest modal fields. For the preliminary simulation, make sure the broadband source is enabled, and the dipole source is disabled. The time monitor is set up to start recording fields after 20 fs when the transient fields have decayed so that only resonant fields of the structure remain. By plotting the spectrum result from the time monitor, the resonant frequency of the mode can be identified.

Using this information, the profile monitor is set up to use apodization again to exclude the effect of the source and record data at the resonant frequency. The dipole source frequency is then set to the resonant frequency and the dipole is placed in the location where the modal fields are maximized. With the dipole source enabled, and the broadband source disabled, re-run the simulation and the dipole source result window provides the Purcell factor estimation.

APPENDIX D

FABRICATION OF PSI-ABRS

ABRs were patterned onto the porous silicon samples using CMOS compatible fabrication processes. Porous silicon core and cladding layers, 200 nm and 700 nm thick, were prepared by the electrochemical etch of p-type silicon wafers at current densities of 20 mA/cm^2 and 70 mA/cm^2. The estimated porosities and refractive indices are 60 %, 79 % and n_{core} = 1.75, $n_{cladding}$ = 1.3 for the core and cladding layers respectively. An 800°C, 15 min thermal oxidation of the samples was carried out in order to ensure a chemically stable, oxidized PSi surface with an estimated oxide thickness of ~2 nm, as detailed in earlier in **Chapter 3**. The oxidized silicon surface also allows for more controllable RIE process control over the etch rate for the core waveguiding layer. ZEP 520A resist, was spun at 5000 rpm onto each PSi sample to create a 300 nm resist film. The resist was then exposed using electron-beam lithography (JEOL9300F) to transfer the designed optical resonator pattern at 100 kV voltage, 400 C/cm^2 onto the sample surface. The width and period of the annular Bragg resonators were varied by ± 20 nm in steps of 5 nm each to account for fabrication variances in the exposure dose and resist development steps. The exposed sample patterns were then developed in xylenes for 30 seconds followed by a thorough IPA rinse. An Oxford Plasmalab 100 RIE tool was used with a C4F8/SF6/Ar gas flow to transfer the GDS layout pattern onto the core PSi ridge waveguiding layer. A top view and cross-sectional SEM image of the fabricated PSi annular Bragg resonator is

shown in **Figure D1**. Difference in pore sizes and porosities between the core and cladding layers are clearly evident from the SEM images.

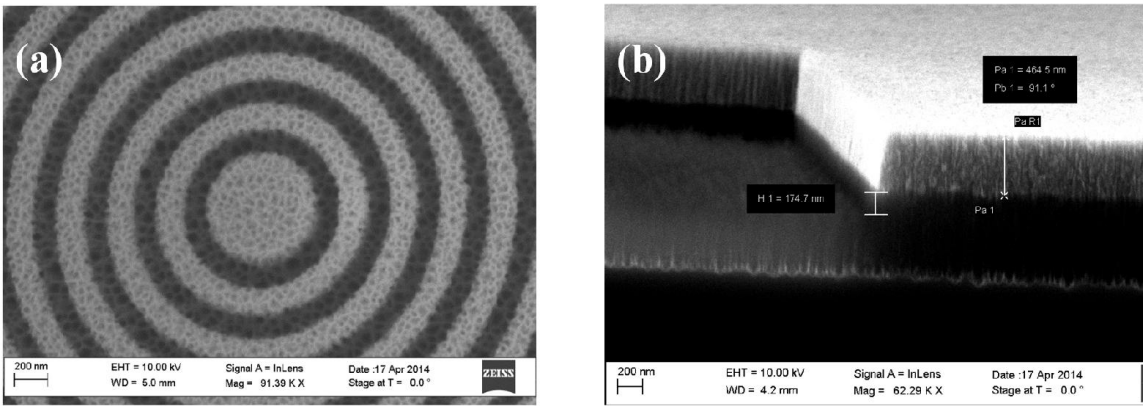

Figure D1. Top view and cross-sectional SEM images of fabricated PSi annular Bragg resonators.

APPENDIX E

QDS IN PSI MICROCAVITIES

QDs immobilized in defect region result in cavity modified enhanced photoluminescence. Spontaneous emission rate increases by ~10-fold.

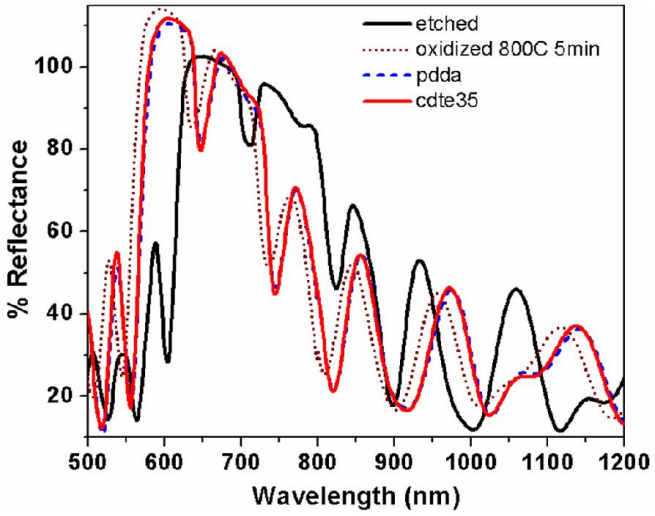

Cavity mode at 650 nm for infiltrated CdTe QDs.

λ_{peak} of QDs in solution = 640 nm

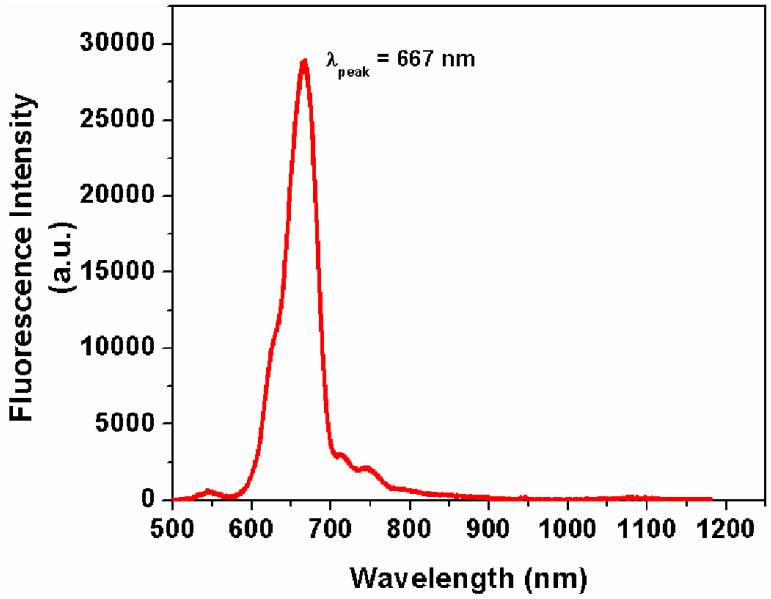

Transfer matrix simulated cavity mode at 701 nm.

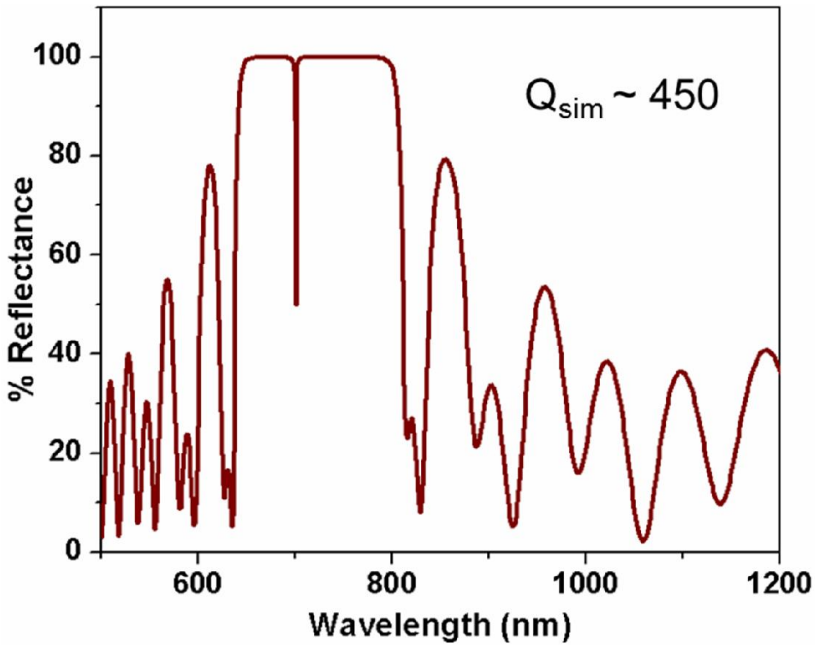

Freshly etched cavity mode at 697 nm.

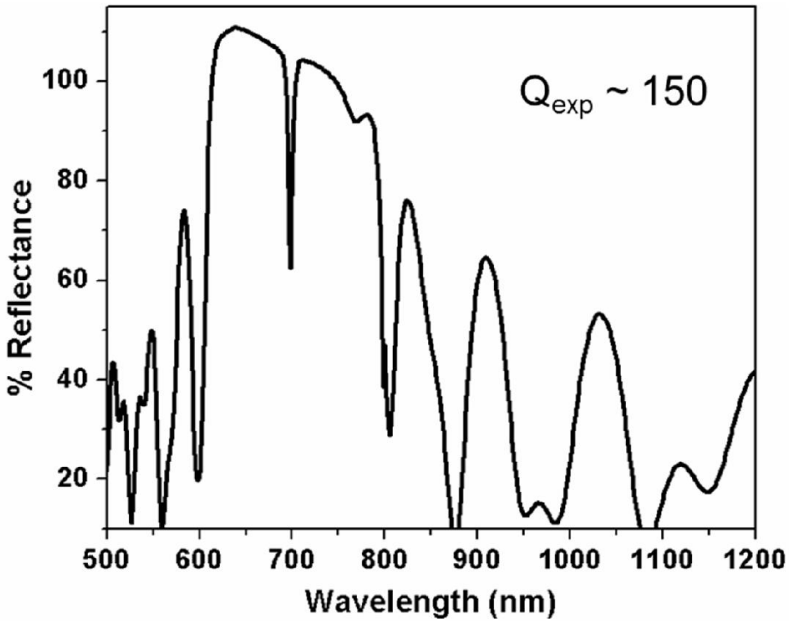

REFERENCES

1. Gates, B., The next outbreak? We're not ready In *TED Talk*, 2015.
2. Fan, X. D.; White, I. M.; Shopova, S. I.; Zhu, H. Y.; Suter, J. D.; Sun, Y. Z., Sensitive optical biosensors for unlabeled targets: A review. *Anal Chim Acta* **2008,** *620* (1-2), 8-26.
3. Hoa, X. D.; Kirk, A. G.; Tabrizian, M., Towards integrated and sensitive surface plasmon resonance biosensors: A review of recent progress. *Biosensors and Bioelectronics* **2007,** *23* (2), 151-160.
4. Fan, X.; White, I. M.; Shopova, S. I.; Zhu, H.; Suter, J. D.; Sun, Y., Sensitive optical biosensors for unlabeled targets: A review. *Analytica Chimica Acta* **2008,** *620* (1–2), 8-26.
5. Liedberg, B.; Nylander, C.; Lunström, I., Surface plasmon resonance for gas detection and biosensing. *Sensors and Actuators* **1983,** *4* (0), 299-304.
6. Engvall, E.; Perlmann, P., Enzyme-linked immunosorbent assay (ELISA) quantitative assay of immunoglobulin G. *Immunochemistry* **1971,** *8* (9), 871-874.
7. Friguet, B.; Chaffotte, A. F.; Djavadi-Ohaniance, L.; Goldberg, M. E., Measurements of the true affinity constant in solution of antigen-antibody complexes by enzyme-linked immunosorbent assay. *Journal of Immunological Methods* **1985,** *77* (2), 305-319.
8. Pacholski, C.; Sartor, M.; J. Sailor, M.; Cunin, F.; Miskelly, G. M., Biosensing using porous silicon double-layer interferometers: reflective interferometric fourier transform spectroscopy. *J. Am. Chem. Soc.* **2005,** *127* (33), 11636–11645.
9. Kerr, R. A., Radiation Will Make Astronauts' Trip to Mars Even Riskier. *Science* **2013,** *340* (6136), 1031-1031.
10. Butson, M. J.; Yu, P. K. N.; Cheung, T.; Metcalfe, P., Radiochromic film for medical radiation dosimetry. *Materials Science and Engineering: R: Reports* **2003,** *41* (3–5), 61-120.
11. Attix, F. H.; Roesch, W. C.; Tochilin, E., *Radiation Dosimetry*. Second ed.; Academic Press: 1968; Vol. I.
12. Nagamatsu, A.; Murakami, K.; Kitajo, K.; Shimada, K.; Kumagai, H.; Tawara, H., Area radiation monitoring on ISS Increments 17 to 22 using PADLES in the Japanese Experiment Module Kibo. *Radiation Measurements* **2013,** *59* (0), 84-93.
13. Benton, E. R.; Benton, E. V., Space radiation dosimetry in low-Earth orbit and beyond. *Nuclear Instruments and Methods in Physics Research Section B: Beam Interactions with Materials and Atoms* **2001,** *184* (1–2), 255-294.
14. Uhlir, A., Electrolytic Shaping of Germanium and Silicon. *Bell System Technical Journal* **1956,** *35* (2), 333-347.
15. Cullis, A. G.; Canham, L. T., Visible light emission due to quantum size effects in highly porous crystalline silicon. *Nature* **1991,** *353* (6342), 335-338.

16. Sailor, M. J., Fundamentals of Porous Silicon Preparation. In *Porous Silicon in Practice*, Wiley-VCH Verlag GmbH & Co. KGaA: 2011; pp 1-42.
17. Janshoff, A.; Dancil, K.-P. S.; Steinem, C.; Greiner, D. P.; Lin, V. S. Y.; Gurtner, C.; Motesharei, K.; Sailor, M. J.; Ghadiri, M. R., Macroporous p-Type Silicon Fabry−Perot Layers. Fabrication, Characterization, and Applications in Biosensing. *Journal of the American Chemical Society* **1998,** *120* (46), 12108-12116.
18. Menna, P.; Di Francia, G.; La Ferrara, V., Porous silicon in solar cells: A review and a description of its application as an AR coating. *Solar Energy Materials and Solar Cells* **1995,** *37* (1), 13-24.
19. Gaur, G.; Koktysh, D. S.; Weiss, S. M., Immobilization of Quantum Dots in Nanostructured Porous Silicon Films: Characterizations and Signal Amplification for Dual-Mode Optical Biosensing. *Advanced Functional Materials* **2013,** *23* (29), 3604-3614.
20. Arrand, H. F. Optical waveguides and components based on porous silicon. PhD thesis, University of Nottingham, 1997.
21. Rong, G.; Najmaie, A.; Sipe, J. E.; Weiss, S. M., Nanoscale porous silicon waveguide for label-free DNA sensing. *Biosensors and Bioelectronics* **2008,** *23* (10), 1572-1576.
22. Wei, X.; Weiss, S. M., Guided mode biosensor based on grating coupled porous silicon waveguide. *Opt. Express* **2011,** *19* (12), 11330-11339.
23. Lawrie, J. L.; Yang, J.; Weiss, S. M., Size-Dependent Infiltration and Optical Detection of Nucleic Acids in Nanoscale Pores. *Nanotechnology, IEEE Transactions on* **2010,** *9* (5), 596-602.
24. El Beheiry, M.; Liu, V.; Fan, S.; Levi, O., Sensitivity enhancement in photonic crystal slab biosensors. *Opt. Express* **2010,** *18* (22), 22702-22714.
25. Tenenbaum, E.; Ben Dov, N.; Segal, E., Tethered lipid bilayers within porous Si nanostructures: A platform for real-time optical monitoring of membrane-associated processes. *Langmuir* **2015**.
26. Beavers, K. R.; Mares, J. W.; Swartz, C. M.; Zhao, Y.; Weiss, S. M.; Duvall, C. L., In Situ Synthesis of Peptide Nucleic Acids in Porous Silicon for Drug Delivery and Biosensing. *Bioconjugate Chemistry* **2014**.
27. Rong, G.; Ryckman, J.; Mernaugh, R.; Weiss, S. M., Label-free porous silicon membrane waveguide for DNA sensing. *Appl. Phys. Lett.* **2008,** *93*, 161109.
28. Jiao, Y.; Weiss, S. M., Design parameters and sensitivity analysis of polymer-cladded porous silicon waveguides for small molecule detection. *Biosensors and Bioelectronics* **2010,** *25* (6), 1535-1538.
29. Krioukov, E.; Greve, J.; Otto, C., Performance of integrated optical microcavities for refractive index and fluorescence sensing. *Sensor Actuat B-Chem* **2003,** *90* (1-3), 58-67.
30. Iqbal, M.; Gleeson, M. A.; Spaugh, B.; Tybor, F.; Gunn, W. G.; Hochberg, M.; Baehr-Jones, T.; Bailey, R. C.; Gunn, L. C., Label-Free Biosensor Arrays Based on Silicon Ring Resonators and High-Speed Optical Scanning Instrumentation. *Ieee J Sel Top Quant* **2010,** *16* (3), 654-661.

31. Chen, Y.; Fegadolli, W. S.; Jones, W. M.; Scherer, A.; Li, M., Ultrasensitive Gas-Phase Chemical Sensing Based on Functionalized Photonic Crystal Nanobeam Cavities. *ACS Nano* **2014,** *8* (1), 522-527.
32. Hu, S.; Zhao, Y.; Qin, K.; Retterer, S. T.; Kravchenko, I. I.; Weiss, S. M., Enhancing the Sensitivity of Label-Free Silicon Photonic Biosensors through Increased Probe Molecule Density. *ACS Photonics* **2014,** *1* (7), 590-597.
33. Kirk, J. T.; Fridley, G. E.; Chamberlain, J. W.; Christensen, E. D.; Hochberg, M.; Ratner, D. M., Multiplexed inkjet functionalization of silicon photonic biosensors. *Lab Chip* **2011,** *11* (7), 1372-1377.
34. Carlborg, C. F.; Gylfason, K. B.; Kazmierczak, A.; Dortu, F.; Banuls Polo, M. J.; Maquieira Catala, A.; Kresbach, G. M.; Sohlstrom, H.; Moh, T.; Vivien, L.; Popplewell, J.; Ronan, G.; Barrios, C. A.; Stemme, G.; van der Wijngaart, W., A packaged optical slot-waveguide ring resonator sensor array for multiplex label-free assays in labs-on-chips. *Lab Chip* **2010,** *10* (3), 281-290.
35. Kang, C.; Phare, C. T.; Vlasov, Y. A.; Assefa, S.; Weiss, S. M., Photonic crystal slab sensor with enhanced surface area. *Opt. Express* **2010,** *18* (26), 27930-27937.
36. Chakravarty, S.; Lai, W. C.; Zou, Y.; Drabkin, H. A.; Gemmill, R. M.; Simon, G. R.; Chin, S. H.; Chen, R. T., Multiplexed specific label-free detection of NCI-H358 lung cancer cell line lysates with silicon based photonic crystal microcavity biosensors. *Biosensors & bioelectronics* **2013,** *43*, 50-55.
37. Shi, L.; Pottier, P.; Peter, Y.-A.; Skorobogatiy, M., Guided-mode resonance photonic crystalslab sensors based on bead monolayergeometry. *Opt. Express* **2008,** *16* (22), 17962-17971.
38. Biao, Q.; Ping, Y.; Yubo, L.; Xiaoqing, J.; Mei, Y.; Jianyi, Y., Analysis of Electrooptic Modulator With 1-D Slotted Photonic Crystal Nanobeam Cavity. *Photonics Technology Letters, IEEE* **2011,** *23* (14), 992-994.
39. Moll, N.; Stöferle, T.; Schönenberger, S.; Mahrt, R. F., Ultra-high quality-factor resonators with perfect azimuthal modal-symmetry. *Opt. Express* **2009,** *17* (23), 20998-21006.
40. Mateus, C. F.; Huang, M. C.; Chen, L.; Chang-Hasnain, C. J.; Suzuki, Y., Broad-band mirror (1.12-1.62 μm) using a subwavelength grating. *Photonics Technology Letters, IEEE* **2004,** *16* (7), 1676-1678.
41. Klemm, A. B.; Stellinga, D.; Martins, E. R.; Lewis, L.; Huyet, G.; O'Faolain, L.; Krauss, T. F., Experimental high numerical aperture focusing with high contrast gratings. *Opt Lett* **2013,** *38* (17), 3410-3413.
42. Huang, M. C.; Zhou, Y.; Chang-Hasnain, C. J., A surface-emitting laser incorporating a high-index-contrast subwavelength grating. *Nat Photonics* **2007,** *1* (2), 119-122.
43. Kanamori, Y.; Ishimori, M.; Hane, K., High efficient light-emitting diodes with antireflection subwavelength gratings. *Photonics Technology Letters, IEEE* **2002,** *14* (8), 1064-1066.
44. Karagodsky, V.; Sedgwick, F. G.; Chang-Hasnain, C. J., Theoretical analysis of subwavelength high contrast grating reflectors. *Opt. Express* **2010,** *18* (16), 16973-16988.

45. Zhu, L.; Kapraun, J.; Ferrara, J.; Chang-Hasnain, C. J., Flexible photonic metastructures for tunable coloration. *Optica* **2015,** *2* (3), 255-258.
46. Klimov, V. I., *Semiconductor and metal nanocrystals: synthesis and electronic and optical properties*. CRC Press: 2003.
47. Etgar, L.; Zhang, W.; Gabriel, S.; Hickey, S. G.; Nazeeruddin, M. K.; Eychmüller, A.; Liu, B.; Grätzel, M., High Efficiency Quantum Dot Heterojunction Solar Cell Using Anatase (001) TiO2 Nanosheets. *Advanced Materials* **2012,** *24* (16), 2202-2206.
48. Lu, S.; Lingley, Z.; Asano, T.; Harris, D.; Barwicz, T.; Guha, S.; Madhukar, A., Photocurrent Induced by Nonradiative Energy Transfer from Nanocrystal Quantum Dots to Adjacent Silicon Nanowire Conducting Channels: Toward a New Solar Cell Paradigm. *Nano Lett* **2009,** *9* (12), 4548-4552.
49. Akahane, Y.; Asano, T.; Song, B. S.; Noda, S., High-Q photonic nanocavity in a two-dimensional photonic crystal. *Nature* **2003,** *425* (6961), 944-947.
50. Rizvi, S. B.; Ghaderi, S.; Keshtgar, M.; Seifalian, A. M., Semiconductor quantum dots as fluorescent probes for in vitro and in vivo bio-molecular and cellular imaging. *Nano Reviews* **2010,** *1*, 10.3402/nano.v3401i3400.5161.
51. Sukhovatkin, V.; Hinds, S.; Brzozowski, L.; Sargent, E. H., Colloidal Quantum-Dot Photodetectors Exploiting Multiexciton Generation. *Science* **2009,** *324* (5934), 1542-1544.
52. McDonald, S. A.; Konstantatos, G.; Zhang, S.; Cyr, P. W.; Klem, E. J. D.; Levina, L.; Sargent, E. H., Solution-processed PbS quantum dot infrared photodetectors and photovoltaics. *Nat Mater* **2005,** *4* (2), 138-142.
53. Harrison, M. Heterogeneously Alloyed Semiconductor Nanocrystals with Induced Chemical Composition Gradients. Vanderbilt University, 2012.
54. Jiao, Y. A study of improved optical sensing performances based on nanoscale porous substrates. Vanderbilt University, 2013.
55. Yeh, P., *Optical waves in layered media*. Wiley New York: 1988; Vol. 95.
56. Yee, K. S., Numerical solution of initial boundary value problems involving Maxwell's equations in isotropic media. *IEEE Trans. Antennas Propag* **1966,** *14* (3), 302-307.
57. https://www.lumerical.com/tcad-products/fdtd/features/.
58. Maragos, P.; Schafer, R. W., Morphological systems for multidimensional signal processing. *Proceedings of the IEEE* **1990,** *78* (4), 690-710.
59. Dubertret, B.; Skourides, P.; Norris, D. J.; Noireaux, V.; Brivanlou, A. H.; Libchaber, A., In Vivo Imaging of Quantum Dots Encapsulated in Phospholipid Micelles. *Science* **2002,** *298* (5599), 1759-1762.
60. Howarth, M.; Takao, K.; Hayashi, Y.; Ting, A. Y., Targeting quantum dots to surface proteins in living cells with biotin ligase. *P Natl Acad Sci USA* **2005,** *102* (21), 7583-7588.
61. Rousserie, G.; Sukhanova, A.; Even-Desrumeaux, K.; Fleury, F.; Chames, P.; Baty, D.; Oleinikov, V.; Pluot, M.; Cohen, J. H. M.; Nabiev, I., Semiconductor quantum dots for multiplexed bio-detection on solid-state microarrays. *Critical Reviews in Oncology/Hematology* **2010,** *74* (1), 1-15.

62. Suzuki, M.; Husimi, Y.; Komatsu, H.; Suzuki, K.; Douglas, K. T., Quantum Dot FRET Biosensors that Respond to pH, to Proteolytic or Nucleolytic Cleavage, to DNA Synthesis, or to a Multiplexing Combination. *Journal of the American Chemical Society* **2008,** *130* (17), 5720-5725.
63. Medintz, I. L.; Mattoussi, H.; Clapp, A. R., Potential clinical applications of quantum dots. *International Journal of Nanomedicine* **2008,** *3* (2), 151–167.
64. Sapsford, K.; Pons, T.; Medintz, I.; Mattoussi, H., Biosensing with Luminescent Semiconductor Quantum Dots. *Sensors* **2006,** *6* (8), 925-953.
65. Michalet, X.; Pinaud, F. F.; Bentolila, L. A.; Tsay, J. M.; Doose, S.; Li, J. J.; Sundaresan, G.; Wu, A. M.; Gambhir, S. S.; Weiss, S., Quantum Dots for Live Cells, in Vivo Imaging, and Diagnostics. *Science* **2005,** *307* (5709), 538-544.
66. Chen, Y.; Ren, H. l.; Liu, N.; Sai, N.; Liu, X.; Liu, Z.; Gao, Z.; Ning, B. a., A Fluoroimmunoassay Based on Quantum Dot−Streptavidin Conjugate for the Detection of Chlorpyrifos. *Journal of Agricultural and Food Chemistry* **2010,** *58* (16), 8895-8903.
67. Shiddiky, M. J. A.; Rauf, S.; Kithva, P. H.; Trau, M., Graphene/quantum dot bionanoconjugates as signal amplifiers in stripping voltammetric detection of EpCAM biomarkers. *Biosensors and Bioelectronics* **2012,** *35* (1), 251-257.
68. Kim, Y. G.; Moon, S.; Kuritzkes, D. R.; Demirci, U., Quantum dot-based HIV capture and imaging in a microfluidic channel. *Biosens Bioelectron* **2009,** *25* (1), 253-258.
69. Kerman, K.; Endo, T.; Tsukamoto, M.; Chikae, M.; Takamura, Y.; Tamiya, E., Quantum dot-based immunosensor for the detection of prostate-specific antigen using fluorescence microscopy. *Talanta* **2007,** *71* (4), 1494-1499.
70. Hansen, J. A.; Wang, J.; Kawde, A.-N.; Xiang, Y.; Gothelf, K. V.; Collins, G., Quantum-Dot/Aptamer-Based Ultrasensitive Multi-Analyte Electrochemical Biosensor. *Journal of the American Chemical Society* **2006,** *128* (7), 2228-2229.
71. Medintz, I. L.; Clapp, A. R.; Melinger, J. S.; Deschamps, J. R.; Mattoussi, H., A Reagentless Biosensing Assembly Based on Quantum Dot–Donor Förster Resonance Energy Transfer. *Advanced Materials* **2005,** *17* (20), 2450-2455.
72. Chan, W. C. W.; Nie, S., Quantum Dot Bioconjugates for Ultrasensitive Nonisotopic Detection. *Science* **1998,** *281* (5385), 2016-2018.
73. Sun, B.; Xie, W.; Yi, G.; Chen, D.; Zhou, Y.; Cheng, J., Microminiaturized immunoassays using quantum dots as fluorescent label by laser confocal scanning fluorescence detection. *Journal of Immunological Methods* **2001,** *249* (1–2), 85-89.
74. Goldman, E.; Medintz, I.; Mattoussi, H., Luminescent quantum dots in immunoassays. *Analytical and Bioanalytical Chemistry* **2006,** *384* (3), 560-563.
75. Medintz, I. L.; Uyeda, H. T.; Goldman, E. R.; Mattoussi, H., Quantum dot bioconjugates for imaging, labelling and sensing. *Nat Mater* **2005,** *4* (6), 435-446.
76. Schuler, B.; Eaton, W. A., Protein folding studied by single-molecule FRET. *Current Opinion in Structural Biology* **2008,** *18* (1), 16-26.
77. Merchant, K. A.; Best, R. B.; Louis, J. M.; Gopich, I. V.; Eaton, W. A., Characterizing the unfolded states of proteins using single-molecule FRET spectroscopy and molecular simulations. *Proceedings of the National Academy of Sciences* **2007,** *104* (5), 1528-1533.

78. Dancil, K.-P. S.; Greiner, D. P.; Sailor, M. J., A Porous Silicon Optical Biosensor: Detection of Reversible Binding of IgG to a Protein A-Modified Surface. *Journal of the American Chemical Society* **1999,** *121* (34), 7925-7930.
79. Collins, B. E.; Dancil, K. P. S.; Abbi, G.; Sailor, M. J., Determining Protein Size Using an Electrochemically Machined Pore Gradient in Silicon. *Advanced Functional Materials* **2002,** *12* (3), 187-191.
80. Stewart, M. P.; Buriak, J. M., Chemical and Biological Applications of Porous Silicon Technology. *Advanced Materials* **2000,** *12* (12), 859-869.
81. Jiao, Y.; Koktysh, D. S.; Phambu, N.; Weiss, S. M., Dual-mode sensing platform based on colloidal gold functionalized porous silicon. *Appl Phys Lett* **2010,** *97* (15), 153125-153123.
82. Gold, S.; Chu, K.-L.; Lu, C.; Shannon, M. A.; Masel, R. I., Acid loaded porous silicon as a proton exchange membrane for micro-fuel cells. *Journal of Power Sources* **2004,** *135* (1-2), 198-203.
83. Pichonat, T.; Gauthier-Manuel, B.; Hauden, D., New proton-conducting porous silicon membrane for small fuel cells. *Fuel Cells Bulletin* **2004,** *2004* (8), 11-14.
84. Aravamudhan, S.; Rahman, A. R. A.; Bhansali, S., Porous silicon based orientation independent, self-priming micro direct ethanol fuel cell. *Sensors and Actuators A: Physical* **2005,** *123-124* (0), 497-504.
85. Vitanov, P.; Goranova, E.; Stavrov, V.; Ivanov, P.; Singh, P. K., Fabrication of buried contact silicon solar cells using porous silicon. *Solar Energy Materials and Solar Cells* **2009,** *93* (3), 297-300.
86. Yae, S.; Kawamoto, Y.; Tanaka, H.; Fukumuro, N.; Matsuda, H., Formation of porous silicon by metal particle enhanced chemical etching in HF solution and its application for efficient solar cells. *Electrochemistry Communications* **2003,** *5* (8), 632-636.
87. Gultepe, E.; Nagesha, D.; Sridhar, S.; Amiji, M., Nanoporous inorganic membranes or coatings for sustained drug delivery in implantable devices. *Advanced Drug Delivery Reviews* **2010,** *62* (3), 305-315.
88. Salonen, J.; Laitinen, L.; Kaukonen, A. M.; Tuura, J.; Björkqvist, M.; Heikkilä, T.; Vähä-Heikkilä, K.; Hirvonen, J.; Lehto, V. P., Mesoporous silicon microparticles for oral drug delivery: Loading and release of five model drugs. *Journal of Controlled Release* **2005,** *108* (2-3), 362-374.
89. Anglin, E. J.; Cheng, L.; Freeman, W. R.; Sailor, M. J., Porous silicon in drug delivery devices and materials. *Advanced Drug Delivery Reviews* **2008,** *60* (11), 1266-1277.
90. Salonen, J.; Kaukonen, A. M.; Hirvonen, J.; Lehto, V.-P., Mesoporous silicon in drug delivery applications. *Journal of Pharmaceutical Sciences* **2008,** *97* (2), 632-653.
91. Wu, E. C.; Park, J.-H.; Park, J.; Segal, E.; Cunin, F. d. r.; Sailor, M. J., Oxidation-Triggered Release of Fluorescent Molecules or Drugs from Mesoporous Si Microparticles. *ACS Nano* **2008,** *2* (11), 2401-2409.

92. Park, J.-H.; Gu, L.; von Maltzahn, G.; Ruoslahti, E.; Bhatia, S. N.; Sailor, M. J., Biodegradable luminescent porous silicon nanoparticles for in vivo applications. *Nat Mater* **2009,** *8* (4), 331-336.
93. Tasciotti, E.; Liu, X.; Bhavane, R.; Plant, K.; Leonard, A. D.; Price, B. K.; Cheng, M. M.-C.; Decuzzi, P.; Tour, J. M.; Robertson, F.; Ferrari, M., Mesoporous silicon particles as a multistage delivery system for imaging and therapeutic applications. *Nat Nano* **2008,** *3* (3), 151-157.
94. Li, Z. F.; Ruckenstein, E., Water-Soluble Poly(acrylic acid) Grafted Luminescent Silicon Nanoparticles and Their Use as Fluorescent Biological Staining Labels. *Nano Lett* **2004,** *4* (8), 1463-1467.
95. Qian, J.; Zhang, C.; Cao, X.; Liu, S., Versatile Immunosensor Using a Quantum Dot Coated Silica Nanosphere as a Label for Signal Amplification. *Analytical Chemistry* **2010,** *82* (15), 6422-6429.
96. Hines, M. A.; Scholes, G. D., Colloidal PbS nanocrystals with size-tunable near-infrared emission: Observation of post-synthesis self-narrowing of the particle size distribution. *Adv. Mater.* **2003,** *15*, 1844-1849.
97. Koktysh, D. S.; McBride, J. R.; Dixit, S. K.; Feldman, L. C.; Rosenthal, S. J., PbS/PbSe structures with core–shell type morphology synthesized from PbS nanocrystals. *Nanotechnology* **2007,** *18* (49), 495607.
98. Torimoto, T.; Adachi, T.; Okazaki, K.; Sakuraoka, M.; Shibayama, T.; Ohtani, B.; Kudo, A.; Kuwabata, S., Facile synthesis of ZnS-AgInS2 solid solution nanoparticles for a color-adjustable luminophore. *Journal of the American Chemical Society* **2007,** *129* (41), 12388-12389.
99. Torimoto, T.; Ogawa, S.; Adachi, T.; Kameyama, T.; Okazaki, K. I.; Shibayama, T.; Kudo, A.; Kuwabata, S., Remarkable photoluminescence enhancement of ZnS-AgInS2 solid solution nanoparticles by post-synthesis treatment. *Chem Commun* **2010,** *46* (12), 2082-2084.
100. Pong, B. K.; Trout, B. L.; Lee, J. Y., Modified ligand-exchange for efficient solubilization of CdSe/ZnS quantum dots in water: A procedure guided by computational studies. *Langmuir* **2008,** *24* (10), 5270-5276.
101. Zhong, X. H.; Zhang, W. J.; Chen, G. J.; Wang, J.; Ye, B. C., Design and Synthesis of Highly Luminescent Near-Infrared-Emitting Water-Soluble CdTe/CdSe/ZnS Core/Shell/Shell Quantum Dots. *Inorg Chem* **2009,** *48* (20), 9723-9731.
102. Koktysh, D.; Bright, V.; Pham, W., Fluorescent magnetic hybrid nanoprobe for multimodal bioimaging. *Nanotechnology* **2011,** *22* (27), 275606.
103. Zheng, Y. G.; Gao, S. J.; Ying, J. Y., Synthesis and cell-imaging applications of glutathione-capped CdTe quantum dots. *Adv Mater* **2007,** *19* (3), 376-378.
104. Rong, G.; Saarinen, J. J.; Sipe, J. E.; Weiss, S. M. In *High sensitivity sensor based on porous silicon waveguide*, MRS Proceedings, Cambridge Univ Press: 2006; pp 0934-I0910-0904.
105. Ouyang, H.; Striemer, C. C.; Fauchet, P. M., Quantitative analysis of the sensitivity of porous silicon optical biosensors. *Applied Physics Letters* **2006,** *88* (16), 163108-163103.

106. Gaur, G.; Koktysh, D.; Weiss, S. M., Integrating Colloidal Quantum Dots with Porous Silicon for High Sensitivity Biosensing. Materials Research Society Symposium Proceeding: 2011; Vol. 1301, pp 241-246.
107. Lu, H.; Yi, G.; Zhao, S.; Chen, D.; Guo, L.-H.; Cheng, J., Synthesis and characterization of multi-functional nanoparticles possessing magnetic, up-conversion fluorescence and bio-affinity properties. *Journal of Materials Chemistry* **2004,** *14* (8), 1336-1341.
108. Kim, S. T.; Kim, D.-J.; Kim, T.-J.; Seo, D.-W.; Kim, T.-H.; Lee, S.-Y.; Kim, K.; Lee, K.-M.; Lee, S.-K., Novel Streptavidin-Functionalized Silicon Nanowire Arrays for CD4+ T Lymphocyte Separation. *Nano Lett* **2010,** *10* (8), 2877-2883.
109. Singh, S.; Lapin, N.; Singh, P.; Khan, M. A.; Chabal, Y. J. In *Attachment Of Streptavidin-Biotin On 3-Aminopropyltriethoxysilane (APTES) Modified Porous Silicon Surfaces*, TRANSPORT AND OPTICAL PROPERTIES OF NANOMATERIALS: Proceedings of the International Conference—ICTOPON-2009, AIP Publishing: 2009; pp 443-449.
110. Dyadyusha, L.; Yin, H.; Jaiswal, S.; Brown, T.; Baumberg, J. J.; Booy, F. P.; Melvin, T., *Chem Commun (Camb)*. **2005,** *25* (null), 3201.
111. Pavesi, L.; Panzarini, G.; Andreani, L. C., All-porous silicon-coupled microcavities: Experiment versus theory. *Phys Rev B* **1998,** *58* (23), 15794-15800.
112. Reddy, R. R.; Nazeer Ahammed, Y.; Rama Gopal, K.; Abdul Azeem, P.; Sasikala Devi, B.; Rao, T. V. R.; Behere, S. H., On the equivalence between Clausius–Mossotti and optical electronegativity relations. *Optical Materials* **2003,** *22* (1), 7-11.
113. Buriak, J. M.; Stewart, M. P.; Geders, T. W.; Allen, M. J.; Choi, H. C.; Smith, J.; Raftery, D.; Canham, L. T., Lewis acid mediated hydrosilylation on porous silicon surfaces. *Journal of the American Chemical Society* **1999,** *121* (49), 11491-11502.
114. Lee, M. R.; Miller, B. L.; Fauchet, P. M. In *Two-Dimensional Photonic Crystal Slot Microcavity Sensor for Virus-Sized Particle Detection*, Integrated Photonics and Nanophotonics Research and Applications, Boston, Massachusetts, 2008/07/13; Optical Society of America: Boston, Massachusetts, 2008; p ITuC4.
115. Takahashi, D.; Hachuda, S.; Watanabe, T.; Nishijima, Y.; Baba, T., Detection of endotoxin using a photonic crystal nanolaser. *Applied Physics Letters* **2015,** *106* (13), 131112.
116. Heydari, E.; Buller, J.; Wischerhoff, E.; Laschewsky, A.; Döring, S.; Stumpe, J., Label-Free Biosensor Based on an All-Polymer DFB Laser. *Advanced Optical Materials* **2014,** *2* (2), 137-141.
117. Watanabe, K.; Kishi, Y.; Hachuda, S.; Watanabe, T.; Sakemoto, M.; Nishijima, Y.; Baba, T., Simultaneous detection of refractive index and surface charges in nanolaser biosensors. *Applied Physics Letters* **2015,** *106* (2), 021106.
118. Purcell, E. M.; Torrey, H. C.; Pound, R. V., Resonance Absorption by Nuclear Magnetic Moments in a Solid. *Physical Review* **1946,** *69* (1-2), 37-38.
119. Coccioli, R.; Boroditsky, M.; Kim, K.; Rahmat-Samii, Y.; Yablonovitch, E., Smallest possible electromagnetic mode volume in a dielectric cavity. *IEE Proceedings-Optoelectronics* **1998,** *145* (6), 391-397.

120. Burstein, E.; Weisbuch, C., *Confined electrons and photons: new physics and applications*. Springer Science & Business Media: 2012; Vol. 340.
121. Gayral, B.; Gerard, J.; Lemaıtre, A.; Dupuis, C.; Manin, L.; Pelouard, J., High-Q wet-etched GaAs microdisks containing InAs quantum boxes. *Applied physics letters* **1999,** *75* (13), 1908-1910.
122. Kolchin, P.; Pholchai, N.; Mikkelsen, M. H.; Oh, J.; Ota, S.; Islam, M. S.; Yin, X.; Zhang, X., High Purcell factor due to coupling of a single emitter to a dielectric slot waveguide. *Nano Lett* **2014,** *15* (1), 464-468.
123. Scheuer, J.; Green, W. M. J.; DeRose, G. A.; Yariv, A., Lasing from a circular Bragg nanocavity with an ultrasmall modal volume. *Applied Physics Letters* **2005,** *86* (25), -.
124. Song, W.; Vasdekis, A. E.; Li, Z.; Psaltis, D., Optofluidic evanescent dye laser based on a distributed feedback circular grating. *Applied Physics Letters* **2009,** *94* (16), 161110.
125. Turnbull, G.; Carleton, A.; Barlow, G.; Tahraouhi, A.; Krauss, T.; Shore, K.; Samuel, I., Influence of grating characteristics on the operation of circular-grating distributed-feedback polymer lasers. *Journal of applied physics* **2005,** *98* (2), 023105.
126. Liu, Y.; Wang, S.; Park, Y.-S.; Yin, X.; Zhang, X., Fluorescence enhancement by a two-dimensional dielectric annular Bragg resonant cavity. *Opt. Express* **2010,** *18* (24), 25029-25034.
127. Scullion, M. G.; Di Falco, A.; Krauss, T. F., Slotted photonic crystal cavities with integrated microfluidics for biosensing applications. *Biosensors & bioelectronics* **2011,** *27* (1), 101-105.
128. Almeida, V. R.; Xu, Q. F.; Barrios, C. A.; Lipson, M., Guiding and confining light in void nanostructure. *Opt Lett* **2004,** *29* (11), 1209-1211.
129. Englund, D.; Fattal, D.; Waks, E.; Solomon, G.; Zhang, B.; Nakaoka, T.; Arakawa, Y.; Yamamoto, Y.; Vučković, J., Controlling the Spontaneous Emission Rate of Single Quantum Dots in a Two-Dimensional Photonic Crystal. *Physical Review Letters* **2005,** *95* (1), 013904.
130. Kuttge, M.; García de Abajo, F. J.; Polman, A., Ultrasmall Mode Volume Plasmonic Nanodisk Resonators. *Nano Lett* **2010,** *10* (5), 1537-1541.
131. Zhao, J.; Bardecker, J. A.; Munro, A. M.; Liu, M. S.; Niu, Y.; Ding, I. K.; Luo, J.; Chen, B.; Jen, A. K. Y.; Ginger, D. S., Efficient CdSe/CdS Quantum Dot Light-Emitting Diodes Using a Thermally Polymerized Hole Transport Layer. *Nano Lett* **2006,** *6* (3), 463-467.
132. Sun, Q.; Wang, Y. A.; Li, L. S.; Wang, D.; Zhu, T.; Xu, J.; Yang, C.; Li, Y., Bright, multicoloured light-emitting diodes based on quantum dots. *Nat Photon* **2007,** *1* (12), 717-722.
133. Caruge, J. M.; Halpert, J. E.; Wood, V.; Bulovic, V.; Bawendi, M. G., Colloidal quantum-dot light-emitting diodes with metal-oxide charge transport layers. *Nat Photon* **2008,** *2* (4), 247-250.

134. Cho, K.-S.; Lee, E. K.; Joo, W.-J.; Jang, E.; Kim, T.-H.; Lee, S. J.; Kwon, S.-J.; Han, J. Y.; Kim, B.-K.; Choi, B. L.; Kim, J. M., High-performance crosslinked colloidal quantum-dot light-emitting diodes. *Nat Photon* **2009,** *3* (6), 341-345.
135. Shirasaki, Y.; Supran, G. J.; Bawendi, M. G.; Bulovic, V., Emergence of colloidal quantum-dot light-emitting technologies. *Nat Photon* **2013,** *7* (1), 13-23.
136. Heiss, M.; Fontana, Y.; Gustafsson, A.; Wüst, G.; Magen, C.; O'Regan, D. D.; Luo, J. W.; Ketterer, B.; Conesa-Boj, S.; Kuhlmann, A. V.; Houel, J.; Russo-Averchi, E.; Morante, J. R.; Cantoni, M.; Marzari, N.; Arbiol, J.; Zunger, A.; Warburton, R. J.; Fontcuberta i Morral, A., Self-assembled quantum dots in a nanowire system for quantum photonics. *Nat Mater* **2013,** *12* (5), 439-444.
137. Pacifici, D.; Lezec, H. J.; Atwater, H. A., All-optical modulation by plasmonic excitation of CdSe quantum dots. *Nature photonics* **2007,** *1* (7), 402-406.
138. Ning, Z.; Voznyy, O.; Pan, J.; Hoogland, S.; Adinolfi, V.; Xu, J.; Li, M.; Kirmani, A. R.; Sun, J.-P.; Minor, J.; Kemp, K. W.; Dong, H.; Rollny, L.; Labelle, A.; Carey, G.; Sutherland, B.; Hill, I.; Amassian, A.; Liu, H.; Tang, J.; Bakr, O. M.; Sargent, E. H., Air-stable n-type colloidal quantum dot solids. *Nat Mater* **2014,** *13* (8), 822-828.
139. Labelle, A. J.; Thon, S. M.; Masala, S.; Adachi, M. M.; Dong, H.; Farahani, M.; Ip, A. H.; Fratalocchi, A.; Sargent, E. H., Colloidal Quantum Dot Solar Cells Exploiting Hierarchical Structuring. *Nano Letters* **2015,** *15* (2), 1101-1108.
140. Lee, Y.-L.; Lo, Y.-S., Highly Efficient Quantum-Dot-Sensitized Solar Cell Based on Co-Sensitization of CdS/CdSe. *Advanced Functional Materials* **2009,** *19* (4), 604-609.
141. Schaller, R. D.; Sykora, M.; Pietryga, J. M.; Klimov, V. I., Seven Excitons at a Cost of One: Redefining the Limits for Conversion Efficiency of Photons into Charge Carriers. *Nano Lett* **2006,** *6* (3), 424-429.
142. Gao, J.; Luther, J. M.; Semonin, O. E.; Ellingson, R. J.; Nozik, A. J.; Beard, M. C., Quantum Dot Size Dependent J−V Characteristics in Heterojunction ZnO/PbS Quantum Dot Solar Cells. *Nano Lett* **2011,** *11* (3), 1002-1008.
143. Gao, J.; Perkins, C. L.; Luther, J. M.; Hanna, M. C.; Chen, H.-Y.; Semonin, O. E.; Nozik, A. J.; Ellingson, R. J.; Beard, M. C., n-Type Transition Metal Oxide as a Hole Extraction Layer in PbS Quantum Dot Solar Cells. *Nano Lett* **2011,** *11* (8), 3263-3266.
144. Campbell, I. H.; Crone, B. K., Quantum-Dot/Organic Semiconductor Composites for Radiation Detection. *Advanced Materials* **2006,** *18* (1), 77-79.
145. Létant, S. E.; Wang, T. F., Semiconductor Quantum Dot Scintillation under γ-Ray Irradiation. *Nano Lett* **2006,** *6* (12), 2877-2880.
146. JavauxC; MahlerB; DubertretB; ShabaevA; Rodina, A. V.; EfrosAl, L.; Yakovlev, D. R.; LiuF; BayerM; CampsG; BiadalaL; BuilS; QuelinX; Hermier, J. P., Thermal activation of non-radiative Auger recombination in charged colloidal nanocrystals. *Nat Nano* **2013,** *8* (3), 206-212.
147. Uematsu, T.; Maenosono, S.; Yamaguchi, Y., Photoinduced fluorescence enhancement in CdSe⁄ZnS quantum dot monolayers: Influence of substrate. *Applied Physics Letters* **2006,** *89* (3), 031910.
148. Peng, W.; Sampat, S.; Rupich, S. M.; Anand, B.; Nguyen, H. M.; Taylor, D.; Beardon, B. E.; Gartstein, Y. N.; Chabal, Y. J.; Malko, A. V., Hybrid light sensor based on

ultrathin Si nanomembranes sensitized with CdSe/ZnS colloidal nanocrystal quantum dots. *Nanoscale* **2015,** *7* (18), 8524-8530.
149. Liu, L.; Wang, G.; Li, Y.; Li, Y.; Zhang, J., CdSe quantum dot-sensitized Au/TiO2 hybrid mesoporous films and their enhanced photoelectrochemical performance. *Nano Res.* **2011,** *4* (3), 249-258.
150. Nguyen, H. M.; Seitz, O.; Aureau, D.; Sra, A.; Nijem, N.; Gartstein, Y. N.; Chabal, Y. J.; Malko, A. V., Spectroscopic evidence for nonradiative energy transfer between colloidal CdSe/ZnS nanocrystals and functionalized silicon substrates. *Applied Physics Letters* **2011,** *98* (16), 161904.
151. Nimmo, M. T.; Caillard, L. M.; De Benedetti, W.; Nguyen, H. M.; Seitz, O.; Gartstein, Y. N.; Chabal, Y. J.; Malko, A. V., Visible to Near-Infrared Sensitization of Silicon Substrates via Energy Transfer from Proximal Nanocrystals: Further Insights for Hybrid Photovoltaics. *ACS Nano* **2013,** *7* (4), 3236-3245.
152. Dmitry, K.; Vanessa, B.; Wellington, P., Fluorescent magnetic hybrid nanoprobe for multimodal bioimaging. *Nanotechnology* **2011,** *22* (27), 275606.
153. Liu, Y. F.; Yu, J. S., Selective synthesis of CdTe and high luminescence CdTe/CdS quantum dots: The effect of ligands. *J. Colloid Interface Sci.* **2009,** *333* (2), 690-698.
154. Gaur, G.; Koktysh, D. S.; Fleetwood, D. M.; Weller, R. A.; Reed, R. A.; Weiss, S. M., Influence of interfacial oxide on the optical properties of single layer CdTe/CdS quantum dots in porous silicon scaffolds. *Applied Physics Letters* **2015,** *107* (6), 063106.
155. Smith, A. M.; Lane, L. A.; Nie, S., Mapping the spatial distribution of charge carriers in quantum-confined heterostructures. *Nat Commun* **2014,** *5*.
156. Sambur, J. B.; Novet, T.; Parkinson, B. A., Multiple Exciton Collection in a Sensitized Photovoltaic System. *Science* **2010,** *330* (6000), 63-66.
157. Zeng, Q.; Kong, X.; Sun, Y.; Zhang, Y.; Tu, L.; Zhao, J.; Zhang, H., Synthesis and Optical Properties of Type II CdTe/CdS Core/Shell Quantum Dots in Aqueous Solution via Successive Ion Layer Adsorption and Reaction. *The Journal of Physical Chemistry C* **2008,** *112* (23), 8587-8593.
158. Nulman, J.; Krusius, J. P.; Gat, A., Rapid thermal processing of thin gate dielectrics. Oxidation of silicon. *Electron Device Letters, IEEE* **1985,** *6* (5), 205-207.
159. Grant, N. E.; McIntosh, K. R., A Review on Low Temperature Chemically Formed Silicon Dioxide for Solar Cell Applications. In *Proceedings of the 48th Annual Conference of the Australian Solar Energy Society., 2010, Canberra, Australia.* , 2010.
160. Gaur, G.; Koktysh, D.; Fleetwood, D. M.; Reed, R. A.; Weller, R. A.; Weiss, S. M., Effects of x-ray and gamma-ray irradiation on the optical properties of quantum dots immobilized in porous silicon. In *SPIE*, SPIE Proc., Micro- and Nanotechnology Sensors, Systems, and Applications V,: 2013; Vol. 8725.
161. Rogach, A. L.; Kotov, N. A.; Koktysh, D. S.; Susha, A. S.; Caruso, F., II–VI semiconductor nanocrystals in thin films and colloidal crystals. *Colloids and Surfaces A: Physicochemical and Engineering Aspects* **2002,** *202* (2–3), 135-144.
162. Lucovsky, G.; Mantini, M. J.; Srivastava, J. K.; Irene, E. A., Low-temperature growth of silicon dioxide films: A study of chemical bonding by ellipsometry and infrared spectroscopy. *Journal of Vacuum Science & Technology B* **1987,** *5* (2), 530-537.

163. Wei, S.-H.; Zhang, S. B.; Zunger, A., First-principles calculation of band offsets, optical bowings, and defects in CdS, CdSe, CdTe, and their alloys. *Journal of Applied Physics* **2000,** *87* (3), 1304-1311.
164. Yan, Y.; Chen, G.; Van Patten, P. G., Ultrafast Exciton Dynamics in CdTe Nanocrystals and Core/Shell CdTe/CdS Nanocrystals. *The Journal of Physical Chemistry C* **2011,** *115* (46), 22717-22728.
165. Yoffe, A. D., Low-dimensional systems: Quantum size effects and electronic properties of semiconductor microcrystallites (zero-dimensional systems) and some quasi-two-dimensional systems. *Advances in Physics* **2002,** *51* (2), 799-890.
166. Ben-Chorin, M.; Möller, F.; Koch, F., Band alignment and carrier injection at the porous-silicon–crystalline-silicon interface. *Journal of Applied Physics* **1995,** *77* (9), 4482-4488.
167. Roman, H. E.; Lorenzo, P., Monte Carlo simulations of the recombination dynamics in porous silicon. *Journal of Physics: Condensed Matter* **1996,** *8* (28), 5161.
168. Geyer, S.; Porter, V. J.; Halpert, J. E.; Mentzel, T. S.; Kastner, M. A.; Bawendi, M. G., Charge transport in mixed CdSe and CdTe colloidal nanocrystal films. *Physical Review B* **2010,** *82* (15), 155201.
169. Smith, A. M.; Mohs, A. M.; Nie, S., Tuning the optical and electronic properties of colloidal nanocrystals by lattice strain. *Nat Nano* **2009,** *4* (1), 56-63.
170. Crisp, R. W.; Schrauben, J. N.; Beard, M. C.; Luther, J. M.; Johnson, J. C., Coherent Exciton Delocalization in Strongly Coupled Quantum Dot Arrays. *Nano Lett* **2013,** *13* (10), 4862-4869.
171. Sun, L.; Choi, J. J.; Stachnik, D.; Bartnik, A. C.; Hyun, B.-R.; Malliaras, G. G.; Hanrath, T.; Wise, F. W., Bright infrared quantum-dot light-emitting diodes through inter-dot spacing control. *Nat Nano* **2012,** *7* (6), 369-373.
172. Gao, Y.; Sandeep, C. S. S.; Schins, J. M.; Houtepen, A. J.; Siebbeles, L. D. A., Disorder strongly enhances Auger recombination in conductive quantum-dot solids. *Nat Commun* **2013,** *4*.
173. Meyer, B. K.; Hofmann, D. M.; Stadler, W.; Petrova-Koch, V.; Koch, F.; Omling, P.; Emanuelsson, P., Defects in porous silicon investigated by optically detected and by electron paramagnetic resonance techniques. *Applied Physics Letters* **1993,** *63* (15), 2120-2122.
174. Gao, X.; Cui, Y.; Levenson, R. M.; Chung, L. W.; Nie, S., In vivo cancer targeting and imaging with semiconductor quantum dots. *Nature biotechnology* **2004,** *22* (8), 969-976.
175. Yang, J.; Dave, S. R.; Gao, X., Quantum Dot Nanobarcodes: Epitaxial Assembly of Nanoparticle−Polymer Complexes in Homogeneous Solution. *Journal of the American Chemical Society* **2008,** *130* (15), 5286-5292.
176. Stroh, M.; Zimmer, J. P.; Duda, D. G.; Levchenko, T. S.; Cohen, K. S.; Brown, E. B.; Scadden, D. T.; Torchilin, V. P.; Bawendi, M. G.; Fukumura, D., Quantum dots spectrally distinguish multiple species within the tumor milieu in vivo. *Nature medicine* **2005,** *11* (6), 678-682.

177. Kang, Z.; Zhang, Y.; Menkara, H.; Wagner, B. K.; Summers, C. J.; Lawrence, W.; Nagarkar, V., CdTe quantum dots and polymer nanocomposites for x-ray scintillation and imaging. *Applied Physics Letters* **2011,** *98* (18), 181914-181914-181913.
178. Guffarth, F.; Heitz, R.; Geller, M.; Kapteyn, C.; Born, H.; Sellin, R.; Hoffmann, A.; Bimberg, D.; Sobolev, N. A.; Carmo, M. C., Radiation hardness of InGaAs/GaAs quantum dots. *Applied Physics Letters* **2003,** *82* (12), 1941-1943.
179. Leon, R.; Swift, G. M.; Magness, B.; Taylor, W. A.; Tang, Y. S.; Wang, K. L.; Dowd, P.; Zhang, Y. H., Changes in luminescence emission induced by proton irradiation: InGaAs/GaAs quantum wells and quantum dots. *Applied Physics Letters* **2000,** *76* (15), 2074-2076.
180. Withers, N. J.; Sankar, K.; Akins, B. A.; Memon, T. A.; Gu, T.; Gu, J.; Smolyakov, G. A.; Greenberg, M. R.; Boyle, T. J.; Osiński, M., Rapid degradation of CdSe⁄ZnS colloidal quantum dots exposed to gamma irradiation. *Applied Physics Letters* **2008,** *93* (17), 173101.
181. Padilha, L. A.; Bae, W. K.; Klimov, V. I.; Pietryga, J. M.; Schaller, R. D., Response of Semiconductor Nanocrystals to Extremely Energetic Excitation. *Nano Lett* **2013,** *13* (3), 925-932.
182. Orlova, A.; Gromova, Y. A.; Maslov, V.; Andreeva, O.; Baranov, A.; Fedorov, A.; Prudnikau, A.; Artemyev, M.; Berwick, K., Reversible photoluminescence quenching of CdSe/ZnS quantum dots embedded in porous glass by ammonia vapor. *Nanotechnology* **2013,** *24* (33), 335701.
183. Tawara, H.; Masukawa, M.; Nagamatsu, A.; Kitajo, K.; Kumagai, H.; Yasuda, N., Characteristics of Mg2SiO4:Tb (TLD-MSO-S) relevant for space radiation dosimetry. *Radiation Measurements* **2011,** *46* (8), 709-716.
184. Fleetwood, D. M.; Winokur, P. S.; Beegle, R. W.; Dressendorfer, P. V.; Draper, B. L., Accounting for Dose-Enhancement Effects with CMOS Transistors. *Nuclear Science, IEEE Transactions on* **1985,** *32* (6), 4369-4375.
185. Attix, F. H.; Roesch, W. C.; Tochilin, E., *Radiation Dosimetry: Fundamentals*. Academic Press: 1968.
186. Uematsu, T.; Maenosono, S.; Yamaguchi, Y., Photoinduced Fluorescence Enhancement in Mono- and Multilayer Films of CdSe/ZnS Quantum Dots: Dependence on Intensity and Wavelength of Excitation Light. *The Journal of Physical Chemistry B* **2005,** *109* (18), 8613-8618.
187. Wang, Y.; Tang, Z.; Correa-Duarte, M. A.; Pastoriza-Santos, I.; Giersig, M.; Kotov, N. A.; Liz-Marzán, L. M., Mechanism of strong luminescence photoactivation of citrate-stabilized water-soluble nanoparticles with CdSe cores. *The Journal of Physical Chemistry B* **2004,** *108* (40), 15461-15469.
188. Gaur, G.; Koktysh, D.; Fleetwood, D. M.; Reed, R. A.; Weller, R. A.; Weiss, S. M. In *Effects of x-ray and gamma-ray irradiation on the optical properties of quantum dots immobilized in porous silicon*, 2013; pp 87252D-87252D-87258.
189. Zhao, J.; Nair, G.; Fisher, B. R.; Bawendi, M. G., Challenge to the Charging Model of Semiconductor-Nanocrystal Fluorescence Intermittency from Off-State Quantum Yields and Multiexciton Blinking. *Physical Review Letters* **2010,** *104* (15), 157403.

190. Alivisatos, A. P., Perspectives on the Physical Chemistry of Semiconductor Nanocrystals. *The Journal of Physical Chemistry* **1996,** *100* (31), 13226-13239.
191. Derfus, A. M.; Chan, W. C. W.; Bhatia, S. N., Probing the Cytotoxicity of Semiconductor Quantum Dots. *Nano Lett* **2004,** *4* (1), 11-18.
192. Aldana, J.; Wang, Y. A.; Peng, X., Photochemical Instability of CdSe Nanocrystals Coated by Hydrophilic Thiols. *Journal of the American Chemical Society* **2001,** *123* (36), 8844-8850.
193. Zhang, Y.; Li, Y.; Yan, X.-P., Photoactivated CdTe/CdSe Quantum Dots as a Near Infrared Fluorescent Probe for Detecting Biothiols in Biological Fluids. *Anal Chem* **2009,** *81* (12), 5001-5007.
194. Nirmal, M.; Brus, L., Luminescence photophysics in semiconductor nanocrystals. *Accounts of Chemical Research* **1999,** *32* (5), 407-414.
195. Fonthal, G.; Tirado-Mejía, L.; Marín-Hurtado, J. I.; Ariza-Calderón, H.; Mendoza-Alvarez, J. G., Temperature dependence of the band gap energy of crystalline CdTe. *Journal of Physics and Chemistry of Solids* **2000,** *61* (4), 579-583.
196. Marple, D. T. F., Effective Electron Mass in CdTe. *Physical Review* **1963,** *129* (6), 2466-2470.
197. Gaur, G.; Koktysh, D. S.; Weiss, S. M., Immobilization of Quantum Dots in Nanostructured Porous Silicon Films: Characterizations and Signal Amplification for Dual-Mode Optical Biosensing. *Advanced Functional Materials* **2013**.
198. Efros, A. L.; Rosen, M.; Kuno, M.; Nirmal, M.; Norris, D. J.; Bawendi, M., Band-edge exciton in quantum dots of semiconductors with a degenerate valence band: Dark and bright exciton states. *Phys Rev B* **1996,** *54* (7), 4843-4856.
199. Wang, X.; Qu, L.; Zhang, J.; Peng, X.; Xiao, M., Surface-Related Emission in Highly Luminescent CdSe Quantum Dots. *Nano Lett* **2003,** *3* (8), 1103-1106.
200. Beer, A. C.; Willardson, R. K.; Weber, E. R., *Semiconductors for room temperature nuclear detector applications*. Academic Press: 1995; Vol. 43.
201. Efros, A. L.; Rosen, M., Random Telegraph Signal in the Photoluminescence Intensity of a Single Quantum Dot. *Physical Review Letters* **1997,** *78* (6), 1110-1113.
202. Ellingson, R. J.; Blackburn, J. L.; Yu, P.; Rumbles, G.; Micic, O. I.; Nozik, A. J., Excitation energy dependent efficiency of charge carrier relaxation and photoluminescence in colloidal InP quantum dots. *The Journal of Physical Chemistry B* **2002,** *106* (32), 7758-7765.
203. Kuno, M.; Fromm, D. P.; Johnson, S. T.; Gallagher, A.; Nesbitt, D. J., Modeling distributed kinetics in isolated semiconductor quantum dots. *Physical Review B* **2003,** *67* (12), 125304.
204. Kuno, M.; Fromm, D. P.; Hamann, H. F.; Gallagher, A.; Nesbitt, D. J., ``On"/``off" fluorescence intermittency of single semiconductor quantum dots. *The Journal of Chemical Physics* **2001,** *115* (2), 1028-1040.
205. Lutz, G., *Semiconductor radiation detectors: device physics*. Springer: 1999.